



저작자표시-비영리-변경금지 2.0 대한민국

이용자는 아래의 조건을 따르는 경우에 한하여 자유롭게

- 이 저작물을 복제, 배포, 전송, 전시, 공연 및 방송할 수 있습니다.

다음과 같은 조건을 따라야 합니다:



저작자표시. 귀하는 원저작자를 표시하여야 합니다.



비영리. 귀하는 이 저작물을 영리 목적으로 이용할 수 없습니다.



변경금지. 귀하는 이 저작물을 개작, 변형 또는 가공할 수 없습니다.

- 귀하는, 이 저작물의 재이용이나 배포의 경우, 이 저작물에 적용된 이용허락조건을 명확하게 나타내어야 합니다.
- 저작권자로부터 별도의 허가를 받으면 이러한 조건들은 적용되지 않습니다.

저작권법에 따른 이용자의 권리는 위의 내용에 의하여 영향을 받지 않습니다.

이것은 [이용허락규약\(Legal Code\)](#)을 이해하기 쉽게 요약한 것입니다.

[Disclaimer](#)

공학석사 학위논문

**Experimental Study of 2-Span  
Continuous Beams with 2400 MPa  
Unbonded Tendons**

**2400MPa 비부착 강연선이 적용된 2경간  
연속보의 실험적 연구**

2018 년 8 월

서울대학교 대학원

건축학과

김 경 민



공학석사 학위논문

**Experimental Study of 2-Span  
Continuous Beams with 2400 MPa  
Unbonded Tendons**

**2400MPa 비부착 강연선이 적용된 2경간  
연속보의 실험적 연구**

2018 년 8 월

서울대학교 대학원

건축학과

김 경 민



# Experimental Study of 2-Span Continuous Beams with 2400 MPa Unbonded Tendons

지도 교수 강 현 구

이 논문을 공학석사 학위논문으로 제출함  
2018 년 8 월

서울대학교 대학원  
건축학과  
김 경 민

김경민의 공학석사 학위논문을 인준함  
2018 년 8 월

위 원 장 \_\_\_\_\_ (인)

부위원장 \_\_\_\_\_ (인)

위 원 \_\_\_\_\_ (인)



## **Abstract**

# **Experimental Study of 2-Span Continuous Beams with 2400 MPa Unbonded Tendons**

Kim, Kyungmin

Department of Architecture and Architectural Engineering  
College of Engineering  
Seoul National University

Recently, strands with strengths of 2160 MPa and 2400 MPa were developed in Korea in 2008 and 2011, respectively, and newly recognized in Korean Standard (KS) D 7002. In spite of the potential benefits of using 2400 MPa strands in prestressed concrete structures, there have been very limited researches and verifications that assure the feasibility and application of the newly developed very high-strength strands. Accordingly, experiments on the flexural behavior of seven 2-span unbonded post-tensioned beams were conducted under 4-point static loading condition to verify the feasibility of using 2400 MPa strands in a manner consistent with the application of 1860 MPa strands in post-tensioned beam members. The variables considered in the test included the strand type, the height of tendon profile, and the amount of prestress. Ordinary high-strength strands were applied to three of the specimens and very high-strength strands were applied to the other four

specimens. The specimens with the very high-strength strands exhibited satisfactory performance developing the equivalent prestress increment, member strength, and ductility while having a bit earlier and wider plastic hinge length at ultimate. Test results also demonstrated that secondary moment increased greatly from the beginning of the loading stage while the internal moment at interior support became constant soon after the first hinge occurred at negative moment region. According to the derived results, the conventional methodology of calculating secondary moment tended to quite underestimate the value at the nonlinear and ultimate behavioral range.

**Keywords : 2400 MPa strand, unbonded post-tensioned beams, prestress at nominal flexural strength ( $f_{ps}$ ), secondary moment.**

**Student Number : 2016-26786**

# Contents

<b>Abstract</b> .....	<b>i</b>
<b>Contents</b> .....	<b>iii</b>
<b>List of Tables</b> .....	<b>viii</b>
<b>List of Figures</b> .....	<b>ix</b>
<b>List of Symbols</b> .....	<b>xi</b>
<b>Chapter 1. Introduction</b> .....	<b>1</b>
1.1 Introduction.....	1
1.2 Scope and objectives.....	3
1.3 Organization.....	3
<b>Chapter 2. Review of Previous Studies and Codes</b> .....	<b>5</b>
2.1 Prestress at nominal flexural strength ( $f_{ps}$ ).....	5
2.2 Current design codes.....	8
2.2.1 Allowable stress design .....	8
2.2.2 Strength design .....	10
2.2.3 Load balancing method .....	10
2.2.4 Anchorage zone design.....	13
2.3 Application of very high-strength (2400 MPa) strands .....	15
2.4 Continuity of PT beams with unbonded tendons.....	16
2.5 Discussion.....	17
<b>Chapter 3. Specimens Program</b> .....	<b>20</b>

3.1 Specimen dimension .....	20
3.1.1 Span .....	20
3.1.2 Section .....	23
3.2 Member design .....	23
3.3 Anchorage zone design .....	27
3.4 Tendon profile design .....	27
3.5 Discussion .....	29
<b>Chapter 4. Construction, Test Setup and Testing.....</b>	<b>30</b>
4.1 Specimen construction .....	30
4.2 Material property and anchorage components .....	33
4.2.1 Strand .....	33
4.2.2 Concrete and steel .....	36
4.2.3 Anchorage components .....	39
4.3 Test setup and measurement .....	40
4.3.1 Test setup .....	40
4.3.2 Measurement plan .....	41
4.3.3 Strain gauge plan .....	42
4.4 Discussion .....	43
<b>Chapter 5. Monitoring Prestress Loss.....</b>	<b>45</b>
5.1 Immediate elastic losses .....	45
5.1.1 Elastic shortening .....	45
5.1.2 Anchorage slip .....	46
5.1.3 Friction losses .....	47
5.2 Time dependent losses .....	49
5.3 Discussion .....	50
<b>Chapter 6. Loading Test Result and Analysis.....</b>	<b>52</b>
6.1 Prestress variation .....	52

6.1.1 Prestress during loading test.....	52
6.1.2 Prestress in member.....	53
6.1.3 Prestress at nominal flexural strength ( $f_{ps}$ ).....	54
6.2 Moment variation.....	55
6.2.1 Static analysis.....	56
6.2.2 Moment variation .....	59
6.2.3 Data filtering .....	63
6.3 Member strength evaluation .....	64
6.3.1 Hinge model .....	64
6.4 Discussion.....	70
<b>Chapter 7. Assessment of Applicability of 2400 MPa Strands.....</b>	<b>72</b>
7.1 Applicability of 2400 MPa strands .....	72
7.2 Material property .....	73
7.3 Equivalent plastic hinge length.....	76
7.4 Plastic hinge collapse mechanism assessment.....	81
7.5 Discussion.....	85
<b>Chapter 8. Evaluation of Secondary Moment.....</b>	<b>88</b>
8.1 Secondary moment .....	88
8.2 Secondary moment estimation.....	89
8.2.1 Flexural behavior at the interior support location .....	89
8.2.2 Evaluation of secondary moment .....	93
8.2.3 Secondary moment results and discussion .....	98
8.3 Discussion.....	103
<b>Chapter 9. Conclusion.....</b>	<b>105</b>
<b>References .....</b>	<b>108</b>

<b>Appendix A : Final drawings.....</b>	<b>112</b>
<b>Appendix B : Prestress variation during jacking and seating.....</b>	<b>117</b>
<b>Appendix C : Prestress distribution at different stages</b>	<b>122</b>
<b>Appendix D : Zone identification.....</b>	<b>127</b>
<b>Appendix E : Steel strain gauge data .....</b>	<b>132</b>
<b>국 문 초 록.....</b>	<b>137</b>



## List of Tables

<b>Table 2-1</b> Selected equations for predicting $f_{ps}$ .....	6
<b>Table 2-2</b> Classification of prestressed flexural members (ACI 318-14).....	8
<b>Table 2-3</b> Strand classification in KS D 7002 .....	15
<b>Table 3-1</b> Test specimen details .....	25
<b>Table 4-1</b> Concrete cylinder test results .....	36
<b>Table 4-2</b> Steel test results .....	38
<b>Table 5-1</b> Measured prestress loss due to elastic shortening from the firstly jacked tendons .....	45
<b>Table 5-2</b> Prestress measured from load cells at different stages.....	48
<b>Table 6-1</b> Prestress measured at load cells for different stages.....	55
<b>Table 7-1</b> Equivalent plastic hinge length calculation sheet .....	79

## List of Figures

<b>Figure 2-1</b> Equivalent loads and moments produced by prestressing tendons (Nilson, 1987) .....	12
<b>Figure 2-2</b> Local and general zones (ACI 318-14) .....	14
<b>Figure 3-1</b> Reference design of 2-span PT beam (NH IT Center, Constructed in 2015) .....	22
<b>Figure 3-2</b> Specimen detail (Unit: mm).....	26
<b>Figure 3-3</b> Anchorage zone design (Specimen D3H) .....	27
<b>Figure 3-4</b> Tendon profile shape (I.P: inflection point; Unit: mm).....	28
<b>Figure 4-1</b> Manufacturing process.....	31
<b>Figure 4-2</b> Steel reinforcement detail .....	32
<b>Figure 4-3</b> Stress-strain curves of strand samples.....	34
<b>Figure 4-4</b> Failure of strand samples .....	35
<b>Figure 4-5</b> Concrete cylinder and test.....	37
<b>Figure 4-6</b> Stress-strain curves of mild steel.....	38
<b>Figure 4-7</b> Mild steel sample test.....	39
<b>Figure 4-8</b> Prestressing steel sample test .....	39
<b>Figure 4-9</b> Two-span beam test (Unit: mm).....	40
<b>Figure 4-10</b> Test setup .....	41
<b>Figure 4-11</b> Strain gauge locations .....	42
<b>Figure 4-12</b> Strain gauge locations (Unit: mm) .....	43
<b>Figure 5-1</b> Stress variation during jacking and anchor slip (D3H) .....	46
<b>Figure 5-2</b> Prestress variation profile.....	49
<b>Figure 6-1</b> Prestress variation during loading test (D3H) .....	52
<b>Figure 6-2</b> Member prestress distribution profile at different stages (D3H).....	54
<b>Figure 6-3</b> Free body diagrams using method of sections (Unit: mm) .....	57
<b>Figure 6-4</b> Moment-deflection curves at critical sections ( $M_I$ is presented in absolute value).....	63
<b>Figure 6-5</b> Hinge model for strength evaluation (Unit: mm).....	65
<b>Figure 6-6</b> Load-deflection curves.....	68
<b>Figure 6-7</b> Tendon fracture (B4H) .....	70
<b>Figure 7-1</b> Stress-strain curves of 1860 MPa and 2400 MPa strand samples .....	74

<b>Figure 7-2</b> Normalized stress-strain curves of 1860 MPa and 2400 MPa strand samples .....	74
<b>Figure 7-3</b> Curvature distribution of simply supported beam (Harajli, 1990) .....	76
<b>Figure 7-4</b> Failure pattern in unbonded members and strain distribution at critical section (Harajli, 2006) .....	78
<b>Figure 7-5</b> Prestress variation measured at jacking ends and fixed ends .....	81
<b>Figure 7-6</b> Plastic collapse mechanism with different hinge length .....	82
<b>Figure 7-7</b> Rotation-deflection curves .....	83
<b>Figure 7-8</b> Strain measured at the reinforcing bar in tension at the interior support .	84
<b>Figure 7-9</b> Crack pattern comparison between B4L and D3L .....	85
<b>Figure 8-1</b> Secondary reactions and moments (Aalami, 1990).....	89
<b>Figure 8-2</b> Secondary moment diagram.....	90
<b>Figure 8-3</b> Member behavior depending on different loading stages .....	91
<b>Figure 8-4</b> Behavior zone identification of the Specimen D3H.....	94
<b>Figure 8-5</b> Stress states of the concrete section at the interior support location .....	95
<b>Figure 8-6</b> Secondary moment curves with the calculated moments.....	102
<b>Figure A-1</b> Details of Specimen B4H (Unit: mm) .....	113
<b>Figure A-2</b> Details of Specimen B4L (Unit: mm).....	113
<b>Figure A-3</b> Details of Specimen B5L (Unit: mm).....	114
<b>Figure A-4</b> Details of Specimen D3H (Unit: mm).....	114
<b>Figure A-5</b> Details of Specimen D3L (Unit: mm) .....	115
<b>Figure A-6</b> Details of Specimen D4H (Unit: mm).....	115
<b>Figure A-7</b> Details of Specimen D4L (Unit: mm) .....	116
<b>Figure B-1</b> Prestress variation measured during jacking at jacking and fixed ends.	121
<b>Figure C-1</b> prestress distribution profile at different stages.....	126
<b>Figure D-1</b> Behavior zone identification of the specimens.....	131
<b>Figure E-1</b> Strain measured at the reinforcing bar in tension at the interior support	136

## List of Symbols

$A_{ps}$	area of prestressing longitudinal tension reinforcement, mm <sup>2</sup>
$A_s$	area of nonprestressed longitudinal tension reinforcement, mm <sup>2</sup>
$A_{tr}$	sectional area of the transformed concrete section, mm <sup>2</sup>
$a$	depth of equivalent rectangular stress block, mm
$b$	width of the compression face of the member, mm
$b_w$	width of member's web, mm
$c$	distance from extreme compression fiber to neutral axis, mm
$c^*$	distance from extreme compression fiber to neutral axis based on $f_{ps\_exp}^*$ , mm
$d$	distance from extreme compression fiber to centroid of nonprestressed reinforcement, mm
$d_p$	distance from extreme compression fiber to centroid of prestressing reinforcement, mm
$d_s$	distance from extreme compression fiber to centroid of longitudinal tension mild steel reinforcement, mm
$E_c$	modulus of elasticity of concrete, MPa
$E_p$	modulus of elasticity of prestressing reinforcement, MPa
$E_s$	modulus of elasticity of mild steel reinforcement and structural steel, excluding prestressing reinforcement, MPa
$e$	eccentricity from c.g.c. to the center of prestressing force, mm

$f_{a,j}$	measured prestress right after anchor set at the jacking end, MPa
$f'_c$	specified compressive strength of concrete, MPa
$f_{i,j}$	measured prestress at jacking stage at the fixed end, MPa
$f_{j,j}$	measured prestress at jacking stage at the jacking end, MPa
$f_p$	evaluated prestress based on the measured prestress at the jacking end and the derived prestress distribution profile, MPa
$f_{ps}$	stress in prestressing reinforcement at nominal (in this study, at peak load) flexural strength, MPa
$f_{ps-AASHTO}$	$f_{ps}$ computed by using the equation provided in AASHTO (2017), MPa
$f_{ps-ACI}$	$f_{ps}$ predicted by using the equation provided in ACI 318-14, MPa
$f_{ps.exp}$	$f_{ps}$ based on the measured data and the derived prestress profile at peak load, MPa
$f_{ps.exp}^*$	modified $f_{ps.exp}$ considering the strain hardening effect based on the evaluated strain increment and stress-strain curves, MPa
$f_{ps.Harajli}$	$f_{ps}$ evaluated by using the equation suggested by Harajli (2006), MPa
$f_{ps.Naaman}$	$f_{ps}$ evaluated by using the equation suggested by Naaman et al. (2002), MPa
$f_{ps-j}$	measured prestress at the peak load at the jacking end, MPa
$f_{pu}$	specified tensile strength of prestressing reinforcement, MPa
$f_{py}$	specified yield strength of prestressing reinforcement, MPa
$f_r$	modulus of rupture of concrete, MPa
$f_s$	tensile stress in reinforcement at service loads, excluding prestressing reinforcement, MPa

$f_{se}$	effective stress in prestressing reinforcement, after allowance for all prestress losses, MPa
$f_{se,f}$	measured prestress at effective stage at the fixed end, MPa
$f_{se,j}$	measured prestress at effective prestress stage at the jacking end, MPa
$f_t$	extreme fiber stress in the tension zone calculated at service loads using gross section properties after allowance of all prestress losses, MPa
$f_u$	specified tensile strength of nonprestressed reinforcement, MPa
$f_y$	specified yield strength for nonprestressed reinforcement, MPa
$h_f$	compression flange depth, mm
$I$	moment of inertia of the transformed section of concrete, mm <sup>4</sup>
$k$	factor which is 0.255 for the high tendon profile and 0.166 for the low tendon profile
$L$	measured reaction force at the interior support, kN
$L_a$	length of tendon between anchors, mm
$L_p$	equivalent plastic hinge length, mm
$L_p^*$	equivalent plastic hinge length based on $f_{ps\_exp}^*$ , mm
$L$	span net length, mm
$l_e$	effective tendon length, mm
$M_{bal}$	balanced moment by prestressing force, kN-m
$M_{bal,ser}$	balanced moment by prestressing force at service load stage, kN-m

$M_{bal.tr}$	balanced moment by prestressing force at transfer, kN-m
$M_I$	Measured internal moment using load cell data at the interior support location, kN-m
$M_{cr}$	total moment required to make the first crack at the interior support section, kN-m
$M_D$	moment produced by superimposed dead load, kN-m
$M_E$	measured internal moment using load cell data at the maximum internal positive moment location, 4.55 m east of the interior support, kN-m
$M_L$	moment produced by live load, kN-m
$M_{self}$	moment produced by self-weight of the member, kN-m
$M_W$	measured internal moment using load cell data at the maximum positive moment location, 4.55 m west of the interior support, kN-m
$M_{@fp}$	plastic moment calculated based on the measured $f_p$ , kN-m
$M_1$	primary moment ( $= Pe$ )
$M_2$	secondary moment, kN-m
$M_{2,I}$	secondary moment at the interior support location, kN-m
$M_{2,E}$	secondary moment at the critical section on the east span ( $= 0.336M_{2,I}$ ), kN-m
$M_{2,W}$	secondary moment at the critical section on the west span ( $= 0.336M_{2,I}$ ), kN-m
$M_{2,I,calc}$	secondary moment at the interior support location which is calculated by using load balancing method, kN-m
$P$	prestressing force in the section of interest, kN
$P_E$	half of the actuator force on the east side, kN

$P_e$	prestressing force at service load stage, kN
$P_i$	prestressing force at transfer, kN
$P_W$	half of the actuator force on the west side, kN
$R_E$	reaction force at the end support on the east side, kN
$R_W$	reaction force at the end support on the west side, kN
$P_0$	point load applied by an actuator until the member barely touches the interior support under zero gravity atmosphere, kN
$P_1$	point load applied by an actuator until the first crack occurs at the interior support location, kN
$P_2$	point load applied by an actuator until the reinforcing bars in tension at the interior support location firstly yields, kN
$T_x$	prestressing force at point $x$ , kN
$t_s$	time interval of the measurement, second
$V_1$	shear force presented in <b>Figure 6-1</b> , kN
$V_2$	shear force presented in <b>Figure 6-1</b> , kN
$w$	uniform line load of gravity due to self-weight applied throughout the beam, kN/m
$x$	length of tendon from stressing end to point $x$ , m
$x_n$	raw data at $n$ second
$Y$	distance from the elastic centroid of the gross section to the stress point, mm
$y_n$	filtered value at $n$ second

$\alpha$	total angular change in radians from jacking end to point $x$ , (rad)
$\beta_l$	ratio of the depth of the equivalent uniformly stressed compression zone assumed in the strength limit state to the depth of the actual compression zone
$\Delta_{cr}$	total deflection in the elastic behavior zone, mm
$\Delta f_{ps,j}$	measured prestress increment between effective stage and nominal stage at the jacking end, MPa
$\Delta_x$	displacement generated by actuator load, mm
$\Delta \epsilon_{ps}$	increase in strain in prestressing steel above effective prestrain (based on the data measured at the jacking end)
$\epsilon_{ce}$	concrete pre-compression strain
$\epsilon_{cu}$	ultimate concrete compression strain
$\kappa$	wobble friction coefficient per unit length of tendon, $m^{-1}$
$\mu$	curvature friction coefficient
$\rho$	ratio of $A_s$ to $bd$
$\rho_p$	ratio of $A_{ps}$ to $bd_p$
$\sigma_{ser}$	extreme concrete fiber stress under consideration at service load stage, MPa
$\sigma_{tr}$	extreme concrete fiber stress under consideration at transfer, MPa
$\tau$	time constant
$\phi$	strength reduction factor
$\phi_1$	curvature discrepancy of the concrete section at the interior support between Stage 1 and Stage 2

$\psi$	ratio of the equivalent plastic hinge length $L_p$ to the neutral axis depth $c$
$\Omega_u$	strain-reduction coefficient which is the ratio of strain increase in the unbonded tendon to that of the equivalent bonded tendon at the section of maximum moment, at nominal bending resistance



# Chapter 1. Introduction

## 1.1 Introduction

The advances in materials such as high-strength concrete with a strength over 100 MPa and steel with high strengths have allowed engineers to make challenges for innovative structural design. For prestressed concrete structures, current practice for the strength of strands has remained 1860 MPa over the past several decades. For this reason, many researches and code developments have been made only on the basis of this strength of strand. Recently, strands with strengths of 2160 MPa and 2400 MPa were developed in Korea in 2008 and 2011, respectively, and newly recognized in Korean Standard (KS) D 7002. The criteria specify the very high-strength strands of 2160 MPa and 2400 MPa using designation of SWPC7CL and SWPC7DL, respectively having the same geometry, size, weight, and elastic modulus as those of the ordinary high-strength strands with 1860 MPa strength.

Kim et al. (2012) revealed in their study that the cost of construction could be reduced by 8% and 10% if the strands with 2160 and 2400 MPa were used, respectively. Using very high-strength strands would lead to cost-effective solution, increasing constructability by using less prestressing sectional area, prestressing components (anchorage, ducts, wedges, etc.) and workforce. Apparently, the use of very high-strength strands for prestressed concrete structures offers undeniable advantages.

Reportedly, the first so-called “very high-strength” strands were first developed in the early 2000s in Japan and were applied to an overhead

walkway in Tokyo in 2006. But it has not been actively commercialized since then. Also, there have been several types of research on using very high-strength strands of 2069 MPa conducted in the Virginia Polytechnic Institute and State University, US (Hill, 2006; and Carroll, 2009). Recently, there have been several experimental and analytical studies verifying the use of very high-strength strands in pre-tensioned concrete members in Korea (Park et al., 2016; Jeon et al., 2016; Yim et al., 2015; Yang et al., 2015; and Park et al., 2012).

The majority of the studies, however, was focused on using the very high-strength strands to bonded systems and researches about applying very high-strength strands to unbonded post-tensioned systems appear almost nonexistent. Unbonded prestressed concrete construction is increasingly used for girders, beams, and flat slabs, as well as nuclear containment structures. Furthermore, performing a verification test for post-tensioned structures with unbonded tendons is highly necessary because prestressed concrete members with bonded and unbonded tendons show similar behavioral characteristics at the working stage, but their behaviors in the plastic stage are distinctively different. This is because unbonded tendons in prestressed concrete members behave in a member dependent way whereas tendons in bonded systems rely on the local compatibility of the individual section. In other words, behavior of unbonded tendons is closely related to the compatibility between the tendon elongation and the overall deformation of the concrete member.

In order to assess the behavior of multi-span unbonded beam systems with ordinary and very high-strength strands, a total of seven 2-span post-tensioned beam specimens were tested, analyzed, and discussed in terms of their flexural behavior. The prestress variation depending on different loading

stages, including the stress in prestressing reinforcement at nominal flexural strength ( $f_{ps}$ ), was investigated. Also, variation of the secondary moment of the specimens was evaluated during load testing.

## **1.2 Scope and objectives**

The main purpose of this study is to investigate behavior and performance of unbonded post-tensioned concrete beams with very high-strength strands. Seven 2-span beam specimens were constructed for comparison, where three of them were prestressed with ordinary 1860 MPa strength strands and four of them were prestressed with 2400 MPa strands. All specimens were designed on the basis of a 3-span post-tensioned girder design used in an existing building. The specimens were designed following ACI 318-14 and PTI M50.2-00: Anchorage Zone Design. From the experiment, various features of post-tensioned concrete members were revealed and investigated: prestress loss, prestress variation according to different stages, stress in prestressing reinforcement at nominal flexural strength ( $f_{ps}$ ), member strength, moment variation at each critical section during loading test, and secondary moment.

## **1.3 Organization**

This thesis is composed of eight main chapters. The introduction, purpose and scope are shown briefly in Chapter 1. Relevant design codes and previous studies that are directly or indirectly related to the application of unbonded tendons to flexural members are reviewed in Chapter 2. Design process including details of seven specimens and construction process is shown in Chapter 3. Chapter 4 contains test setup, material's properties, prestressing procedure, loading plan and measuring instrument plan. More detailed results

observed during prestressing are discussed in Chapter 5. The main loading test results and discussion of seven specimens are described and compared in Chapter 6. In Chapter 7, feasibility assessment is conducted for applying high-strength strands to unbonded post-tensioned concrete flexural members. In Chapter 8, the developed methodology to evaluate secondary moment and the secondary moment evaluated in each specimen are presented and discussed. Finally, conclusions are given in Chapter 9.

## Chapter 2. Review of Previous Studies and Codes

### 2.1 Prestress at nominal flexural strength ( $f_{ps}$ )

From the viewpoint of applying high-strength strands to the post-tensioned flexural members with unbonded tendons, predicting accurate prestress of the high-strength strand at the flexural nominal state of the member ( $f_{ps}$ ) is highly important because  $f_{ps}$  significantly affects the flexural strength of post-tensioned beam members. Generally, the stress of an unbonded tendon at ultimate state or at nominal strength ( $f_{ps}$ ) is expressed as a sum of effective stress ( $f_{se}$ ) and stress increment ( $\Delta f_{ps}$ ). The stress of tensile reinforcement and bonded prestressed reinforcement can be computed by using strain compatibility method of sections under consideration. But predicting the prestress of unbonded tendons at nominal flexural strength cannot be computed in the same manner because the behavior of unbonded tendons is related to the compatibility between tendon elongation and overall deformation of the concrete member.

A number of experimental studies and analytical approaches have been made to evaluate the stress of unbonded tendons in prestressed flexural members. It has been reported in various studies that the equations specified in ACI Building Code (ACI 318-14), Section 20.3.2.4.1 do not provide reasonable values for  $f_{ps}$  in the strands when they are compared with the experimental results. Additionally, despite the extensive studies on  $f_{ps}$ , most of the proposed equations or expressions do not seem to find common ground to share in respect of the way that the primary parameters are applied. Up to the present,

comprehensive literature reviews on  $f_{ps}$  have been conducted by scholars such as Naaman and Alkhairi (1991), Allouche et al. (1998), Lee et al. (1999), Au and Du (2004), Harajli (2006), and so on. Over the years, a number of experimental works have been made and different forms of equations have been proposed to evaluate stress in unbonded tendons ( $f_{ps}$ ) at nominal. Selected equations suggested by the past researchers and some code specifications are presented in **Table 2-1**.

**Table 2-1** Selected equations for predicting  $f_{ps}$

Year	Reference	Equations	Eq. No.
2014	ACI 318-14	$f_{ps} = f_{se} + 10,000 + \frac{f'_c}{100\rho_p} \text{ (psi)}$ <p>for <math>l / d_p \leq 35</math></p> $f_{ps} = f_{se} + 10,000 + \frac{f'_c}{300\rho_p} \text{ (psi)}$ <p>for <math>l / d_p &gt; 35</math></p>	(2-1)
2017	AASHTO	$f_{ps} = f_{se} + 900 \left( \frac{d_p - c}{l_e} \right) \leq f_{py} \text{ (ksi)}$ $l_e = \left( \frac{2L_a}{2 + N_s} \right)$ $c = \frac{A_{ps}f_{ps} + A_s f'_s - A'_s f'_s - 0.85f'_c (b - b_w)h_f}{0.85f'_c \beta_1 b_w}$ <p>for rectangular section</p> <p>where, <math>l_e</math> is the effective tendon length; <math>L_a</math> is the length of tendon between anchorages; and <math>N_s</math> is the number of support hinges crossed by the tendon between anchorages or discretely bonded points</p>	(2-2)
1976	Tam and Pannel	$f_{ps} = f_{se} + E_p \varepsilon_{cu} \psi \left( \frac{d_p - c}{l} \right)$ $c = \frac{(f_{pe} + 10.5E_p \varepsilon_{cu} d_p / L)A_{ps} + A_s f'_y - A'_s f'_y - 0.85f'_c (b - b_w)h_f}{0.85\beta_1 f'_c b_w + 10.5E_p \varepsilon_{cu} A_{ps} / l}$	(2-3)

		where, $A'_s$ is section area of compression steel; $E_{ps}$ is modulus of elasticity of the prestressing steel; and $\psi$ is the ratio of the equivalent plastic hinge length $L_p$ to the neutral axis depth $c$	
2002	Naaman et al.	$f_{ps} = f_{se} + \Omega_u E_p \varepsilon_{cu} \left( \frac{d_p}{c} - 1 \right) \frac{L_1}{L_2}$ $f_{ps} = f_{se} + 15 \frac{L_1}{L_2} \geq f_{se} + 7.5 \text{ (ksi) (simplified)}$ <p>where,  <math>\Omega_u</math> is the strain-reduction coefficient which is the ratio of strain increase in the unbonded tendon to that of the equivalent bonded tendon at the section of maximum moment, at nominal bending resistance; <math>L_1</math> is the length of loaded span or sum of lengths of loaded spans, affected by the same tendon; and <math>L_2</math> is the length of tendon between end anchorages</p>	(2-4)
2011	Yang and Kang	$f_{ps} = \frac{-B_1 + \sqrt{B_1^2 - 4A_1C_1}}{2A_1} \leq f_{py}$ <p>where,  <math>A_1 = A_p</math>; <math>B_1 = A_s f_y - A'_s f'_y - C_f - A_p f_{pe} + \alpha_f E_p \varepsilon_{cu} A_p</math>; <math>C_1 = \alpha_f E_p \varepsilon_{cu} (A_s f_y - A'_s f'_y - C_f - 0.85 f'_c b_w \beta_1 d_p) - f_{se} (A_s f_y - A'_s f'_y - C_f)</math>; and <math>C_f</math> is simply taken as 0 for a rectangular beam</p>	(2-5)
2012	Harajli	$f_{ps} = f_{se} + \frac{60 N_p}{L_a / d_p} \left( 1 - \frac{c_e}{d_p} \right)$ $c_e = \frac{A_{ps} f_{se} + A_s f_y}{0.85 \beta_1 f'_c b}$ <p>where, <math>N_p</math> is the parameter that combines the effect of member continuity and type of applied load; <math>L_a</math> is the total length of the tendons between anchorages</p>	(2-6)

$A_{ps}$ : area of prestressed longitudinal tension reinforcement;  $A_s$ : area of nonprestressed longitudinal tension reinforcement;  $b$ : the width of the compression face of the member;  $b_w$ : width of member's web  $d_p$ : distance from extreme compression fiber to centroid of prestressing reinforcement  $f'_c$ : specified compressive strength of concrete;  $f_{ps}$ : distance from extreme compression fiber to centroid of prestressing reinforcement;  $f_{py}$ : specified yield strength of prestressing reinforcement;  $f_s$ : tensile stress in reinforcement at service loads, excluding prestressing reinforcement;  $f_{se}$ : effective stress in prestressing reinforcement, after allowance for all prestress losses;  $h_f$ : compression flange depth  $l$ : span length of beam;  $\beta_1$ : ratio of the depth of the equivalent uniformly stressed compression zone assumed in the strength limit state to the depth of the actual compression zone;  $\varepsilon_{cu}$ : ultimate concrete compression strain;  $\rho_n$ : ratio of  $A_{ps}$  to  $bd_p$ .

## 2.2 Current design codes

There are several codes that are related to designing of post-tensioned beams with unbonded tendons. ACI 318-14 covers the basic principle of the design. PTI M50.2-00 and PTI TAB.1-06 provide guidelines for anchorage zone design. ACI 423.10R-16 and PCI Committee on Prestress Losses (1975) offer explanation of how to calculate prestress losses.

### 2.2.1 Allowable stress design

In designing prestressed concrete flexural members, concrete stresses shall be limited in accordance with Sections 24.5.2 through 24.5.4 in ACI 318-14. The concrete stress can be calculated by using the elastic theory where strains vary linearly with distance from neutral axis following strain compatibility and the assumption that concrete resists no tension force.

According to ACI 318-14, Section 24.5.2, prestressed flexural members can be classified as Class U (uncracked), T (transition between uncracked and cracked), or C (cracked). The class is determined based on the extreme fiber stress in tension in the precompressed tension zone calculated at service loads assuming an uncracked section. **Table 2-1** shows the classification.

**Table 2-2** Classification of prestressed flexural members (ACI 318-14)

Assumed behavior	Class	Limitation of $f_i$
Uncracked	$U$	$f_i \leq 7.5\sqrt{f'_c}$
Transition between uncracked and cracked	$T$	$7.5\sqrt{f'_c} < f_i \leq 12\sqrt{f'_c}$
Cracked	$C$	$f_i > 12\sqrt{f'_c}$

$f_i$ : extreme fiber stress in the precompressed tension zone calculated at service loads using gross section properties after allowance of all prestress losses.

The serviceability design requirements are provided in Table R24.5.2.1 of ACI 318-14. The permissible concrete stresses shall be checked at both the transfer stage and service stage. The concrete stresses at transfer are caused by the self-weight of the members and the prestressing force after jacking reduced by the losses due to anchor-set behavior and elastic shortening of the concrete. Anchor-set behavior will be discussed in the later chapters. By using the strain compatibility method as mentioned above, concrete stress at extreme fiber can be calculated by using **Eqs. (2-7) and (2-8)**.

$$\sigma_{tr} = \frac{M_{bal\_tr} + M_{self}}{I_g} y + \frac{P_i}{A_g} \quad (2-7)$$

$$\sigma_{ser} = \frac{M_{bal\_ser} + M_D + M_L}{I_g} y + \frac{P_e}{A_g} \quad (2-8)$$

where,  $\sigma_{tr}$  is the extreme concrete fiber stress under consideration at transfer;  $M_{bal\_tr}$  is the moment produced by equivalent load (load balancing method) due to prestressing force at transfer;  $M_{self}$  is the moment produced by self-weight of the member;  $y$  is the distance from the elastic centroid of the gross section to the stress point;  $P_i$  is the prestressing force at transfer;  $A_g$  is the gross section area;  $\sigma_{ser}$  is the extreme concrete fiber stress under consideration at service load stage;  $M_{bal\_ser}$  is the moment produced by equivalent load due to prestressing force at service load stage;  $M_D$  is the moment produced by superimposed dead load;  $M_L$  is the moment produced by live load; and  $P_e$  is the prestressing force at service load stage.

For designing the specimen, concrete stresses are checked for three different cases: (1) when the specimens are in zero-gravity state without any external loads and this is to take into account the initial condition of the specimens

where concrete is cast and cured on the flat bed; (2) the specimens are lifted up by the lifting hooks; and (3) the specimens are placed on the supports.

### 2.2.2 Strength design

Obtaining permissible stresses in concrete does not mean that adequate design strength is secured: Member strength should be checked as well. According to Section 5.3.11 of ACI 318-14, required strength should include internal load effects due to reactions induced by prestressing with a load factor of 1.0. The internal load effects due to reactions induced by prestressing forces are secondary moments. Since these moments (or loads) are applied externally, this effect should be considered in the load combination of strength design. Nominal flexural strength of the member section can be calculated by using Eq. (2-9).

$$\phi M_n = 0.9 \left\{ f_{ps} A_{ps} \left( d_p - \frac{a}{2} \right) + f_y A_s \left( d_s - \frac{a}{2} \right) \right\} \quad (2-9)$$

where,  $f_{ps}$  is the stress in prestressing reinforcement at nominal;  $A_{ps}$  is the area of prestressed longitudinal tension reinforcement;  $d_p$  is the distance from extreme compression fiber to centroid of prestressing reinforcement;  $A_s$  is the area of nonprestressed longitudinal tension reinforcement;  $f_y$  is the specified yield strength for nonprestressed reinforcement;  $a$  is the depth of the concrete stress block at the ultimate state is the extreme concrete fiber stress under consideration, and  $d_s$  is the distance from extreme compression fiber to centroid of nonprestressed reinforcement.

### 2.2.3 Load balancing method

The load balancing method is one of the most widely used methods to design

post-tensioned concrete beams and slabs which was introduced by Lin (1963). It has been widely accepted as a predominant method for analyzing post-tensioned members. In this method, a portion of design load is selected to be balanced load, which is induced by prestressing force to concrete. In combination with other external design loads, the member is then analyzed with the equivalent set of prestressing force acting on the member. The balanced load is usually taken as 80% of the dead load or greater.

In this analysis, tendons in the members are removed and replaced with the forces the tendon exerts on the structure and this forces can be derived as equivalent forces. A few examples of equivalent forces depending on different tendon profile shapes are illustrated in **Figure 2-1**. This equivalent forces from the prestressing tendons results in the action and reaction between the prestressing steels and concrete, redistributing the concrete stress in a beneficial way against the demanded loads. Note that this equivalent loads (balanced loads) are not external forces, but they reveal the force equilibrium between the prestressing tendons and the concrete member. If the structure is a statically indeterminate structure, there could be a secondary effect which acts as an external force.

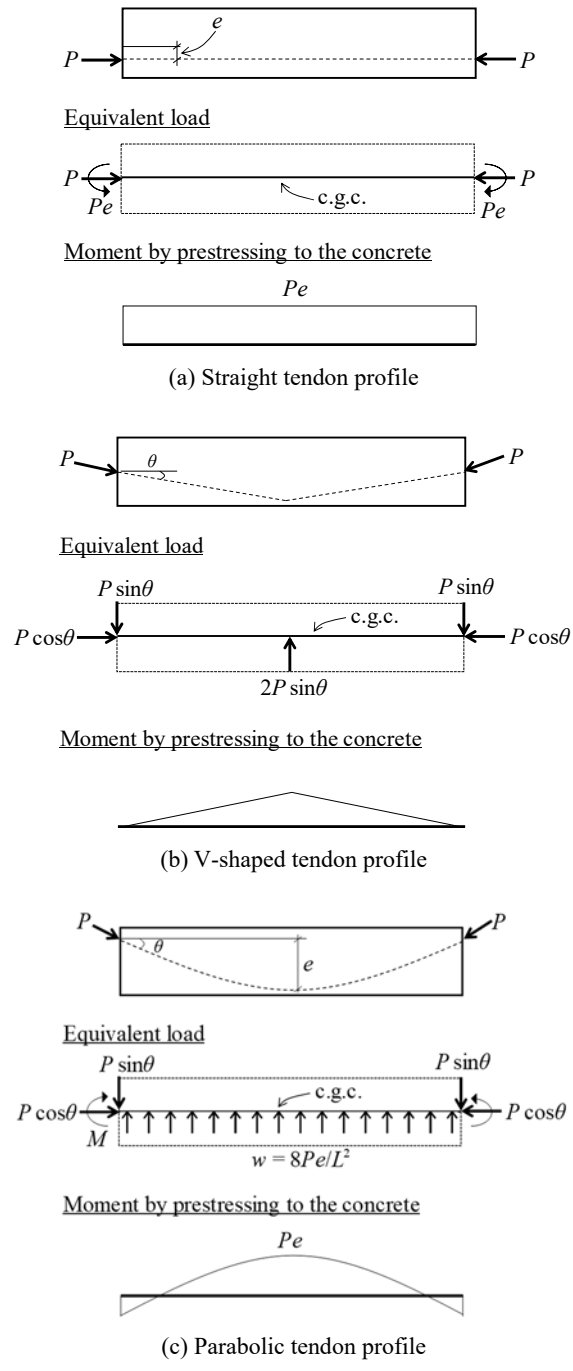


**Figure 2-1** Equivalent loads and moments produced by prestressing tendons (Nilson, 1987)

By using the load balancing method, secondary effects of the indeterminate structures can be evaluated. The secondary moment at a particular section of the member is defined as the difference between the balanced load moment and the primary moment as presented in **Eq. (2-10)**. Primary moment can be calculated as  $Pe$ , where  $P$  is the prestressing force in the section of interest, and  $e$  is the eccentricity from c.g.c. to the center of prestressing force. More detailed investigation on the secondary moment will be covered in Chapter 8.

$$\text{Secondary Moment} = M_{bal} - M_I \quad (2-10)$$

where,  $M_{bal}$  is the balanced moment by prestressing force; and  $M_I$  is the primary moment.

#### **2.2.4 Anchorage zone design**

Anchorage zone can be classified into two zones: local zone and general zone. ACI 318-14 and PTI M50.2-00: Anchorage Zone Design specifies the design method for both zones. The local zone, which is generally assumed as a rectangular prism, surrounds the anchorage device and any confining reinforcement. The general zone includes the local zone and the portion of the concrete member through which the concentrated prestressing force is transferred to the concrete and distributed more uniformly across the section (ACI 318-14). The extent or range of local and general zones may differ depending on the type of code provisions. **Figure 2-2** illustrates the identification of the local and general zones according to ACI 318-14.

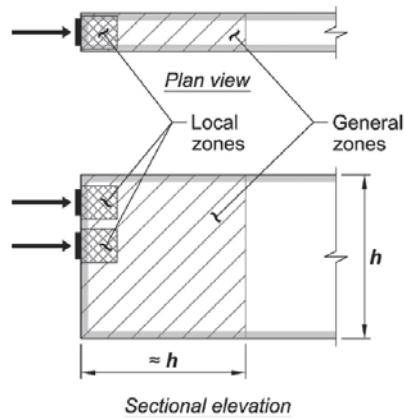


**Figure 2-2** Local and general zones (ACI 318-14)

For post-tensioned anchorage zone design, a load factor of 1.2 shall be applied to the maximum prestressing reinforcement jacking force according to ACI 318-14, Section 5.3.12.

Local zone design should be carried out carefully since the local zone resists very high local stresses introduced by anchorage such as anchor plate and transfers them to the remainder of the anchorage zone as a form of bearing pressure. If special anchorage devices are used, the supplier should provide information about the required conditions for applying the device.

For the design of general zone, there are three possible analysis approaches that are recommended: strut-and-tie models, linear stress analysis, or by using the simplified equations provided in AASHTO (2017). From the analysis, required strength against bursting force can be computed and additional hairpin bars may be placed to resist the bursting force.

### 2.3 Application of very high-strength (2400 MPa) strands

Strands with strengths of 2160 MPa and 2400 MPa were developed in Korea in 2008 and 2011, respectively, and newly recognized in Korean Standard (KS) D 7002. The criteria specifies the very high-strength strands of 2160 MPa and 2400 MPa using designation of SWPC7CL and SWPC7DL, respectively, having the same geometry, size, weight, and elastic modulus to the ordinary strands with 1860 MPa strength. Table 2-3 Shows the classification of the strands in KS.

**Table 2-3** Strand classification in KS D 7002

Type	Class	Nominal diameter (mm)	Area (mm <sup>2</sup> )	Unit weight (kgf/km)	Steel Yield force (kN)	Tensile load (0.2% permanent elongation, kN)
A	SWPC 7A	9.3	51.61	405	88.8	75.5
		10.8	69.68	546	120	102
		12.4	92.9	729	160	136
		15.2	138.7	1101	240	204
B	SWPC 7B	9.5	54.84	432	102	86.8
		11.1	74.19	580	138	118
		12.7	98.71	774	183	156
		15.2	138.7	1101	261	222
C	SWPC 7CL	12.7	98.71	774	214	182
		15.2	138.7	1101	300	255
D	SWPC 7DL	12.7	98.71	774	237	202
		15.2	138.7	1101	333	283

ACI 318-14 specifies that prestressing reinforcement of strand shall conform to ASTM A416-06. But ASTM A416-06 does not include the strands with very high strength of 2160 MPa or 2400 MPa in the criteria. This implies that there is no solid evidence to make sure that replacing ordinary high-strength

strands with very high-strength strands would be acceptable. So, it would be highly necessary to conduct verifying tests and researches to evaluate the validity of the current code provisions to be applied to the very high-strength strands.

For flexural members such as beams to display satisfactory performance, three main features should be satisfied properly: sufficient strength, stiffness and ductility. This means that if tendons in the members which are originally prestressed with ordinary high-strength unbonded tendons are replaced with equivalent or smaller number of very high-strength strands, the members still should develop the same level of strength and ductility. The aforementioned “equivalent number of very high-strength strands” is determined when the member is designed in the same manner using the same code requirements and equations, but with different strand type. If the same level of strength and ductility is proved to be developed in this case, applying very high-strength strands to the flexural prestressed members with unbonded tendons could be acceptable. If not, revision of the guidelines should be needed for using very high-strength strands.

## **2.4 Continuity of PT beams with unbonded tendons**

Experimental studies have been conducted on continuous prestressed concrete beams and one-way slabs over the years by numerous researchers: Hemakom (1970), Chen (1971), Mattock et al. (1971), Burns et al. (1978), Zhou and Zheng (2014), Maguire et al. (2016), and so on. Considering the member continuity of the unbonded post-tensioned beams is important because the variation of the stress of prestressed reinforcement is dependent on the overall member behavior. Harajli (2012) pointed out in his study that the factors that

contribute to the inaccuracies in the prediction of the stress in unbonded tendons at ultimate include the difficulty in evaluating the spread of plasticity due to the development of localized flexural cracks, the assumption of a linear relationship between steel stress and steel strain at strain levels close to yield, and most importantly the neglect of the effect of member continuity. The studies conducted by Burns et al. (1978), Naaman and Alkhairi (1991), and Naaman et al. (2002) also showed that the tendon stress is affected by the number of loaded spans or the number of the tension yielding zones that the tendon passes through. According to Burns et al. (1978), the increase in strain or stress in the prestressing steel tends to diffuse by “escaping” or “slipping” from the loaded span(s) to the unloaded spans in continuous members in which one or few spans are loaded (pattern loading) to produce maximum moments at the critical sections, and in the process of forming a collapse mechanism. Also, the study conducted by Kang and Wallace (2008) revealed that the number of slab-column connections in the post-tensioned system affects the variation of tendon stresses.

However, the current ACI 318 code equation for predicting  $f_{ps}$  does not consider the member continuity. Harajli pointed out in his study (2006) that there are two major limitations in the current ACI equation (**Eq. (2-1)**): 1) ACI 318 neglects the effect of bonded tension reinforcement, and 2) ACI 318 does not consider the effect of multi-span systems or loading pattern in continuous members. On the contrary, **Eq. (2-2)** provided in AASHTO (2017) adopted this concept.

## **2.5 Discussion**

In this chapter, previous studies on prestress of unbonded tendons at nominal

( $f_{ps}$ ) and continuous unbonded post-tensioned flexural members were reviewed. Also, code reviews on designing unbonded post-tensioned members were conducted from the point of applying very-high strength (2400 MPa) strands. The major contents are summarized as follows:

- 1) Predicting accurate  $f_{ps}$  is highly important because  $f_{ps}$  significantly affects the flexural strength of post-tensioned flexural members in strength calculation. Nonetheless predicting  $f_{ps}$  has been a very complicated issue because the stress increase in the unbonded tendons cannot be determined by cross section, but the overall deformation of the concrete member.
- 2) Despite the extensive studies on  $f_{ps}$  in unbonded tendons, most of the proposed equations or expressions do not seem to find common ground to share in respect of the way that the primary parameters are applied, and when it comes to post-tensioned members with multi-spans the problem becomes even more complicated.
- 3) For designing the specimens, both allowable stress design and strength design were considered as per ACI 318-14. For both design methods, load balancing method was used to calculate the stress of critical points and evaluate the secondary effect to be considered in the load combination.
- 4) Code review was conducted in the view of using 2400 MPa strands. In respect of code specification, only the Korean Standard D 7002 newly recognizes 2400 MPa strands. But there is no other clue or ground in any code specification about using tendons with higher strengths.
- 5) Literature review was conducted in the view of using 2400 MPa strands. It was learned that there have been some experimental and analytical

studies on the application of higher strength strands in Korea, Japan and the US. The majority of the studies, however, were focused on using the higher strength strands to bonded systems, and researches about applying very high-strength strands to unbonded post-tensioned systems appear almost nonexistent.

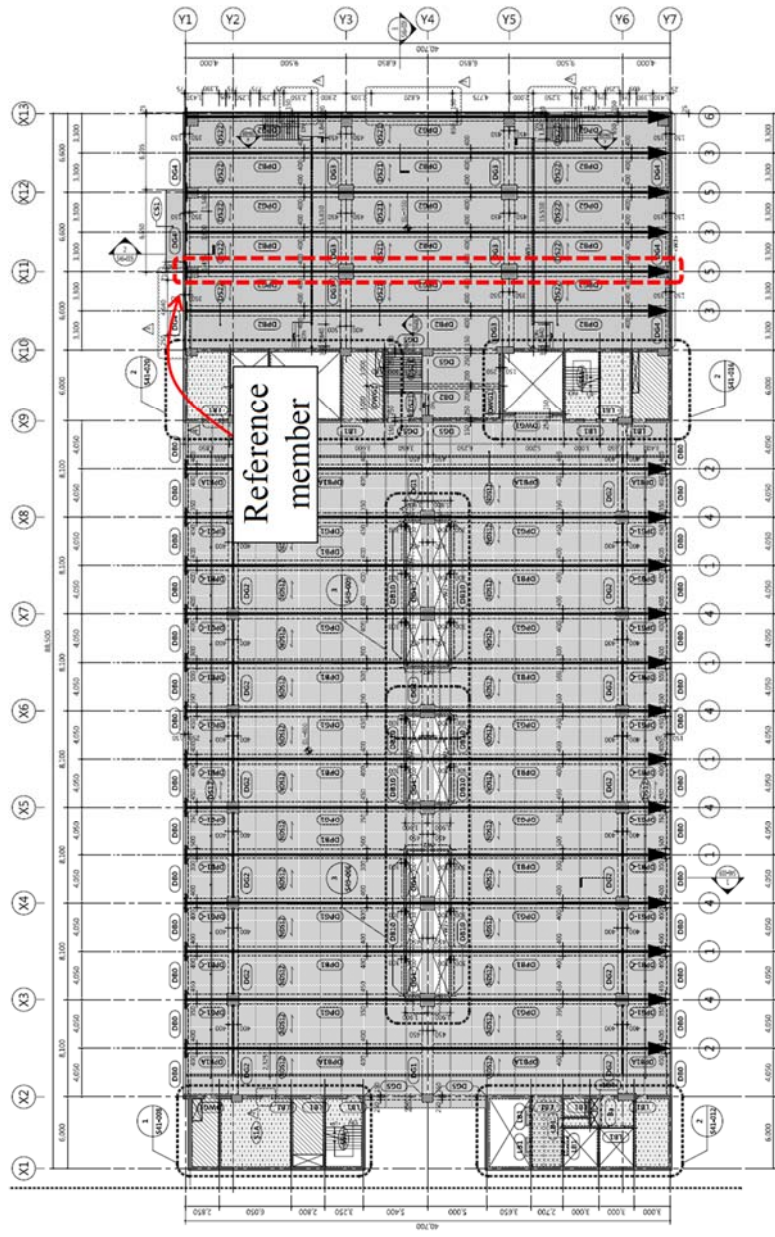
## **Chapter 3. Specimens Program**

In this chapter, design process and fabrication process of seven specimens are presented. The specimens were designed based on the existing building (NH IT Center, constructed in 2015) design and the size was reduced down to half due to the limitations of the experimental environment. The half scale specimen design was checked against ACI 318-14 and PTI M50.2-00: Anchorage Zone Design. Three variables were considered in this study: strand type, prestressing force, and tendon profile height.

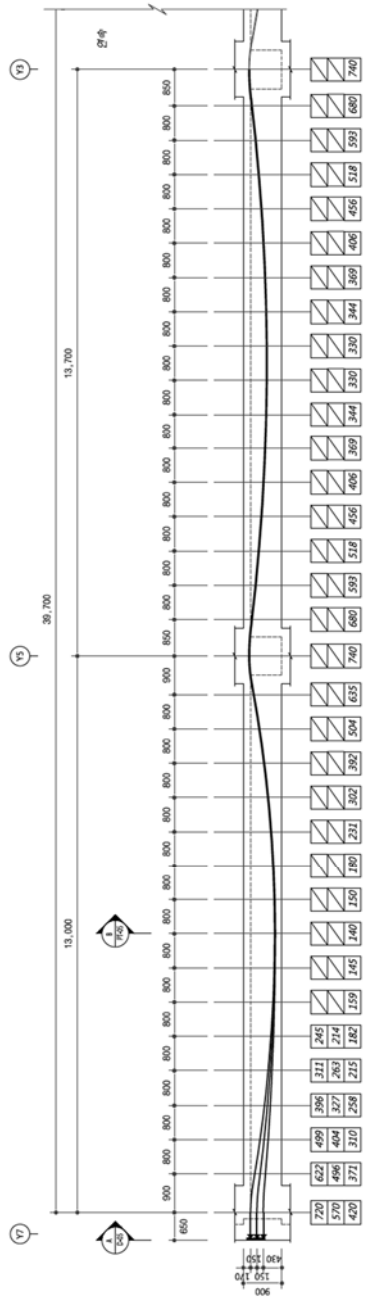
### **3.1 Specimen dimension**

#### **3.1.1 Span**

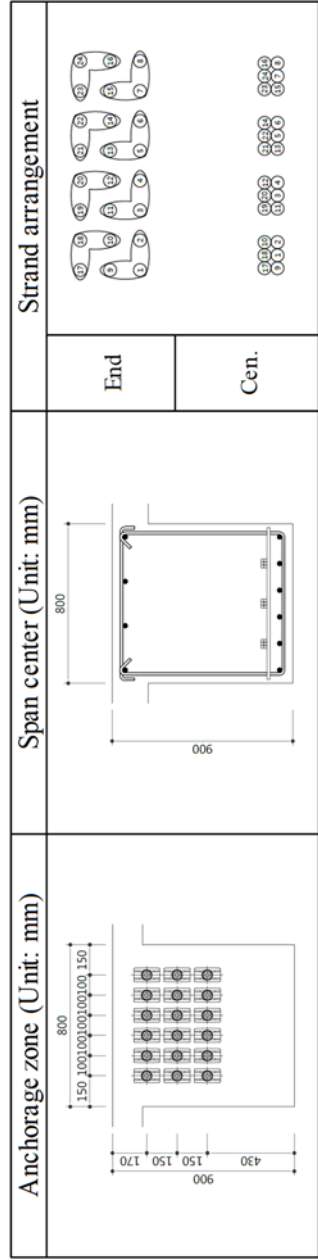
The seven specimens were designed based on the continuous post-tensioned beams used in an existing building. The referenced continuous beam is presented in **Figure 3-1**. Originally, the referenced member was a 3-span continuous post-tensioned girder having a total length of 39.7 m. To achieve the experimental goals effectively in the limited experimental environment, the number of spans was reduced down to two, where investigation of the unique features of continuous PT beams prestressed with unbonded tendons needs to be demonstrated: the effect due to indeterminacy such as secondary moment, impact of multiple hinge development on tendon stress variation, moment redistribution, influence of tendon profile shape, and other incidental or possible phenomena that may not be discovered in a simple beam test. The length of each span was determined to be 6.85 m for every specimen which was taken from the middle span length as a reference.



(a) Floor plan view of reference design



(b) Elevation section view (Unit: mm)



(c) Section detail

Figure 3-1 Reference design of 2-span PT beam (NH IT Center, Constructed in 2015)

### 3.1.2 Section

Sections of each specimen were determined based on the reference design in the same manner of how the span length was decided. The section size was reduced to half in size ended up having a rectangular section with 450 mm of depth and 400 mm of width, which is a quarter of the original sectional area. Since the reference beam was designed to have 16 unbonded, Grade 270, 15.2 mm diameter prestressing strands ( $A_{ps} = 140 \text{ mm}^2$ ,  $f_{pu} = 1860 \text{ MPa}$ ), the representative number of the tendons of the reference beam was decided to be four of the same kind of strand. This is because the original sectional area was reduced to a quarter, so did the area of prestressed reinforcement ( $A_{ps}$ ). For comparison, the representative number of 2400 MPa strands was determined to be three, with the same strand section area of  $140 \text{ mm}^2$ , but the higher strength of 2400 MPa. Assuming that the same percentage of jacking forces were to be applied regardless of the strand type ( $0.75f_{pu}$ ), almost equivalent amount of effective prestressing force was applied with three very high-strength strands compared to the prestressing force with four ordinary high-strength strands.

### 3.2 Member design

The specimens were designed assuming a uniformly distributed loading throughout the length. The design was carried out to ensure adequate ductility to achieve realistic beam design and enough behavioral ranges. Every specimen had identical bonded reinforcement meeting the minimum requirement for bonded reinforcement in ACI 318-14, Section 9.6.2.3. To meet the serviceability requirement in ACI 318-14, Section 24.5.2.1, concrete

stresses were checked as described in Section 2.2.1 and additional compression steel reinforcement was provided identically to each of the specimens to meet the requirements. In terms of nominal flexural strength at the critical sections, specimens in each comparing group were designed to have almost same flexural strengths according to ACI 318-14 code. This is to compare the theoretical and experimental flexural strengths of the specimens with the ordinary high-strength strands and the very high-strength strands individually. In this respect, shear reinforcement was provided rather conservatively to every specimen. Flexural failure was designed to be a controlling failure mode of the specimens. Further information about the specimen design is provided in **Table 3-1**, **Figure 3-2**, and Appendix A.

**Table 3-1** Test specimen details

Specimen	B4H	B4L	B5L	D3H	D3L	D4H	D4L
Strand type (MPa)	1860	1860	1860	2400	2400	2400	2400
Number of strand	4	4	5	3	3	4	4
Profile height (mm)	354	176	176	354	176	354	176
$f_{se}$ (MPa)	1148.7	1150.6	1150.6	1502.4	1503.9	1502.4	1503.9
$f'_c$ (MPa)	52.7	52.7	52.7	52.7	52.7	52.7	52.7
$f_y$ (MPa)	478.2	478.2	478.2	478.2	478.2	478.2	478.2
$A_s$ (mm <sup>2</sup> )	799.4	799.4	799.4	799.4	799.4	799.4	799.4
$A_{ps}$ (mm <sup>2</sup> )	277.4	554.8	693.5	416.1	416.1	554.8	554.8
$\rho$ (%)	0.22	0.44	0.44	0.44	0.44	0.44	0.44
$\rho_p$ (%)	0.35	0.44	0.55	0.26	0.33	0.35	0.44
$b$ (mm)	400	400	400	400	400	400	400
$d$ (mm)	450	450	450	450	450	450	450
$l$ (m)	6.85	6.85	6.85	6.85	6.85	6.85	6.85
$d_s$ (mm)	402	402	402	402	402	402	402
$d_p$ (mm)	402	313	313	402	313	402	313

$f_{se}$ : effective stress in prestressing reinforcement, after allowance for all prestress losses;  $f'_c$ : specified compressive strength of concrete;  $f_y$ : specified yield strength for nonprestressed reinforcement;  $A_s$ : area of nonprestressed longitudinal tension reinforcement;  $A_{ps}$ : area of prestressed longitudinal tension reinforcement;  $\rho$ : ratio of  $A_s$  to  $bd$ ;  $\rho_p$ : ratio of  $A_{ps}$  to  $bd_p$ ;  $b$ : section width;  $d$ : section depth;  $l$ : span net length;  $d_s$ : distance from extreme compression fiber to centroid of longitudinal tension reinforcement; and  $d_p$ : distance from extreme compression fiber to centroid of prestressing reinforcement.



### 3.3 Anchorage zone design

The concept and process of conducting anchorage zone design are presented in Section 2.2.4. As mentioned in Section 2.2, flexural failure of the member was determined to be the controlling failure mode of every specimen. Not only shear failure was acceptable, failure of the anchorage zone was also avoided. Thus, enough amount of reinforcement was provided for the anchorage zone. Back-up bars were fully provided to the rear portion of every anchor plates, and the cross ties and 135-degree hooks were concentrated inside and near the local zones to resist bursting force. In this case, cross ties are considered as hairpin bars. The confinement effect of the 135-degree hooks could contribute to the greater resistance against the bursting force. In this manner, the reinforcement design in the anchorage zone was conducted in a very conservative way. This is because the tendon stress could reach up to its specified tensile strength. **Figure 3-3** shows the detail of anchorage zone reinforcement (Specimen D3H).

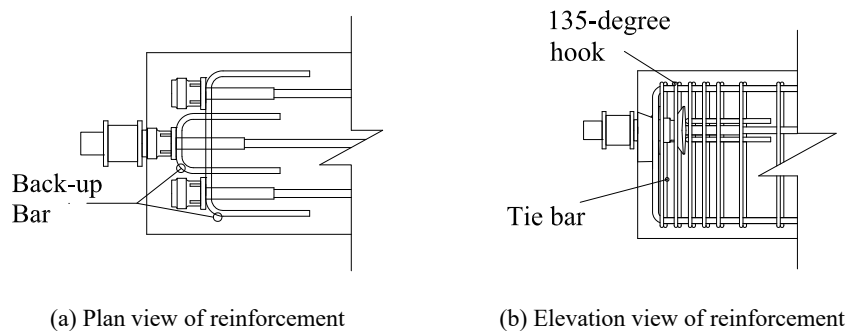
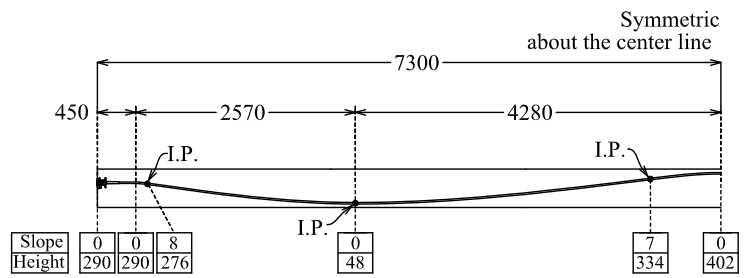


**Figure 3-3** Anchorage zone design (Specimen D3H)

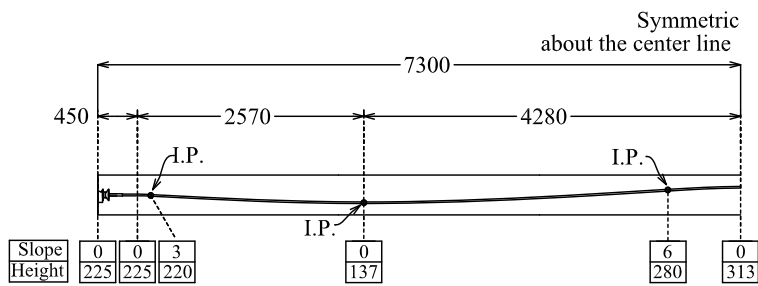
### 3.4 Tendon profile design

Tendon profile consisted of several parabolas throughout the beams, and there

were two types of tendon profile that were used for the specimens: high profile and low profile. As shown in **Figure 3-4**, the high profile had a total height of 354 mm while the low profile had a height of 176 mm which was a half of the high profile in height. Anchorage location of the high tendon profile was elevated 65 mm from the section center to secure greater curvatures whereas those of low tendon profile was located at the section center. The lowest point of the tendon profiles was located 200 mm inside of the exterior loading points. The lowest point of the tendon was designed to correspond to the location where the maximum positive moment occurs when the uniformly distributed load is applied throughout the length. This location is where the deflections were measured with LVDTs. For detailed information about test setup, see Section 4.4 The highest and lowest points of each tendon profile had the same eccentricity with respect to the c.g.c. of the section. **Figure 3-4** shows the detailed elevation of each tendon profile shape.



(a) Elevation view of high tendon profile



(b) Elevation view of low tendon profile

**Figure 3-4** Tendon profile shape (I.P: inflection point; Unit: mm)

### 3.5 Discussion

In this chapter, the detailed design process of specimens was introduced. Primary considerations are as follows:

- 1) All seven specimens were designed as half scale and satisfied the design specification of ACI 318-14, PTI M50.2-00: Anchorage Zone Design. Three variables were considered, which are strand type, prestressing force, and tendon profile height.
- 2) Every specimen was designed as symmetrically about the interior support location, and the same shear reinforcement and flexural reinforcement details were provided to every specimen. Shear reinforcement was conservatively provided so that flexural failure can be the controlling failure mode. In the same sense, enough amount of reinforcement was provided for the anchorage zone design.
- 3) Two kinds of tendon profiles were: high and low profiles. The lowest point and the highest point of each tendon profile passed the critical section having the same distance between the tendon center to the extreme tension fiber of concrete. Thus the maximum positive moment sections on the both spans have upside down section of the maximum negative moment section at the interior support location.

## **Chapter 4. Construction, Test Setup and Testing**

### **4.1 Specimen construction**

All specimens were constructed in a precast factory in Yeosu, Korea. The specimens were constructed in the process where the three specimens with ordinary high-strength strands were constructed first and the other four specimens with very high-strength strands were built later having a week gap between.

To begin with, the reinforcing bars were fabricated on the top of wooden forms. Then tendons were placed throughout the length. At this point, fixed end of the tendon is anchored with an anchorage. In the procedure of placing tendons, some tendons were bundled like as in the real construction site. The tendons were fixed onto the tie bars to make the parabola shapes described in the design. After the tendons were all placed and the profile shapes were made, jacking ends of the tendons were put together with the formwork panels by assembling the pocket formers and the anchorages. And then steel gauges were installed and the formwork panels on the sides were put together.

After concrete casting, the specimens were steam cured for a day and laid for 50 days before jacking. The strands were jacked one by one with a hydraulic single-strand jack. Note that the locations of jacking and fixed ends for some tendons were switched between both ends in an attempt to make the specimens as symmetric as possible about the interior support location of the member. During jacking procedure, the prestressing force was measured at the load cells employed between the steel chuck and the anchorage. After jacking, the specimens were delivered to a structural testing facility in Incheon, Korea.

**Figure 4-1** displays the construction process and **Figure 4-2** shows steel reinforcement.



(a) Placing tendons



(b) Tendon profile shaping



(c) Steel gauge installment



(d) Concrete pouring



(e) Steam curing



(f) Removing formwork



(g) Jacking strands



(h) Completion

**Figure 4-1** Manufacturing process



(a) Anchorage zone detail (high profile)



(b) Anchorage zone detail (low profile)



(c) Anchorage zone view (D3H)



(d) Transverse rebar at 100 mm spacing



(e) Tendon profile at the highest point (high profile)



(f) Tendon profile at the lowest point (high profile)



(g) Tendon profile at the highest point (low profile)



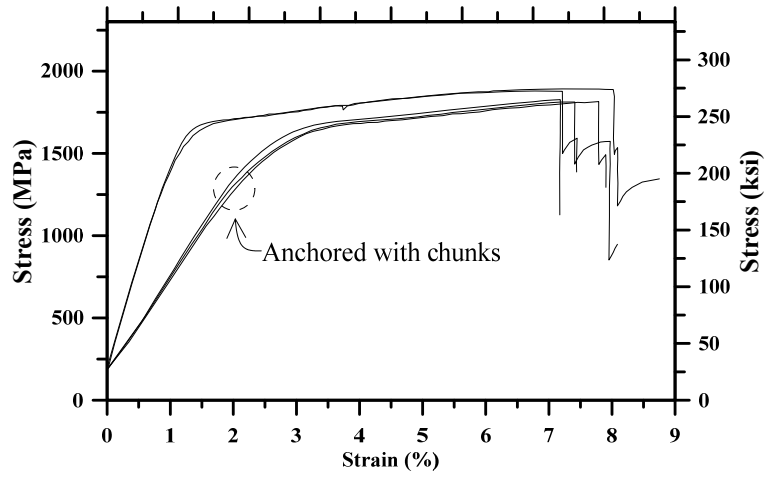
(h) Tendon profile at the lowest point (low profile)

**Figure 4-2** Steel reinforcement detail

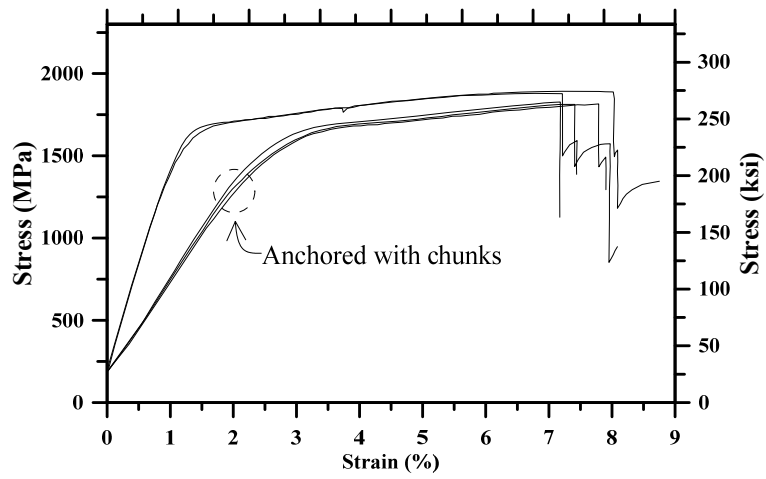
## 4.2 Material property and anchorage components

### 4.2.1 Strand

For fabrication of the specimens, two types of strands were used: SWPC 7B, and SWPC 7DL. See **Table 2-2**. Korean standard (KS D 7002) specifies several requirements of the very high-strength strands. In an attempt to investigate the behavior of the very high-strength strands in prestressed members (particularly the correlation between the local hinge development mechanism and the tendon stress increase trend) material tests were carried out for the samples of both ordinary and very high-strength strand and high-strength strands that were used for the fabrication by Korea Testing & Research Institute (KRT). **Figure 4-3** shows stress-strain curves of high-strength and very high-strength strand samples. All the samples showed their nominal strength and fractured at around 7% strain except for one 2400 MPa strand sample. The samples were tested in two ways. Some samples were tested with steel chucks anchored at the ends and pulled. Other samples were tested directly without the chucks.



(a) Ordinary high-strength strand



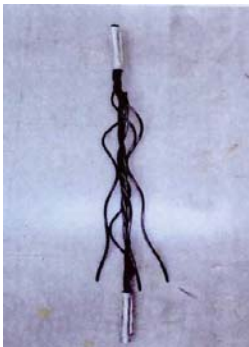
(b) Very high-strength strand

**Figure 4-3** Stress-strain curves of strand samples

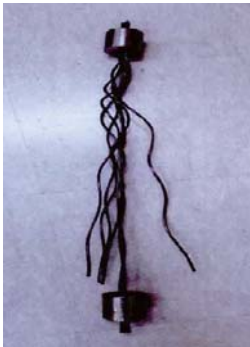
**Figure 4-4** shows the configuration. Stress-strain curves indicated in **Figure 4-3** displays that the samples tested with the chuck anchors showed less elastic modulus than the samples without the chucks. This is considered to be due to the locking behavior between the chucks, strands, and wedges inside the chucks and this made some slips. Detailed discussion on the material property of the 2400 MPa strand and the 1860 MPa strand is provided in another Section 7.2



(a) 1860 MPa strand sample with steel chucks



(b) 1860 MPa strand sample with steel chucks



(c) 2400 MPa strand sample with steel chucks



(d) 2400 MPa strand sample with steel chucks

**Figure 4-4** Failure of strand samples

### 4.2.2 Concrete and steel

Cast-in-place concrete with a nominal strength of 50 MPa was used in fabrication. **Table 4-1** shows 100 mm diameter cylinder compression testing at three different test ages of concrete cylinders: 28 days, 50 days (jacking), and 66~70 days (experiment). The cylinders were cured next to the specimens and the average testing results from cylinder compression testing at each age were 47.0 MPa, 51.9 MPa, and 52.3 MPa, respectively. Concrete mixing and placing were done by a mixer truck, as in actual in-site construction. The pictures of concrete cylinders and testing are shown in **Figure 4-5**.

**Table 4-1** Concrete cylinder test results

Age (days)	Batch	Sample strength (MPa)				Mean strength (MPa)	W/B (%)	$E_c$ (MPa)
28	1	49.3	44.7	44.45	46.2	47.0	29.5	34,352.4
	2	49.2	44.7	49.9	47.9			
40 (Jacking)	1	48.1	51.0	49.8	49.6	51.9		
	2	54.9	54.6	53.2	54.2			
66~70 (Testing)	1	49.6	46.3	50.8	48.9	52.2		
	2	51.1	48.9	61.2	61.2			

$E_c$ : modulus of elasticity concrete



(a) Concrete cylinder



(b) Curing



(c) Concrete cylinder test



(d) Concrete cylinder test

**Figure 4-5** Concrete cylinder and test

Three types of reinforcing steel were used in the fabrication and the test results of the steel samples are presented in **Table 4-2**. Reinforcing bars with a nominal strength of 400 MPa were used for nonprestressed reinforcement. The stress-strain curves are presented in **Figure 4-6** and the photo of steel sample test is shown in **Figure 4-7**.

**Table 4-2** Steel test results

Steel	$f_y$ (MPa)	$f_u$ (MPa)	$f_u/f_y$
D10	524.1	663.7	1.27
	526.3	657.4	1.25
	527.2	638.4	1.21
Mean	525.9	653.2	1.24
D13	494.2	610.1	1.23
	480.4	594.1	1.24
	491.9	605.4	1.23
Mean	488.8	603.2	1.23
D16	485.4	596.2	1.23
	475.8	584.3	1.23
	486.9	599.6	1.23
Mean	482.7	593.4	1.23

$f_y$ : specified yield strength for nonprestressed reinforcement; and  $f_u$ : specified tensile strength of nonprestressed reinforcement

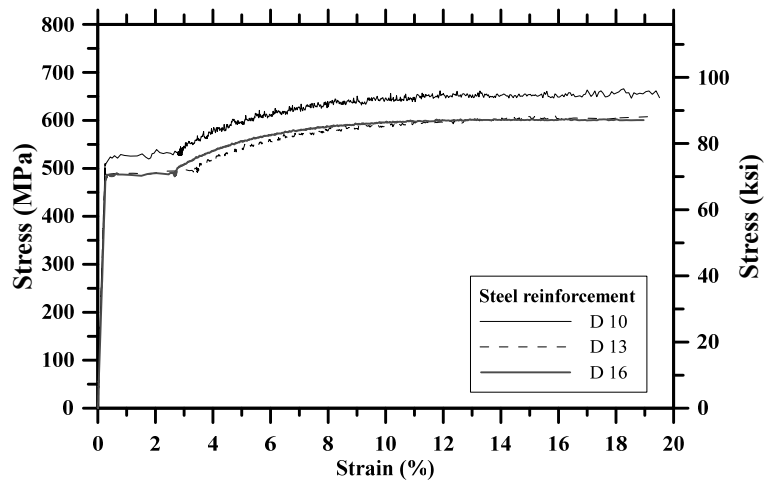


**Figure 4-6** Stress-strain curves of mild steel



(a) Polishing the surface of re-bars to attach gauges



(b) Steel sample failure

**Figure 4-7** Mild steel sample test

### 4.2.3 Anchorage components

In the fabrication, two different types of anchorages were used due to the difference in strand type. For 1860 MPa strands, plastic encapsulated anchorages (KFA; Korea's First Anchor) were used. For 2400 MPa strands, mono-strand anchorages produced by a PT supplier were used. **Figure 4-8** shows the photos anchorages assembled with wedges and strands.



(a) Anchorage for 1860 MPa (KFA)



(b) Anchorage for 2400 MPa

**Figure 4-8** Prestressing steel sample test

### 4.3 Test setup and measurement

#### 4.3.1 Test setup

The test instrumentation is presented in **Figure 4-9**. The specimens were put on three round-cylindrical supports. The photo of the supports is shown in **Figure 4-10(a)**. Two hydraulic actuators were used to apply static loads individually on both spans at the same rate of displacement control at the speed of 1 mm/min. Two spreader beams were attached at the end of each actuator connected with rotatable hinges. This jig enabled the force equally divided from the actuator and transferred equally to both ends of the spreader beam, mimicking a uniformly distributed load. See **Figure 4-10(b)** and **(c)**.

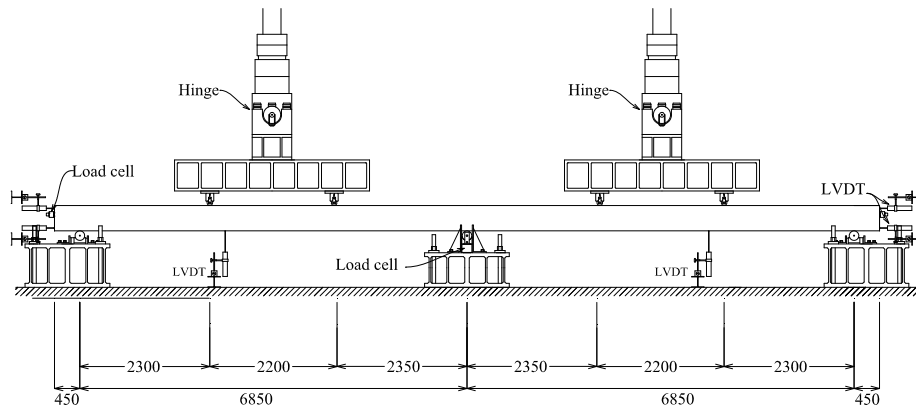


**Figure 4-9** Two-span beam test (Unit: mm)

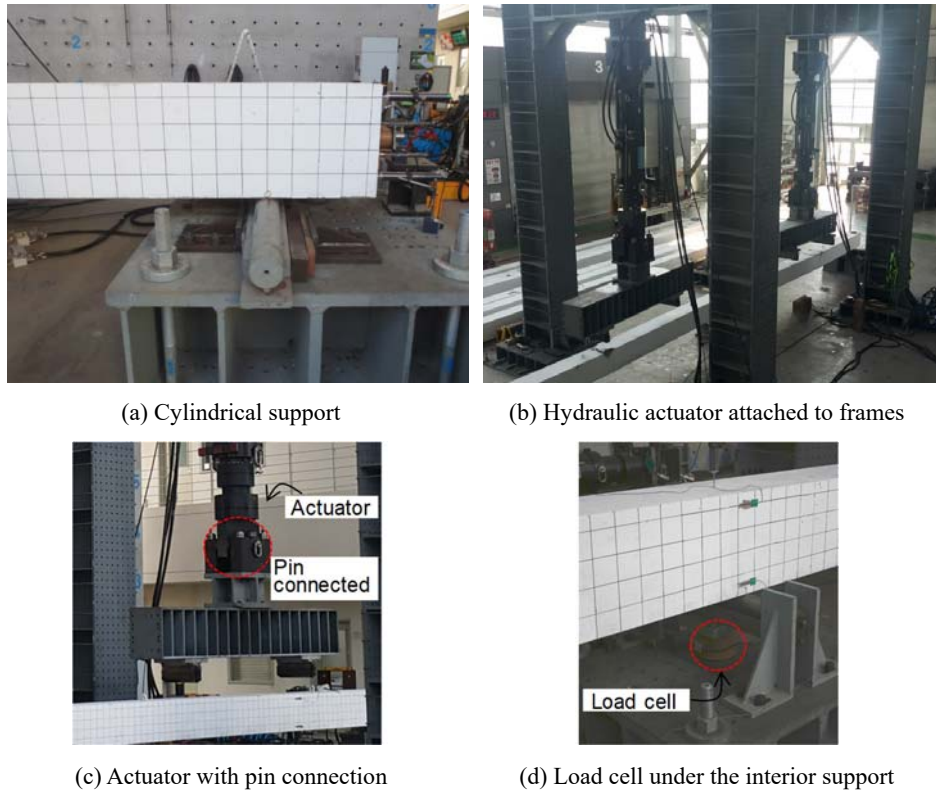


**Figure 4-10** Test setup

### 4.3.2 Measurement plan

Prestressing force was measured from jacking stage throughout the entire loading testing. A representative tendon for each specimen was chosen for every specimen to measure the tendon force. Jacking ends and fixed ends of Specimens B4H, B4L, B5L, and D3H employed hollow-core load cells between the chuck and anchorage to measure the prestressing force. In Specimens D3L, D4H, and D4L, load cells were used only on the jacking ends. Detailed plan for measuring prestress is shown in **Figure 4-11**.

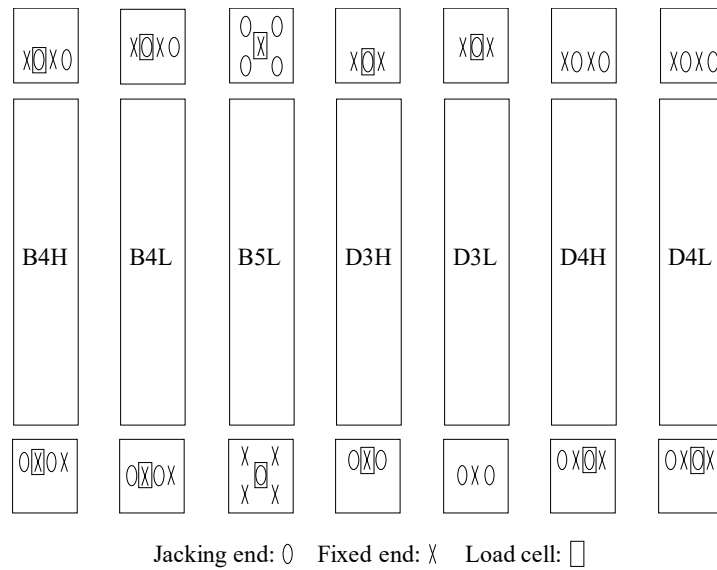


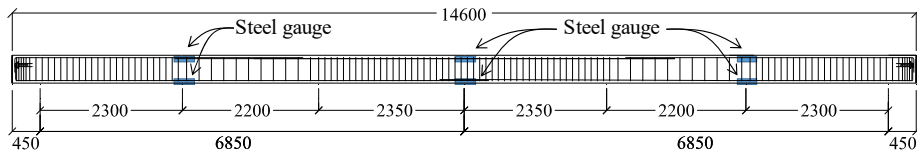
**Figure 4-11** Strain gauge locations

Each actuator had an in-built load cell which measured the applied load. Other than the load cells in the actuators, an additional 200-ton-capacity load cell was employed under the interior support. This load cell provided the reaction force at the interior support, so the moment redistribution and secondary moment can be computed. LVDTs were installed on both spans to measure vertical deflections at the locations where the maximum deflection is expected. At both end side surfaces, LVDTs were employed on the top and bottom part to measure the parallel displacement by which end rotations were able to be measured during load testing. The LVDTs are illustrated in **Figure 4-9**.

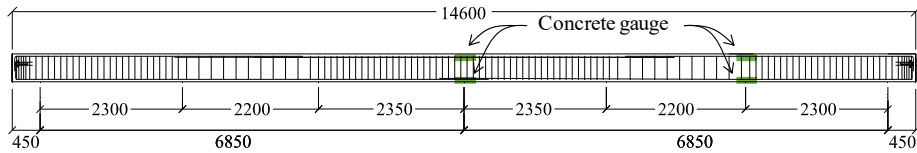
### 4.3.3 Strain gauge plan

Electrical strain gauges were applied to the reinforcing steel and concrete surface. Steel gauges were mounted on the top and bottom longitudinal re-bars at each critical section where the tendon profile is at its highest or lowest point. Concrete strain gauges were attached at the same elevation level of the

steel gauges, but only at two critical sections. **Figure 4-12** displays the location of the steel and concrete gauges.



(a) Steel gauge locations



(b) Concrete gauge locations

**Figure 4-12** Strain gauge locations (Unit: mm)

## 4.4 Discussion

In this chapter, construction of specimens, material properties, and test setup were illustrated. Primary considerations are summarized as follows.

- 1) All specimens were constructed in a precast factory in Yeosu, Korea and delivered to the testing facility in Incheon, Korea. In the construction, 50 MPa concrete was used and two different types of strands were used 1860 MPa and 2400 MPa strength. Reinforcing bars of SD 400 were used for the fabrication.
- 2) After concrete casting, the specimens were steam cured for a day and laid for 50 days before jacking. Prestressing force was measured during the jacking and after the jacking, the specimens were delivered by trucks.
- 3) The load was applied with two actuators which had load cells within it

individually. Each actuator was pin-connected to a spreader beam so that the jib enabled the force equally divided mimicking a uniformly distributed load.

- 4) There was a load cell of 200-ton-capacity to measure the reaction at the interior support. The data provided by this load cell reduced one degree of indeterminacy of the structure and enabled the full static analysis. Prestressing force, strain gauge data, deflection, and end rotation were kept measured during the loading test.

## Chapter 5. Monitoring Prestress Loss

### 5.1 Immediate elastic losses

During the construction of post-tensioned concrete members, immediate prestress losses can occur during or right after jacking. The immediate prestress losses include the losses associated elastic shortening of concrete, anchorage slip, and friction.

#### 5.1.1 Elastic shortening

In post-tensioned members, the surrounding concrete is being compressed while the tendon is stressed and elongated. This does not affect the stress of the tendon being elongated at the time, but does affect the prestress of the other tendons that are already jacked. The elastic shortening loss in a post-tensioned member depends on the sequence of stressing operations and the average of the losses of the individual tendons can be taken as the elastic shortening loss. **Table 5-1** shows the measured prestress loss generated by elastic shortening in the firstly jacked tendon of each member at jacking ends. The data does not show clear trend but the firstly jacked tendon in Specimen B4H showed unexpectedly low prestress loss due to elastic shortening. This provides a credibility to the hypothesis that some of the tendons in Specimen B4H were not jacked correctly.

**Table 5-1** Measured prestress loss due to elastic shortening from the firstly jacked tendons

Specimen	B4H	B4L	B5L	D3H	D3L	D4H	D4L
Prestress loss (MPa)	11.3	27.5	35.3	50.0	22.9	28.2	33.5

### 5.1.2 Anchorage slip

Once the stress at the jacking end reached its prescribed value, the strand was released and was locked into a conical wedge cavity in the anchor, retracting and drawing the wedges. In the process, stress loss was observed. A sudden stress drop at the jacking end was noted which was produced by this anchor set (anchorage slip) loss. This loss is represented as “Loss (1)” in **Figure 5-1**.

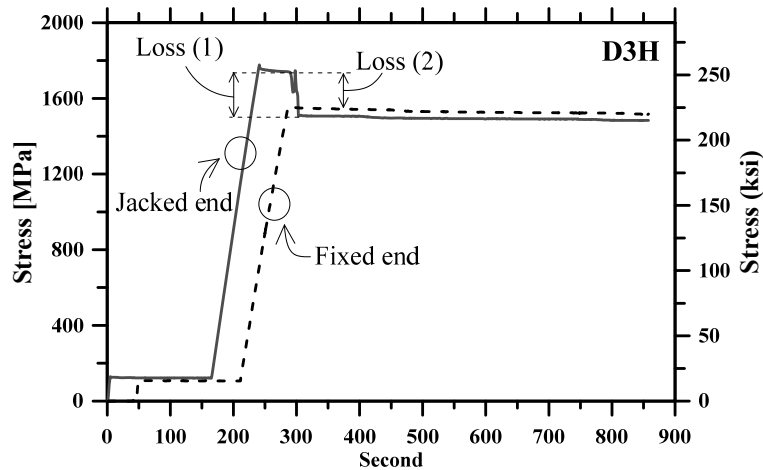


**Figure 5-1** Stress variation during jacking and anchor slip (D3H)

**Figure 5-1** shows measured stress variations of the tendon at the jacking end and fixed end in Specimen D3H during jacking. The discrepancy presented as “Loss (2)” in the figure indicates the total friction loss occurred between the jacking end and fixed end. The total friction loss consists of curvature friction and wobble friction. Other measured data of stress variation during jacking are provided in Appendix B. The ratio of  $T_0$  to  $T_{14.6}$  can be calculated and this allowed to estimate  $\mu$  and  $\kappa$ .  $T_x$  is the prestressing force at point  $x$ ,  $\mu$  is the curvature friction coefficient, and  $\kappa$  is the wobble friction coefficient. The detailed procedure is presented in the following section.

### 5.1.3 Friction losses

During prestressing, the prestressing force along the tendon decreased from its maximum value at the jacking end to minimum at the fixed end. This decrease was due to friction losses between the prestressing strand and its sheathing or duct due to the intended tendon curvature and unintended tendon curvature, which is also called wobble (ACI 423.10R-16). These losses can be estimated by using the following equation (ACI 423.10R-16).

$$T_x = T_0 e^{-(\mu\alpha + \kappa x)} \quad \text{Eq. (5-1)}$$

where,  $x$  is the length of tendon from stressing end to point  $x$ ;  $T_x$  is the prestressing force at point  $x$ ;  $\mu$  is the curvature friction coefficient,  $\kappa$  is the wobble friction coefficient; and  $\alpha$  is the total angular change in radians from jacking end to point  $x$ .

To investigate these effects caused by friction losses, the measured values of the prestressing forces during jacking were categorized and analyzed to determine curvature friction coefficient ( $\mu$ ) and wobble friction coefficient ( $\kappa$ ). Four specimens (B4H, B4L, B5L, and D3H) had the measured values at the jacking and fixed ends; however, the measurement from Specimen B5L was not reliable because several additional jacking steps were attempted due to some technical issues of the mono-strand jack. With the three given ratios of ( $T_0/T_{14.6}$ ) from Specimens B4H, B4L and D3H, the average value of ( $\mu\alpha + 14.6\kappa$ ) was evaluated. Consequently,  $\mu$  and  $\kappa$  were determined as 0.044 and 0.0044 m<sup>-1</sup> respectively. The  $\mu$  fell into a range specified in performance specification (PTI M10.3-00). However,  $\kappa$  is rather beyond the code range. The reason is considered to be because the measured tendons were the specially manufactured tendons with fiber optic sensors for the measurement

purpose by inserting the tendon into the plastic tube. See **Table 5-2** for detailed data.

**Table 5-2** Prestress measured from load cells at different stages

Specimen	$f_{j_j}$ (MPa)	$f_{j_f}$ (MPa)	$f_{a_j}$ (MPa)	$f_{se_j}$ (MPa)	$f_{se_f}$ (MPa)	$f_{ps_j}$ (MPa)	$\Delta f_{ps_j}$ (MPa)	$\ln(\frac{f_{j_f}}{f_{j_j}})$
B4H	1375	1239	1199	1121	1140	1663	542	0.10386
B4L	1391	1276.3	1221	1129	1157	1589	460	0.08634
B5L	1432	1214	1190	1096	1127	1479	383	0.16513
D3H	1743	1549	1506	1420	1446	2121	701	0.11815
D3L	1785	-	1596	1524	-	2054	529	-
D4H	1752	-	1586	1464	-	2059	595	-
D4L	1738	-	1603	1488	-	1953	464	-

$f_{j_j}$ : measured prestress at jacking stage at the jacking end;  $f_{j_f}$ : measured prestress at jacking stage at the fixed end;  $f_{a_j}$ : measured prestress right after anchor set at the jacking end;  $f_{se_j}$ : measured prestress at effective prestress stage at the jacking end;  $f_{se_f}$ : measured prestress at effective stage at the fixed end;  $f_{ps_j}$ : measured prestress at the peak load at the jacking end; and  $\Delta f_{ps_j}$ : measured prestress increment between effective stage and nominal stage at the jacking end.

Note that the prestress at the fixed end remained almost constant between jacking stage and after anchor set behavior. This is due to enough length of the specimens so that anchor set loss could not affect the prestress throughout the full length. By using the obtained  $\mu$  and  $\kappa$ , stress variation profiles according to each strand type and tendon profile were derived as shown in **Figure 5-2**. In the process, several assumptions were made: 1) rate of angular change of a tendon profile is constant throughout the tendon profiles regardless of the location; 2) curvature friction coefficient is a constant value regardless of strand type; and 3) wobble friction coefficient is the same value in every case. Because of the first assumption, the prestress drop due to anchor set can be reflected in the tendon stress profile in a manner that the stress dropped with the inverse direction demonstrating the same slope, but in opposite sign.

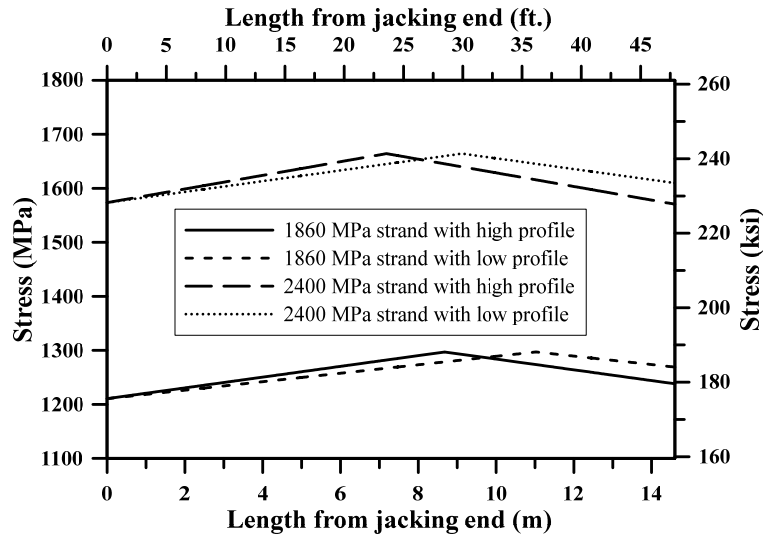


Figure 5-2 Prestress variation profile

## 5.2 Time dependent losses

Time dependent losses occur due to the behavior of concrete and prestressing steel through the lifespan of the member. The time dependent prestress losses are considered long-term losses, and analyzing this effect is highly complicated because the effect of prestressing steel such as relaxation affects concrete behavior and they interact with each other in a complicated manner. Code specifications (ACI 318-14; CEN, 2004; Standard, NZS 3101, 2006.) identify the causes for long term loss as concrete creep, dry shrinkage, and relaxation of prestressing steel. The loss can be computed by considering the individual factors of concrete shrinkage and creep, and tendon relaxation and simply adding up those effects to estimate the total long term loss. In this study, the detailed approach of estimating long-term loss is beyond the scope of the study. It showed the total long-term prestress loss of 88.8 MPa from the specimens with ordinary high-strength strands and 98.6 MPa from the

specimens with very high-strength strands, respectively, for the duration of jacking to the commencement of loading test days. Given the equivalent prestressing force applied to the same mass of concrete member in longitudinal direction, the strands with 1860 MPa strength showed less long-term prestress loss. This implies that the strain range in the long-term loss of the 1860 MPa strands included more distinct strain hardening zone in the material respect. One interesting thing observed during the long-term loss is that the prestress measured at the jacking end and the fixed end in each specimen showed almost same decrease amount of prestress. This observation revealed that the prestress of the tendons throughout the length experienced about the same amount of prestress loss.

### **5.3 Discussion**

In this chapter, prestress loss between the jacking and loading test was monitored and discussed. The main summaries are as follows.

- 1) The prestress loss was monitored from the specimens in the respect of immediate elastic losses and time dependent losses.
- 2) Prestress variation at the jacking end and fixed end were measured during jacking and seating. It was noted that the prestress at the jacking end experienced the immediate prestress loss due to anchor set behavior and elastic shortening of the concrete. The fixed ends were not affected by the anchor set behavior because of the enough distance between those two points.
- 3) Based on the discrepancy measured between the jacking end and the fixed end at the moment when the mono-strand jack held the strand,

friction between the jacking and fixed ends was evaluated and friction coefficients ( $\mu$  and  $\kappa$ ) were derived.

- 4) Time dependent loss due to concrete creep, drying shrinkage, and relaxation of prestressing steel was measured to be 88.8 MPa in the specimens with 1860 MPa strands, and 98.6 MPa in the specimens with 2400 MPa strands prior to testing.
- 5) During the prestress loss, the loss measured both at the jacking and fixed ends showed almost the same trend of variation. This revealed that the prestress of the tendons throughout the length experienced about the same amount of prestress loss.

# Chapter 6. Loading Test Result and Analysis

## 6.1 Prestress variation

### 6.1.1 Prestress during loading test

A tendon for each specimen was chosen to measure prestress from jacking stage to failure state of the specimen. Four specimens of B4H, B4L, B5L, and D3H employed two load cells at the both ends of a tendon and the rest of three specimens of D3L, D4H, and D4L had only one load cell for each representative tendon at the jacking end to measure the prestress variation. Prestress variation until the onset of the loading test is described in Chapter 5. In this chapter, prestress variation observed from every specimen during loading is described and discussed. **Figure 6-1** shows the measured prestress variation of the specimen D3H at the jacking and fixed ends according to the deflection.

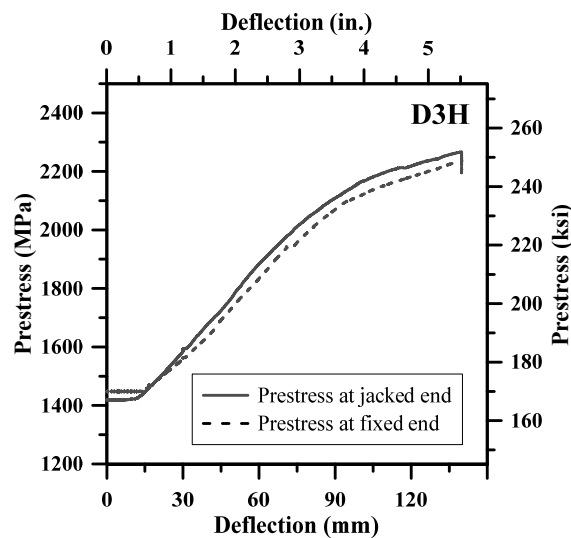


Figure 6-1 Prestress variation during loading test (D3H)

From the measured data, the followings were revealed.

- (1) The prestress increase rate was remained almost zero while the members were in elastic behavior state. As the members started to develop the first hinge at the interior support location, the prestress increased. This indicates that the prestress variation is closely related to the development of hinges and plastic collapse mechanism.
- (2) The prestress increase rate reduced as the prestress approached the nominal strength of the prestressing steel. This is considered to be due to the nonlinearity of the prestressing steel.
- (3) From the measured data at the jacking and fixed ends, it was discovered that the prestress variation trends between the jacked and fixed ends were similar in the same specimen. This corresponds to the fact that the long-term prestress loss happened in the same manner at the both ends.
- (4) From the discussion derived in (3) above, it is possible to assume that the tendon prestress profiles throughout the length were maintained after the anchor set loss.

### **6.1.2 Prestress in member**

From the discussion derived in (4) above, the prestress profile throughout the length of each specimen can be derived. Note that the inverted V-shaped prestress profiles presented in **Figure 5-1** show the prestress profile in the tendon level. Since the location of jacked and fixed ends were switched between the east and west ends (i.e., alternated stressing anchorage), the average prestress profile of the Specimen D3H in **Figure 6-2** looks more like a symmetric V-shape. In this case, the prestress in the interior support location

was larger than the other two critical sections where the maximum positive moment occurred. This indicates that the hinge at the interior support location might have larger plastic hinge moment resistance than other two critical sections even though their section geometry for applied moment direction were exactly the same. Derived prestress profiles from other specimens are provided in Appendix C.

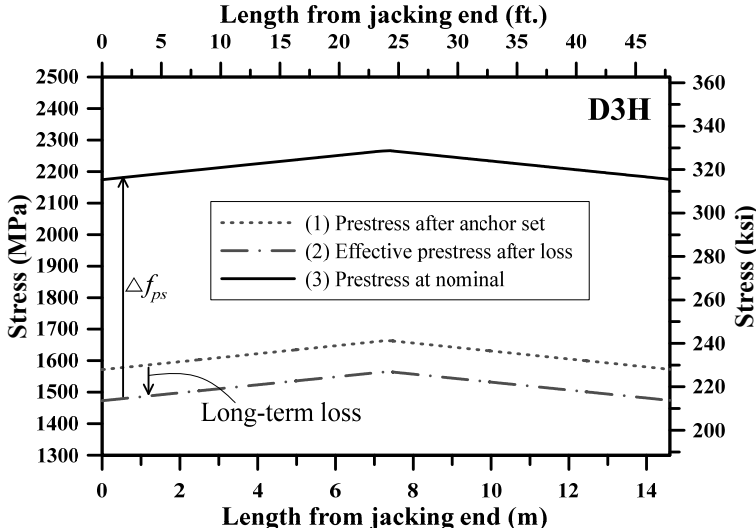


Figure 6-2 Member prestress distribution profile at different stages (D3H)

### 6.1.3 Prestress at nominal flexural strength ( $f_{ps}$ )

In this study,  $f_{ps}$  was evaluated in the view of member level rather than solely relying on the section geometry, and it was defined as the average stress of the prestressing reinforcement of the member at the peak load. This allowed to consider the effect of the member continuity to  $f_{ps}$  and better reflects the prestress variation at the ultimate state in real structures. The average prestress can be evaluated by integrating the area underneath the prestress profile at nominal (see **Figure 6-2**) divided by the total member length. Since the value is based on the experimental result, this is denoted as  $f_{ps\_exp}$  in this study. There

have been numerous equations for predicting this value. Methodologies by ACI 318-14, AASHTO (2017), Naaman et al. (2002), and Harajli (2006) were used to predict  $f_{ps}$  of the specimens and compared in **Table 6-1**. The results of the negative moment at an interior support using the method of Harajli (2006) are given in the brackets. It was discovered that the methodology suggested by Naaman et al. (2002) showed the most accurate prediction and the ACI equation quite underestimated the actual  $f_{ps}$  from the test result. From the discoveries made from the test results, the following trend could be found which corresponds to the past studies conducted by many researchers.  $\Delta f_{ps}$  tends to be larger when: (1) the specimen has a higher tendon profile; and (2) the specimen has less number of strands (less prestressing).

**Table 6-1** Prestress measured at load cells for different stages

	B4H	B4L	B5L	D3H	D3L	D4H	D4L
$f_{ps\_exp}$	1652.5	1563.3	1460.8	2141.0	2044.1	2083.6	1971.7
$f_{ps\_ACI}$	1524.2	1339.5	1315.7	1776.1	1732.5	1725.1	1692.8
$f_{ps\_AASHTO}$	1368.9	1301.5	1294.3	1710.5	1654.6	1700.9	1647.0
$f_{ps\_Naaman}$	1573.6	1392.4	1353.5	1920.2	1756.8	1839.8	1705.2
$f_{ps\_Harajli}$	1468.8 (1590.0)	1368.7 (1590.0)	1357.7 (1590.0)	1803.9 (2052.0)	1724.5 (1982.1)	1879.2 (2052.0)	1710.6 (1946.6)

$f_{ps\_exp}$ :  $f_{ps}$  based on the measured data and the derived prestress profile at peak load;  $f_{ps\_ACI}$ :  $f_{ps}$  computed by using the equation provided in ACI 318-14;  $f_{ps\_AASHTO}$ :  $f_{ps}$  computed by using the equation provided in AASHTO 2017;  $f_{ps\_Naaman}$ :  $f_{ps}$  evaluated by using the equation suggested by Naaman et al. (2002);  $f_{ps\_Harajli}$ :  $f_{ps}$  evaluated by using the equation suggested by Harajli (2006).

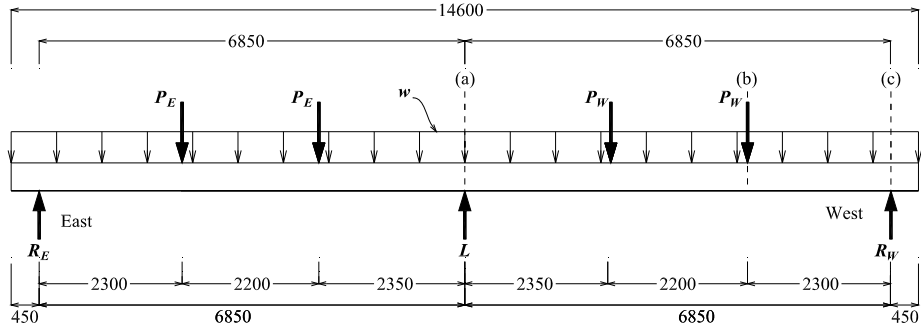
## 6.2 Moment variation

In this chapter, moment variation at each critical section of the specimen during loading test is presented and discussed. To begin with, the statics

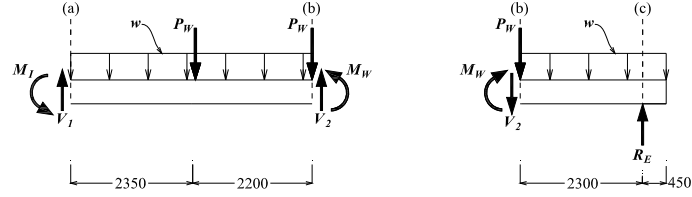
concept was employed to calculate the moment variation at each critical section: the maximum negative moment section at the interior support region and two maximum positive moment sections right at the two exterior loading points. And then the calculated moment variation during the loading test was derived.

### **6.2.1 Static analysis**

In this chapter, static analysis on the test specimens is presented. Because of the characteristic of 2-span beam's indeterminacy, it is impossible to calculate the reaction forces at each support ( $L$ ,  $R_E$ , and  $R_W$ ) even though the magnitude of the loads applied from the actuators ( $P_E$  and  $P_W$ ) are known. By using the load cell under the interior support, however, reaction force at the interior support ( $L$ ) can be obtained and the data can be used to calculate the reaction forces at the other supports ( $R_E$  and  $R_W$ ). From **Figure 6-3 (a)**, the following equations can be derived by using the force equilibrium (**Eq. (6-1)**) and moment equilibrium (**Eq. (6-2)** and **Eq. (6-3)**).



(a) Free body diagram of the full specimen



(b) Free bodies of the west part of a specimen

**Figure 6-3** Free body diagrams using method of sections (Unit: mm)

$$2P_E + 2P_W + w (= 4.32 \text{ kN/m}) \times (14.6 \text{ m}) = L + R_E + R_W \text{ (kN)} \quad (6-1)$$

$$R_W = 0.49635P_E + 1.50365P_W - 0.5L + 31.536 \text{ (kN)} \quad (6-2)$$

$$R_E = 0.49635P_W + 1.50365P_E - 0.5L + 31.536 \text{ (kN)} \quad (6-3)$$

where,  $P_E$  is the half of the actuator force on the east side,  $P_W$  is the half of the actuator force on the west side,  $w$  is the uniform line load of gravity due to self-weight applied throughout the beam,  $L$  is the measured reaction force at the interior support,  $R_E$  is the calculated reaction force at the end support on the east side, and  $R_W$  is the calculated reaction force at the end support on the west side.

By using the  $R_W$  and  $R_E$  derived in **Eqs. (6-2)** and **(6-3)**, two equations which meet moment equilibrium for each of two free bodies in **Figure 6-3(b)** can be obtained and these equations can be solved as simultaneous equations having

$M_I$  and  $M_W$  as unknown values. The values of  $V_I$  and  $V_2$  in **Figure 6-3(b)** can be obtained by using force equilibrium condition of each free body.

$$V_I = 0.5L + 0.49635(P_W - P_E) \text{ (kN)} \quad (6-4)$$

$$V_2 = 0.49635P_E + 0.50365P_W - 0.5L + 19.656 \text{ (kN)} \quad (6-5)$$

$$M_I = 3.4P_E + 3.4P_W - 3.425L + 100.9152 \text{ (kN-m)} \quad (6-6)$$

$$M_E = 1.141605P_W + 3.458395P_E - 1.15L + 56.1978 \text{ (kN-m)} \quad (6-7)$$

$$M_W = 1.141605P_E + 3.458395P_W - 1.15L + 56.1978 \text{ (kN-m)} \quad (6-8)$$

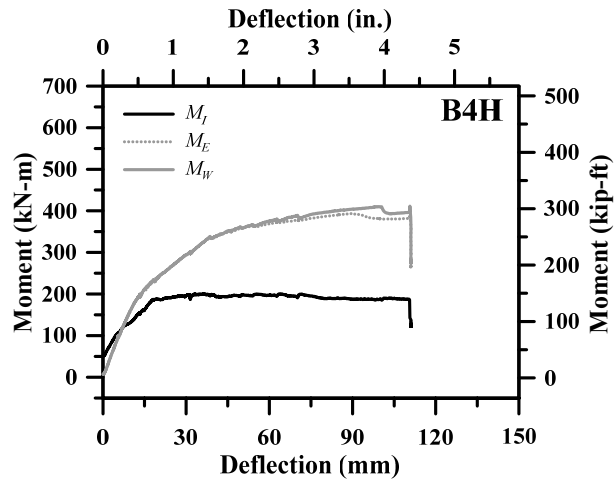
where,  $V_I$  and  $V_2$  are the shear forces at the sections represented in **Figure 6-1(b)**,  $M_I$  is the calculated internal moment at the interior support location by using load cell data,  $P_E$  is the half of the actuator force on the east side,  $P_W$  is the half of the actuator force on the west side,  $L$  is the measured reaction force at the interior support,  $M_E$  is the measured internal moment using load cell data at the maximum internal positive moment location, 4.55 m east of the interior support, and  $M_W$  is the measured internal moment using load cell data at the maximum positive moment location, 4.55 m west of the interior support.

Locations of  $M_I$  and  $M_W$  are important (critical sections) because those locations are the points where the maximum negative and positive moments are expected, respectively. This also means that the first plastic hinge (interior support) and the subsequent hinges (on both spans) are most likely to occur at those locations during moment redistribution behavior in the continuous member. In the same manner,  $M_E$  which is the internal moment at the location 4.55 m east of the interior support can be obtained as shown in **Eq. (6-8)**.

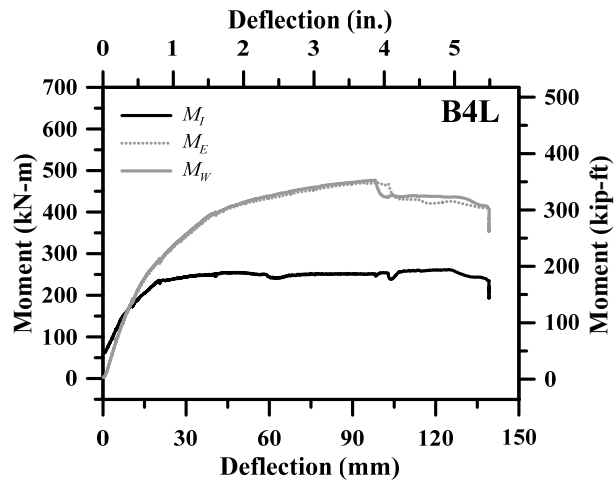
Actuator loads on the east side ( $2P_E$ ) and the west side ( $2P_W$ ) were measured in real time at 1 second intervals. The reaction force at the interior support was also measured with a load cell at 1 second intervals. So, the values of  $M_I$ ,  $M_E$  and  $M_W$  could be calculated throughout the whole loading test.

### 6.2.2 Moment variation

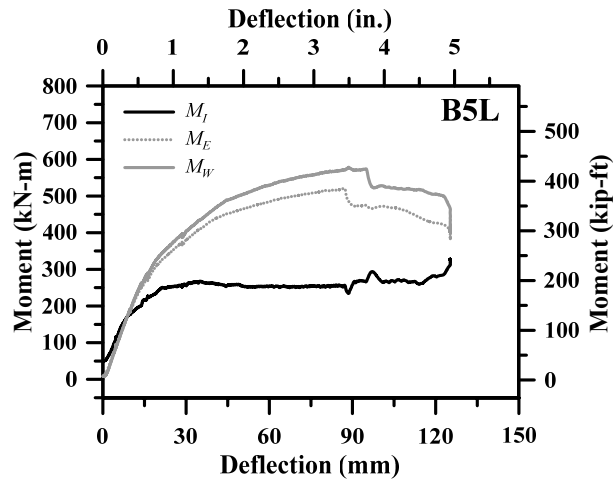
By using Eqs. (6-6), (6-7), and (6-8) derived in Section 6.2.1, the data measured at the two actuators and the load cell under the interior support can be used to calculate the moment values at the critical sections. The moment variations at the interior support ( $M_I$ ) and the other two critical sections ( $M_W$  and  $M_E$ ) of Specimen D3H are presented in **Figure 6-4**. Note that the calculated moment at the interior support ( $M_I$ ) is presented as the absolute value for better comparison. The value of  $M_I$  presented in the figure, however, is calculated to be considerably small compared to  $M_E$  and  $M_W$ . Since the section at the interior support and the maximum positive moment section is symmetrical with respect to the mid-depth of the beam section, the nominal moment strengths in the plastic hinge behavioral zone are expected to be the same (to be precise, not exactly the same due to the prestress variation; see Section 6.1.2).



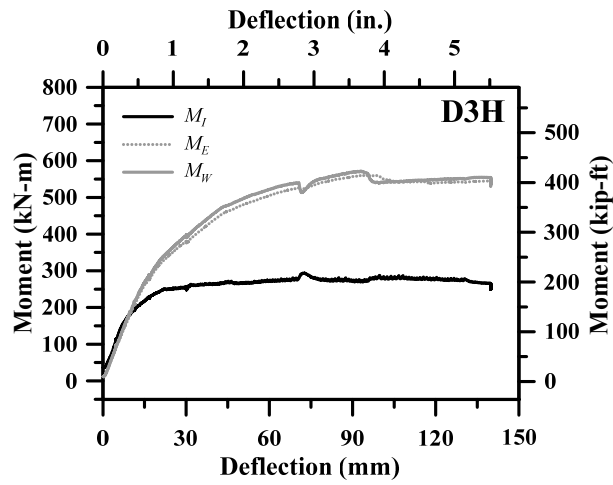
(a) Moment-deflection curves at critical sections of B4H



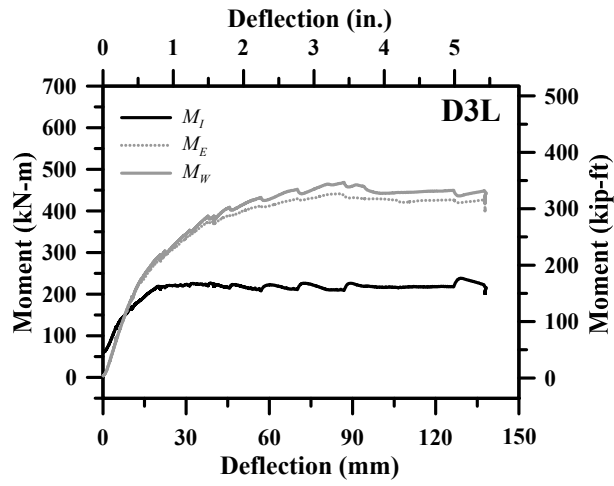
(b) Moment-deflection curves at critical sections of B4L



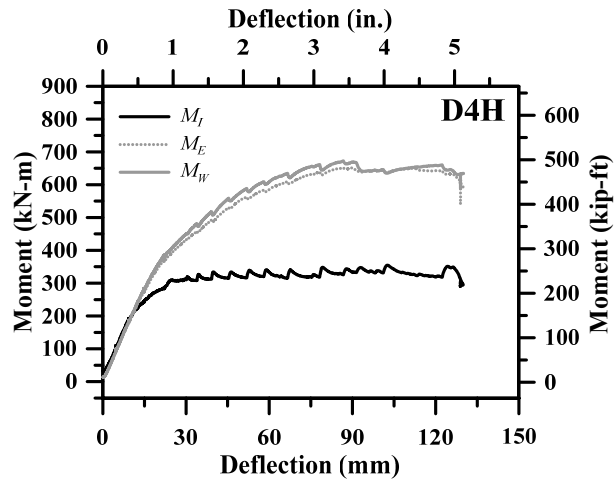
(c) Moment-deflection curves at critical sections of B5L



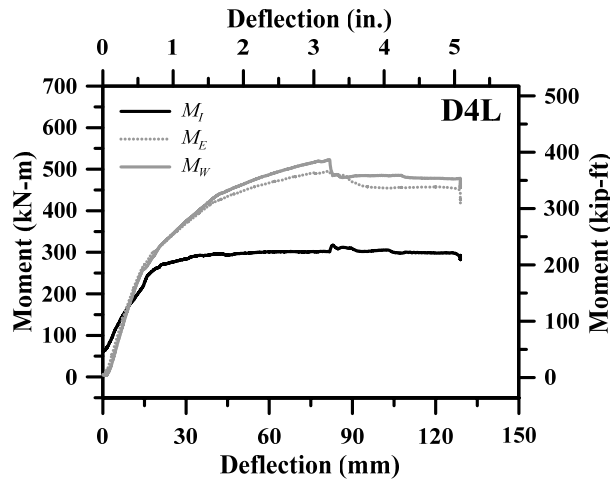
(d) Moment-deflection curves at critical sections of D3H



(e) Moment-deflection curves at critical sections of D3L



(f) Moment-deflection curves at critical sections of D4H



(g) Moment-deflection curves at critical sections of D4L

**Figure 6-4** Moment-deflection curves at critical sections ( $M_I$  is presented in absolute value)

The higher  $M_E$  or  $M_W$  compared to  $M_I$  is because the measured reaction at the interior support was reduced due to the secondary reaction. The member deformed to bend up in the center and this phenomenon counteracted against the actuator loading in a manner that it redistributed the interior support reaction to the end supports (secondary effect). This increased the absolute values of  $M_E$  and  $M_W$  and decreased the value of  $M_I$  according to the developed **Eqs. (6-6), (6-7), and (6-8)**. So, the curves in **Figure 6-4** do not include the secondary moment. More details will be provided in Chapter 8.

### 6.2.3 Data filtering

The data from the load cells (actuators and the reaction at the interior support) were monitored every second and those load cell data went through a low-pass filter using the following equation.

$$y_n = \frac{\tau}{\tau + t_s} y_{n-1} + \frac{t_s}{\tau + t_s} x_n \quad (6-9)$$

where,  $y_n$  is the filtered value at  $n$  second;  $t_s$  is the time interval of the measurement (= 1 second);  $x_n$  is the raw data at  $n$  second; and  $\tau$  is time constant in this study.  $\tau$  was determined to be 20 because the value was found to be the most appropriate to eliminate the noise efficiently and did not distort the graph too much.

### 6.3 Member strength evaluation

In this section, member strength of each specimen is evaluated and discussed. Firstly, hinge model was developed to derive the relationship between the total actuator loads and member strength.

#### 6.3.1 Hinge model

Hinge model developed to evaluate the member strength is shown in **Figure 6-5**. As shown in the figure, three critical sections were assumed to have the same absolute moment strength at the ultimate state of the member. This made the structure as statically determinate structure. Here, “ultimate state” indicates the instance when the total actuator load reaches its peak value. Assuming the full nominal flexural strengths are developed at the critical sections, the total actuator loads can be calculated by using statics.

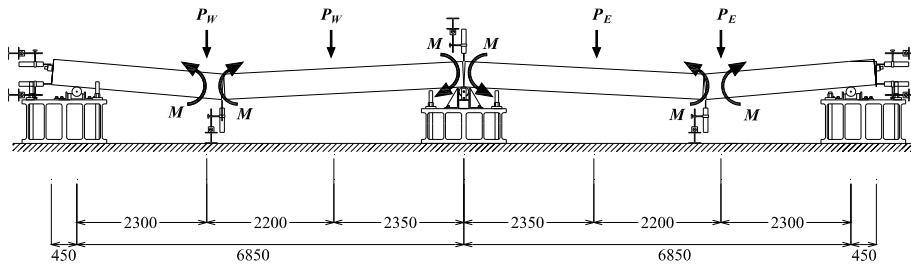
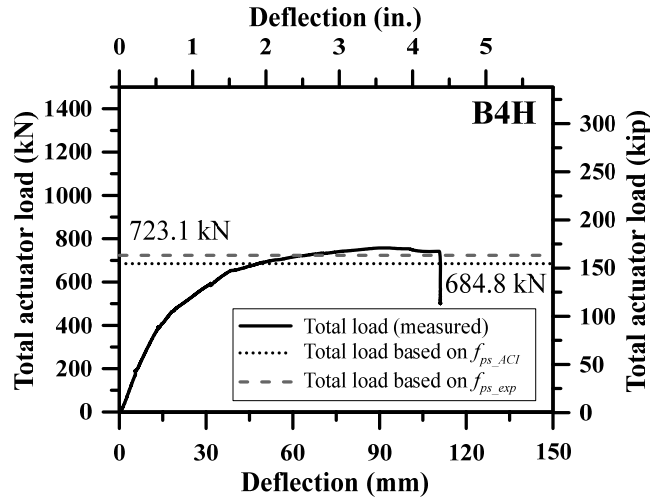
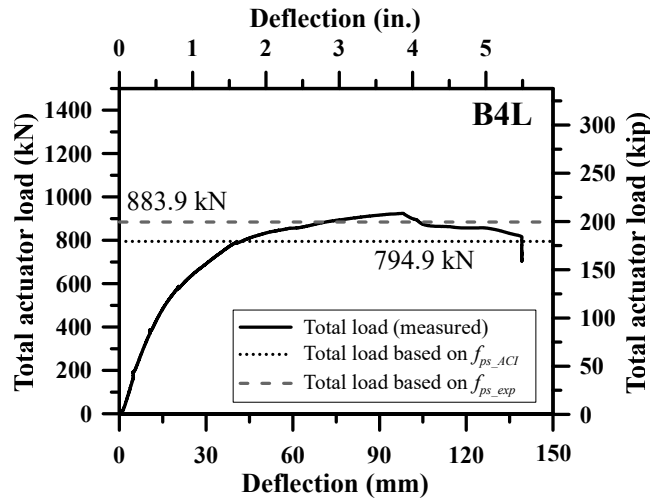


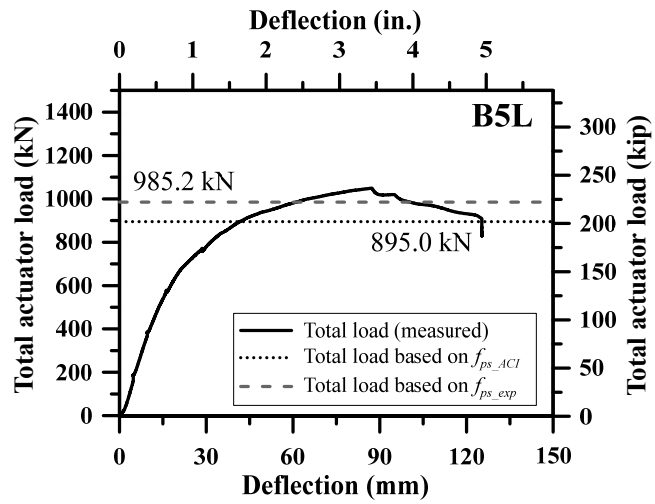
Figure 6-5 Hinge model for strength evaluation (Unit: mm)



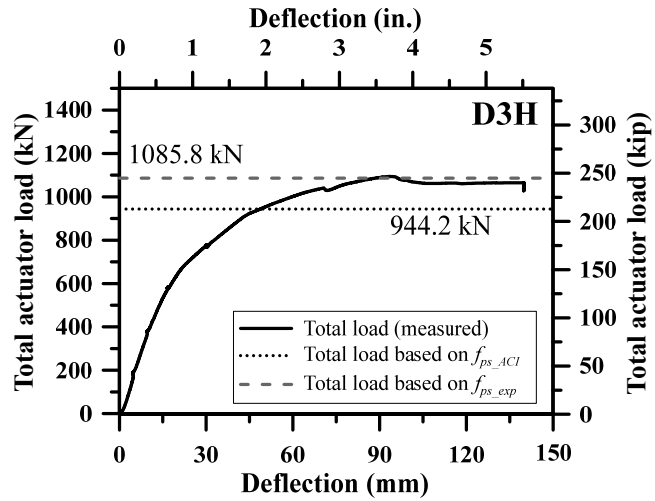
(a) Load-deflection curve of Specimen B4H



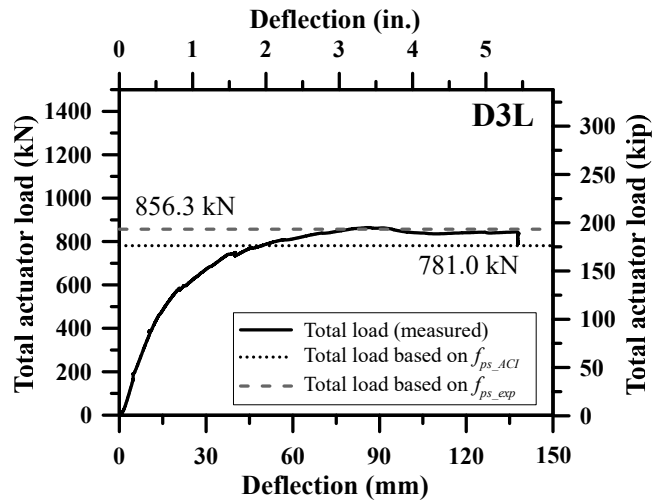
(b) Load-deflection curve of Specimen B4L



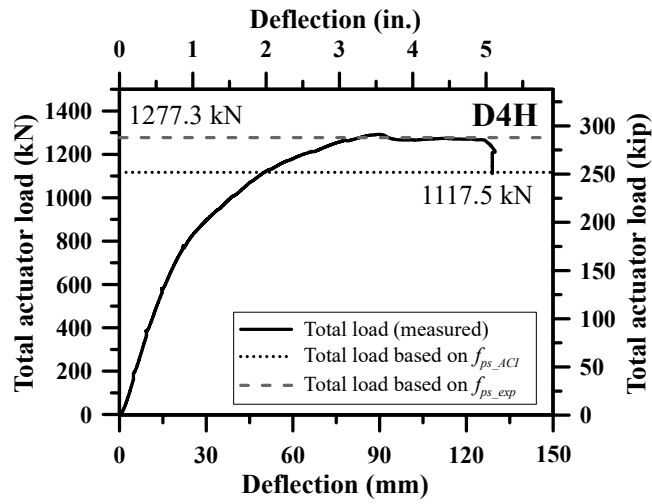
(c) Load-deflection curve of Specimen B5L



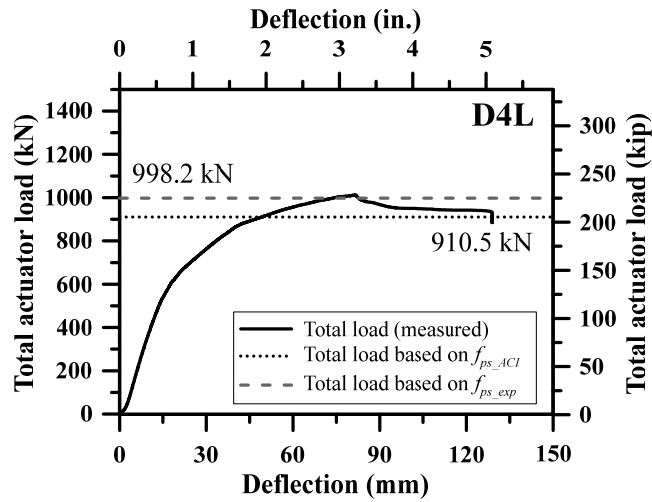
(d) Load-deflection curve of Specimen D3H



(e) Load-deflection curve of Specimen D3L



(f) Load-deflection curve of Specimen D4H



(g) Load-deflection curve of Specimen D4L

**Figure 6-6** Load-deflection curves

**Figure 6-6** shows the load-deflection curve of the specimens. Each dotted horizontal line represents the equivalent total actuator load in **Figure 6-5** using  $f_{ps\_ACI}$  based on the ACI 318-14 code equation and  $f_{ps\_exp}$ . The light dashed horizontal line in **Figure 6-5** represents the equivalent total actuator load using  $f_{ps\_exp}$  which is the evaluated average prestress of the specimens at the peak load. The measured peak load and the equivalent actuator load using  $f_{ps\_exp}$  showed good agreement in most of the specimens and this implies that the assumed hinge model and the evaluated average prestress at peak load worked quite accurately. On the other hand, the member strength evaluated by using ACI equation for  $f_{ps}$  tend to underestimate the member strength, and this corresponds to the results revealed in Section 6.1.3. It appears that the specimens in pair (B4H-D3H; B4L-D3L; B5L-D4L) showed equivalent ductility capacity, which implies that using very high-strength strands instead of ordinary high-strength strands in the flexural members could be feasible in terms of ductility of the members. Comparing the member strengths directly

between the specimens in pair, however, might not be adequate because the specimens in pair were not designed to have exactly the same flexural strength. For comparison of the strength development, it would be more proper to investigate the tendon stress increment until nominal state because the stress development in the prestressing reinforcement at nominal (peak load) state greatly affects the flexural strength of the specimens.

During the loading test, one of the strands in B4H fractured and a piece of the strand shoot out of the member. The strand fractured near the fixed end location. The loading test stopped immediately after this happened. The photos of the jacking end and fixed end at the time of fracture are shown in **Figure 6-7**. Considering the load-deflection curve that the Specimen B4H showed, it was suspected that maybe two of the strands were not anchored properly (did not contribute to the member behavior) and this resulted in the less flexural stiffness and strength as represented in **Figure 6-6(a)**. The dotted line in **Figure 6-6(a)** was estimated based on this assumption and the correspondence between the load-deflection curve and the thick dotted line in the graph backs up this assumption. Thus, it is possible to conclude that the strand fracture occurred in B4H because the specimen was under prestressed than other specimens. This led the other remaining prestressing tendons to burden higher tensile force and led to fracture. This kind of fracture was never discovered in other specimens.



(a) Jacking end

(b) Fixed end

**Figure 6-7** Tendon fracture (B4H)

## 6.4 Discussion

In this chapter, loading test results were investigated and discussed with respect to the prestress variation, moment variation, and the member strength evaluation. The main summaries are as follows.

- 1) Stress in the tendon at the jacking and fixed ends of the specimens was measured during the loading test. The prestress did not vary much when the specimens showed elastic behavior, but started to increase as the specimens developed hinges.
- 2) By considering the measured data at the jacking and fixed ends, it was learned that the prestress varied retaining the same prestress distribution profile during the different loading stages.
- 3) The  $f_{ps}$  for each specimen was evaluated and compared based on the test results and different equations: ACI 318-14, AASHTO (2017), Naaman et al. (2002), and Harajli (2006). It was noticed that the equation suggested by Naaman et al. (2002) provided the most accurate result, yet still on the

conservative side.

- 4) From the discoveries made from the test results, the following trend was found which corresponds to the past studies conducted by many researchers. The  $\Delta f_{ps}$  tends to be larger when the specimen has a higher tendon profile and the specimen has less number of strands (less prestressing).
- 5) Moment variations at the critical sections were derived by using static analysis. Since the analysis used the reaction measured at the interior support location, secondary effect was considered in the estimation and the moment values were influenced by the effect.
- 6) Load-deflection curves were derived based on the measured data and the member strengths were evaluated by using the hinge model, which reduced one degree of indeterminacy.
- 7) According to the load-deflection curves mentioned in 5), it was learned that the specimens with 2400 MPa strands showed good ductile behavior which is equivalent to that of the specimens with 1860 MPa strands.
- 8) The member strength based on the  $f_{ps}$  evaluated using ACI 318-14 equation underestimates the actual member strength. This is because the ACI equation predicting  $f_{ps}$  underestimates the value.

## Chapter 7. Assessment of Applicability of 2400 MPa Strands

### 7.1 Applicability of 2400 MPa strands

To assess applicability of 2400 MPa strands for post-tensioned members instead of 1860 MPa strands, the members with 2400 MPa strands have to show the equivalent performance to those with 1860 MPa strands when the same design codes and requirements were applied. If the members with 2400 MPa strands do not meet or overly exceed the equivalent performance criteria to those with 1860 MPa strands, there needs to be a modification of the design codes to consider the different materials.

“Performance criteria” or “capacities” required for continuous unbonded post-tensioned beams may include: flexural strength, shear strength, flexural stiffness (deflection), ductility, fire resistance, durability, corrosion resistance and resistance to fatigue and so on. In this study, flexural strength and ductility performance were verified against 2-span PT specimens with 2400 MPa strength. Flexural strength will be verified in this chapter by investigating the stress in prestressing reinforcement at nominal state ( $f_{ps}$ ) since  $f_{ps}$  highly affects the flexural resistance and the value varies a lot as the member goes into plastic state. Ductility capacity was fully revealed and verified in Section 6.3 so that the specimens with very high-strength strands showed equivalent ductility compared to the specimens with ordinary high-strength strands.

Flexural stiffness (deflection) does not have to be considered as a feature to be verified because one of the core natures of the unbonded post-tensioned

flexural members is the capability to control the deflection by using prestress. So, as long as the prestressing force is maintained and controlled in the member, the deflection can be calculated and controlled actively in the system, and this concept works regardless of the type of strands. Features such as fire resistance, durability, corrosion resistance, or resistance to fatigue would not be controlling limitations for using very high-strength strands because the use of less but higher strength strands does not change the nature of structural system and it would not affect those capacities much.

## 7.2 Material property

As indicated in Section 6.1.3,  $\Delta f_{ps}$  can be affected by the amount of prestressing and tendon profile height. But these trends were identified only within the same specimen group of strand type. To find out the correlation between  $\Delta f_{ps}$  and the type of strand,  $\Delta \varepsilon_{ps}$ , the strain increment from effective to nominal state, should be investigated. This is important considering that  $f_{ps}$  is a highly member dependent factor and that is why numerous studies on  $f_{ps}$  have focused on finding out the correlation between the nonlinear behavior and the tendon strain variation ( $\Delta \varepsilon_{ps}$ ). In order to look into the difference in behavior between 2400 MPa and 1860 MPa strands in PT members, material tests were conducted as shown in **Figure 4-3**. The samples without chucks were tested and the comparison of stress-strain curves is shown in **Figure 7-1**.

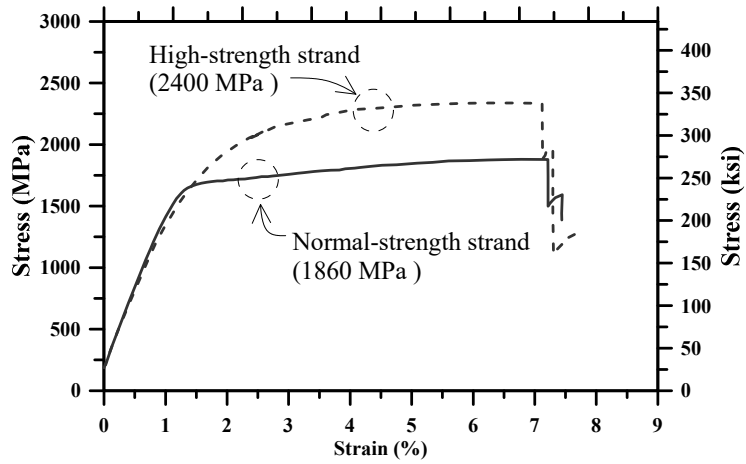


**Figure 7-1** Stress-strain curves of 1860 MPa and 2400 MPa strand samples

In the figure, the slopes of the curve are almost the same at the beginning, but the strands start to have nonlinearity as it goes into plastic behavior zone. It is difficult to identify the distinct difference so each curve is normalized by its own nominal strength in **Figure 7-2**.

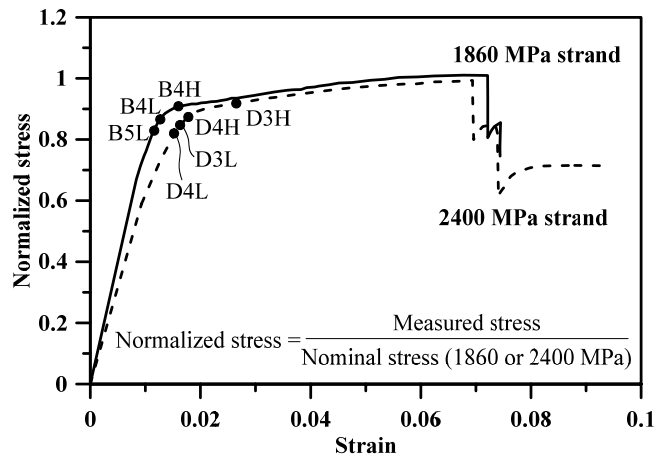


**Figure 7-2** Normalized stress-strain curves of 1860 MPa and 2400 MPa strand samples

On average, effective stresses of both strand types were measured to be about 66 % of their nominal strengths, and the average  $f_{ps}$  was about 86 % of their nominal strengths. So, it was about 20 % of stress increment off of 66 % state of nominal strength, and this stress jump involves a lot of inelastic behavioral range (see **Figure 7-2**). In this respect, normalized curves in **Figure 7-2** are drawn. The black dots on the curves represent the points of each specimen at peak load. According to the figure, the larger strain increment was required for 2400 MPa strands to obtain the equivalent stress jump throughout the total strain range. This implies that from effective stress level to  $f_{ps}$ , 2400 MPa strands should elongate more than the strands with 1860 MPa strength. This is due to the reduced sectional area when the very high-strength strands are used. For example, approximately three 2400 MPa strands would be needed instead of four 1860 MPa strands to obtain the same effective prestressing force. But in order to obtain the same increment of prestressing force, 2400 MPa strands should elongate more because it has 25 % less sectional area to develop the additional strength. This could mean that the members with the very high-strength strands should develop collapse mechanism in a manner that the strand elongates more to obtain the same prestressing force increment. Otherwise, the members with the very high-strength strands could not develop the equivalent stress in prestressing reinforcement at the nominal state of the members.

### 7.3 Equivalent plastic hinge length

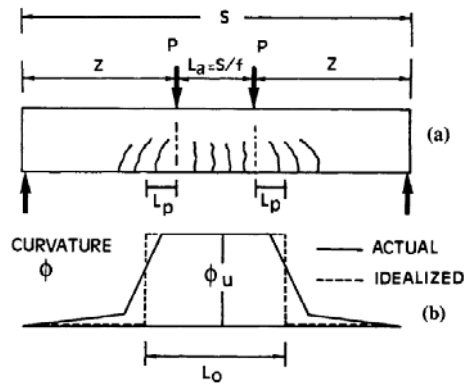


Figure 7-3 Curvature distribution of simply supported beam (Harajli, 1990)

Figure 7-3 shows the curvature distribution of simply supported beam. As shown in the figure, curvature is concentrated at the plastic hinge region. It was discovered in the test results that this plastic hinge development mechanism directly affected the increase of prestress of unbonded tendons. This corresponds to the points made in Section 2.4 that more spans mean more plastic hinges, leading to more prestress increase in the collapse mechanism.

There have been researches which used equivalent plastic hinge length to predict the  $f_{ps}$  in analytical ways. Studies of Pannell (1969) and Tam and Pannell (1976) put great emphasis on “span/depth ratio of the beams” as a factor which can affect ultimate moment resistance of unbonded prestressed concrete beams. In the studies, the authors introduced a ratio of equivalent length of plastic region (plastic hinge length) to neutral axis depth at ultimate to accommodate this. There were other following researches such as Kordina and Hegger (1987), Harajli and Hijazi (1991), and Au and Du (2004) predicting  $f_{ps}$  based on the plastic hinge theory developed in Pannell’s study.

Harajli and Hijazi (1991) evaluated the length of plastic region by using an expression which takes account of geometry of loading and nonlinear analysis in the shear span. This enabled the consideration of the span-depth ratio as one of the controlling factors in predicting  $f_{ps}$ . Harajli proposed an expression for evaluating the equivalent plastic hinge length in his study in 2006 and 2012. The expression accommodated the loading type like it was adopted by Harajli and Hijazi (1991), taking account of the neutral axis depth, which was originally proposed by Tam and Pannell (1976) and proven to be a strongly influential factor in Harajli's study (2006). In this paper, the length of plastic hinge of each specimen was estimated by using the expression developed in the study by Harajli (2006). The equation is presented below.

$$L_p = \frac{\Delta \varepsilon_{ps} L_a}{n_p \left( \varepsilon_{cu} \frac{d_p - c}{c} + \varepsilon_e \right)} \quad (7-1)$$

where,  $L_p$  is the equivalent plastic hinge length;  $\Delta \varepsilon_{ps}$  is the increase in strain in prestressing steel above effective prestrain (based on the data measured at jacking end);  $L_a$  is the length of tendon between anchors;  $n_p$  is the number of plastic hinges;  $\varepsilon_{cu}$  is the ultimate concrete compression strain;  $d_p$  is the depth of unbonded prestressing steel;  $c$  is the neutral axis depth; and  $\varepsilon_e$  is the concrete pre-compression strain.

**Figure 7-4** shows the failure pattern in unbonded members and strain distribution at critical section. The equation is based on the figure which assumes that the strain increment is generated in the plastic hinge region evenly, of which the length is represented as  $L_p$ . With **Eq. (7-1)**, plastic hinge length of the specimens can be calculated.

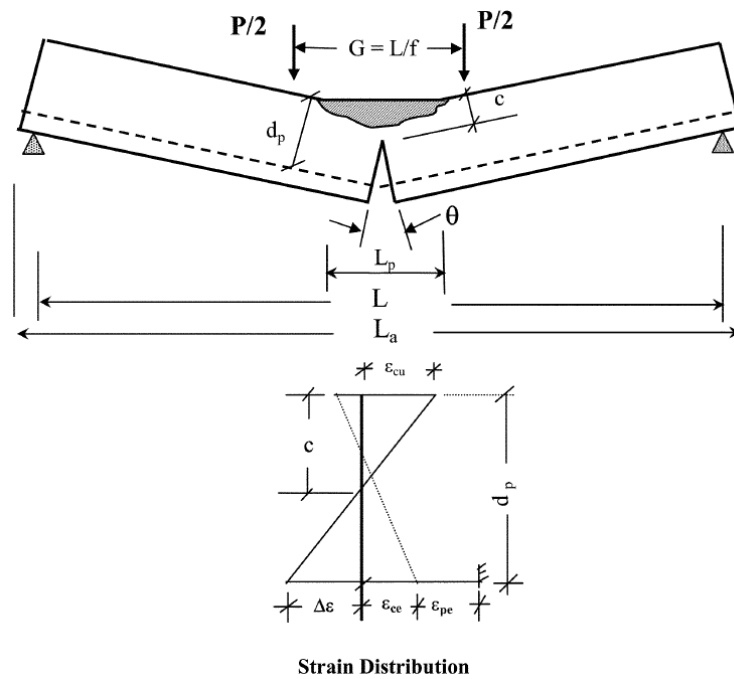


**Figure 7-4** Failure pattern in unbonded members and strain distribution at critical section (Harajli, 2006)

In **Table 7-1**,  $\Delta\epsilon_{ps}$  of each specimen was estimated based on the data measured at the jacking end (from  $f_{se}$  to  $f_{ps}$  state) and the stress-strain curves presented in **Figure 7-1**. Since the stress-strain curves from the sample tests were used, nonlinearity of the material was taken into account. Assuming that three hinges at the critical sections in each specimen have same equivalent hinge length, individual plastic hinge in each specimen can be computed by using **Eq. (7-1)**. Comparing the computed equivalent hinge length in **Table 7-1**, it was noticed that the specimens with the very high-strength strands developed longer plastic hinge lengths ( $L_P^*$ ) than the specimens with the ordinary strands, when other variables were fixed. This explains why very high-strength strands elongated further at the same deflection. Note that  $c$  in **Eq. (7-1)** is affected by the value of  $f_{ps\_exp}$ , and  $f_{ps\_exp}$  is estimated assuming that the stress-strain curve

of the tendon is linear. In **Table 7-1**,  $f_{ps\_exp}^*$  is the modified  $f_{ps\_exp}$  considering the strain hardening effect based on the evaluated strain increment and stress-strain curves, and then  $c^*$  and  $L_p^*$  were derived based on the  $f_{ps\_exp}^*$ , as presented in **Table 7-1**.

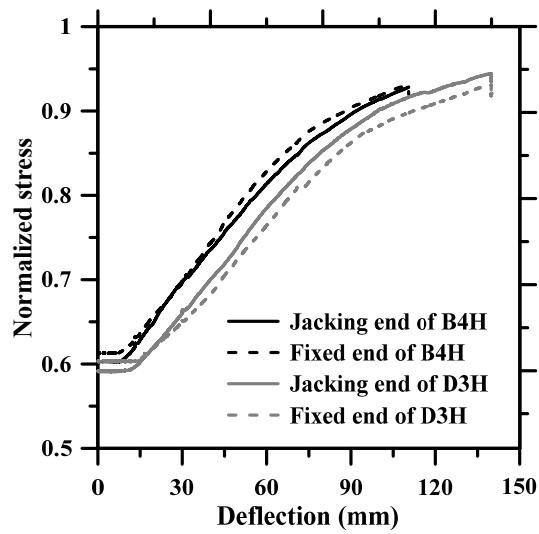
**Table 7-1** Equivalent plastic hinge length calculation sheet

Specimen	B4H	B4L	B5L	D3H	D3L	D4H	D4L
$\Delta\varepsilon_{ps}$ (%)	0.85	0.59	0.41	0.89	0.64	0.71	0.52
$L_a$ (m)	14.6	14.6	14.6	14.6	14.6	14.6	14.6
$\varepsilon_{ce}$ (%)	0.014	0.015	0.018	0.028	0.014	0.037	0.019
$d_p$ (mm)	402	313	402	402	313	402	313
$f_{ps\_exp}$ (MPa)	1690.8	1610.7	1542.1	2203.6	2033.8	2097.62	1968.5
$c$ (mm)	61.4	87.3	99.2	88.8	84.2	105.8	100.8
$L_p$ (mm)	2464.4	3623.8	3000.0	3988.5	3785.9	3966.7	3885.1
$f_{ps\_exp}^*$ (MPa)	1652.5	1563.3	1460.8	2141.0	2044.1	2083.58	1971.67
$c^*$ (mm)	60.82	85.6	95.3	87.1	84.5	105.2	100.9
$L_p^*$ (mm)	2437.2	3528.5	2834.9	3893.5	3804.1	3937.5	3890.7

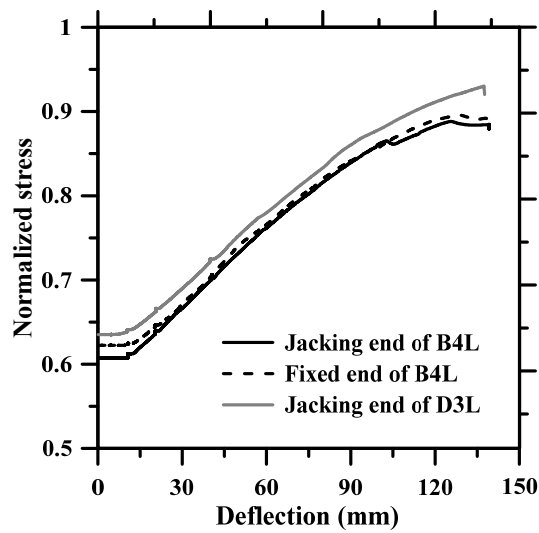
$\Delta\varepsilon_{ps}$ : increase in strain in prestressing steel above effective prestrain (based on the data measured at jacking end);  $L_a$ : length of tendon between anchors;  $\varepsilon_{ce}$ : concrete pre-compression strain;  $d_p$ : distance from extreme compression fiber to centroid of prestressing reinforcement;  $f_{ps\_exp}$ :  $f_{ps}$  based on the measured data and the derived prestress profile at peak load;  $c$ : neutral axis depth;  $L_p$ : equivalent plastic hinge length;  $n_p$ : number of plastic hinges;  $\varepsilon_{cu}$ : ultimate concrete compression strain;  $f_{ps\_exp}^*$ : modified  $f_{ps\_exp}$  considering the strain hardening effect based on the evaluated strain increment and stress-strain curves;  $c^*$ : neutral axis depth based on  $f_{ps\_exp}^*$ ; and  $L_p^*$ : equivalent plastic hinge length based on  $f_{ps\_exp}^*$ .

**Figure 7-5** shows the prestress variation measured at jacking ends or fixed ends according to the deflection of the members with pair specimens. The figure shows that the prestress increase in 2400 MPa strands is equivalent to that of 1860 MPa strands according to the deflection. This observation leaves one question: how come the members with 2400 MPa strands developed longer plastic hinge region than the members with 1860 MPa strands at same

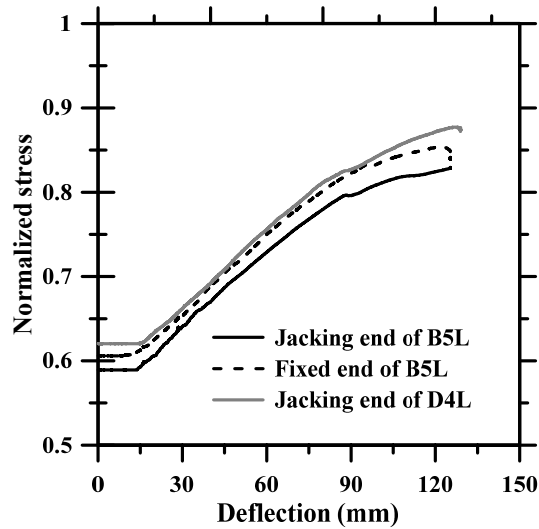
deflection? This can be explained by investigating the plastic collapse mechanism which is going to be covered in Section 7.4.



(a) Comparison of prestress variation (B4H and D3H)



(b) Comparison of prestress variation (B4L and D3L)



(c) Comparison of prestress variation (B5L and D4L)

**Figure 7-5** Prestress variation measured at jacking ends and fixed ends

#### 7.4 Plastic hinge collapse mechanism assessment

As indicated in Section 7.3, the specimens with 2400 MPa strands developed equivalent amount of  $\Delta f_{ps}$  when the pair specimens with 1860 MPa strands were compared and this could be possible when the tendon elongation of the 2400 MPa strands was greater than that of the ordinary strands. In this section, it was verified that the members with 2400 MPa strands developed wider plastic hinge region than the members with 1860 MPa strands. **Figure 7-6** shows schematic drawings of two 2-span members developing three plastic hinges at critical sections under four pointed loads and those members show the same deflection on the spans. In the figure, member (a) with the wider plastic hinge regions has smaller curvature concentrated in the hinge regions which is wider. At the same deflection on the spans, this results in the smoother curvature variation throughout the total length leading to the larger end rotation geometrically.

End rotation variation of the specimens was calculated based on the horizontal LVDTs installed at the end surfaces of the specimen. **Figure 7-7** shows the end rotation-deflection curves of each specimen and how the rotation was measured by LVDTs. The cross symbol means the peak load point in each specimen. **Figure 4-9(a)** shows the test setup photo of how the horizontal LVDTs were installed to measure the end rotation. The y-axis in the **Figure 7-7** indicates the average end rotation (rad) of both ends. As shown in the figure, the curves of seven specimens showed almost the same results. As the member went into plastic behavior however, the curves diverged. When the pair specimens were compared, it was noted that the specimens with 2400 MPa strands showed greater end rotation as the member went into inelastic behavioral zone. This means that the specimens with 2400 MPa strands showed the feature of the member in **Figure 7-6(a)** whereas the specimens with 1860 MPa strands were on the side of case presented in **Figure 7-6(b)**. In other words, the members with 2400 MPa developed the wider hinge region as the member deformed, having the prestressing tendons elongate more, resulting in obtaining the equivalent prestressing force increment ( $\Delta f_{ps}$ ) as presented in **Figure 7-5**.

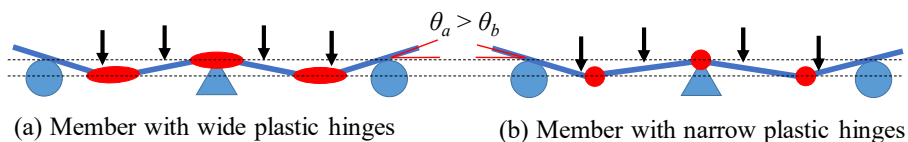


**Figure 7-6** Plastic collapse mechanism with different hinge length

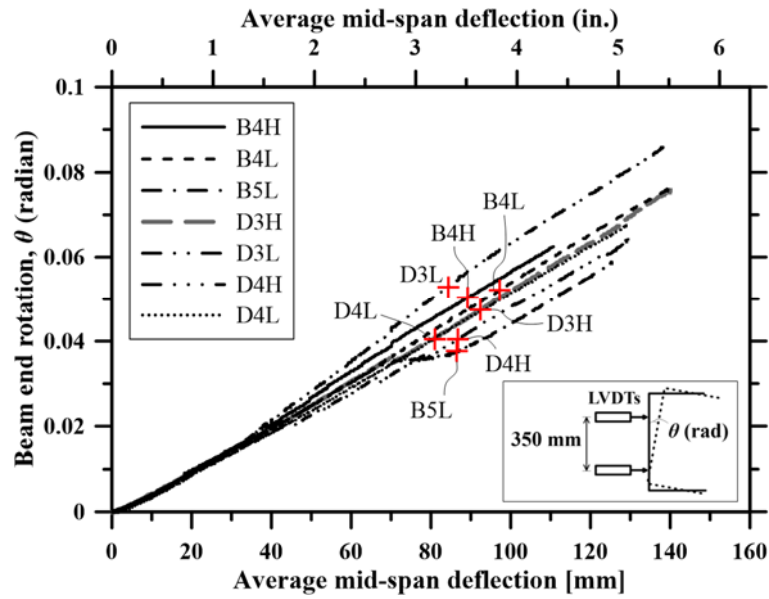
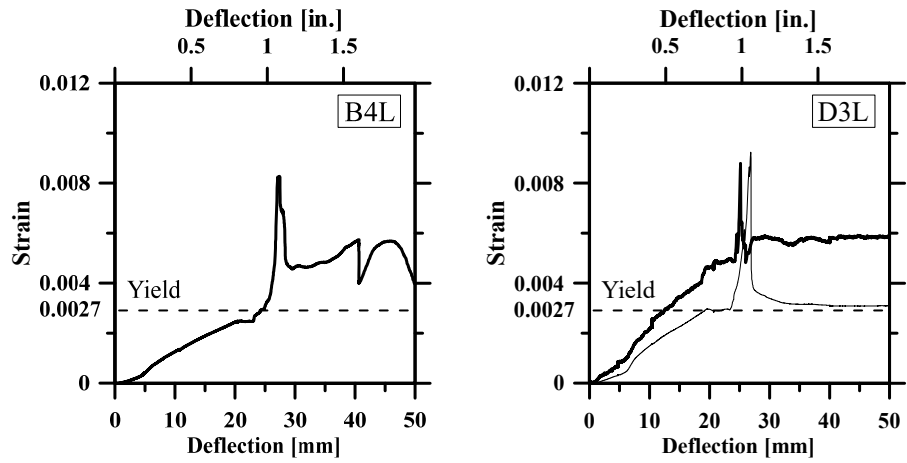


Figure 7-7 Rotation-deflection curves

The reason for the wider plastic hinge region of the members with 2400 MPa strands was considered to be due to the earlier yielding of nonprestressed reinforcement. As strands with 2400 MPa strength did not develop as much prestressing force as 1860 MPa strands at the same amount of elongation, the nonprestressed reinforcement in tension took over more tensile force, leading to yield earlier compared to the one in the members with 1860 MPa strands.

It was revealed from the strain gauges mounted on the tensile nonprestressed reinforcement at the section of interior support location that the tensile nonprestressed reinforcement yielded at the earlier deflection stage in the case of the specimen with 2400 MPa strands compared to their pair specimens with 1860 MPa strands. See **Figure 7-8** for the comparison and Appendix E for the data from the other specimens.



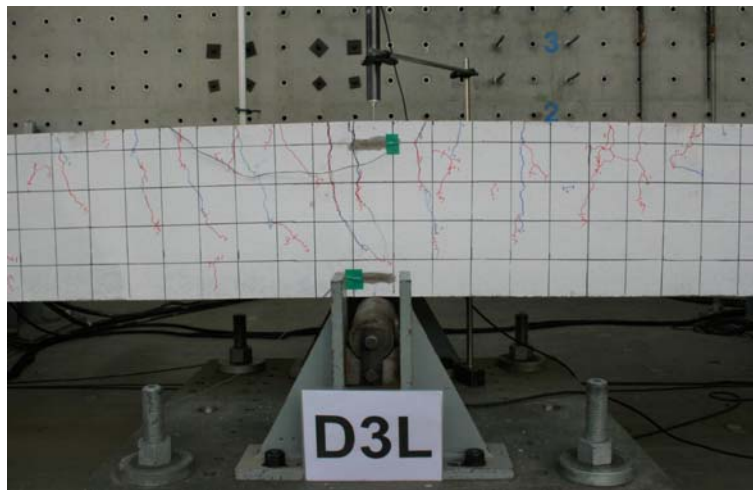
(a) Stain in reinforcing bar in tension (B4L)      (b) Stain in reinforcing bar in tension (D3L)

**Figure 7-8** Strain measured at the reinforcing bar in tension at the interior support

This gap resulted in the different crack patterns as shown in **Figure 7-9** when the paired specimens are compared at the same deflection state. As shown in the figure, the specimens with the higher strength strands (D3L) developed wider hinge region with more and narrower cracks.



(a) Crack pattern at the interior support of B4L at the deflection of 48.5 mm



(b) Crack pattern at the interior support of D3L at the deflection of 48.5 mm

**Figure 7-9** Crack pattern comparison between B4L and D3L

## 7.5 Discussion

In this chapter, feasibility of using 2400 MPa strands instead of 1860 MPa strands was investigated. The main results are summarized as follows:

- 1) Amongst different kinds of capacities of members such as flexural strength, shear strength, ductility, fire resistance, durability, and so on, the feasibility study of using 2400 MPa strands was conducted in the view of flexural strength and associated  $f_{ps}$ .
- 2) From the strand sample tests, it was noted that the stress range that the strands experienced while developing the nominal stress involved the stress range where strain hardening effect became distinct. From the normalized stress-strain curves of the strand samples, it was learned that 2400 MPa strands should have developed greater  $\Delta\varepsilon_{ps}$  to obtain the same amount of normalized stress increment than 1860 MPa strands. This was due to the reduced sectional area of prestressing reinforcement when 2400 MPa strands were used.
- 3) Equivalent hinge length concept has been deployed by many researches over the decades to analytically investigate  $f_{ps}$  in unbonded tendons. In this section, one of the methodologies to estimate equivalent plastic hinge length was used (Harajli, 2006). It was learned that the specimens with 2400 MPa strands were calculated to have the wider equivalent hinge length than those with 1860 MPa strands.
- 4) From prestress-deflection curves, it was noted that the stress increase occurred equivalently in the 2400 MPa strands when they were compared with the 1860 MPa strands. It was revealed that the specimens with higher strength of strands developed the wider hinges, resulting in greater strain increment and almost equivalent stress increment in prestress.
- 5) In this chapter, the discovery illustrated in discussion 4) was verified by conducting plastic hinge collapse mechanism using geometrical feature

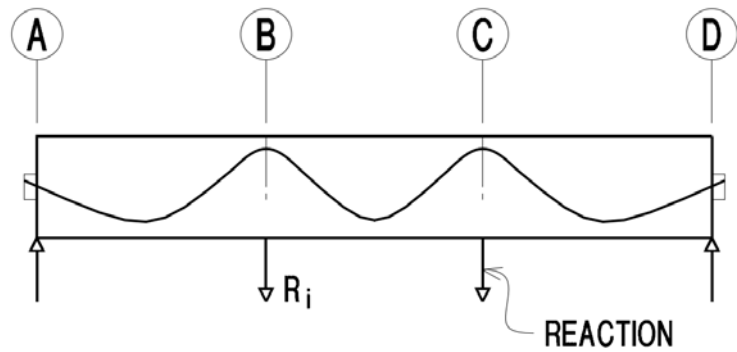
and end rotation data of the members, photographic analysis of the hinge development as well as steel gauge investigation.

## Chapter 8. Evaluation of Secondary Moment

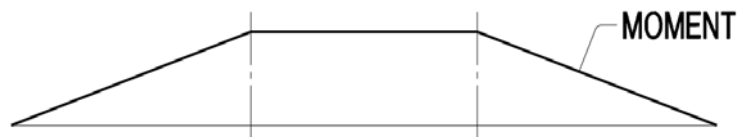
### 8.1 Secondary moment

Secondary moment (or force) in unbonded post-tensioned system is generated by the prestressing force in statically indeterminate structures. This effect is caused by support restraint and does not occur in statically determinate structures. The current ACI 318 code specifies that this effect shall be included in the load combination of strength design because they act like external forces to the members. Since the specimens were 2-spanned beams, which are statically indeterminate structures, the secondary moment and the secondary reaction were anticipated. In this chapter, the secondary effect was measured, estimated, and analyzed.

By using the load balancing method, secondary effects of the indeterminate structures can be evaluated. The secondary moment at a particular section of the member is also defined as the difference between the balanced load moment and the primary moment and presented in **Eq. (2-10)**. Primary moment can be calculated as  $Pe$ , where  $P$  is the prestressing force in the section of interest, and  $e$  is the eccentricity from c.g.c. to the center of prestressing force. **Figure 8-1** shows the secondary reactions and the secondary moments.



(a) Prestressing reactions in beam on support (secondary actions)



(b) Secondary moments due to prestressing support reactions

**Figure 8-1** Secondary reactions and moments (Aalami, 1990)

## 8.2 Secondary moment estimation

In this section, methodology used to estimate secondary moment is presented. Generally, it is known that secondary moment can be calculated by using the conventional method using the **Eq. (2-10)**. However, it was noted from the experimental results that there was a significant discrepancy between the actual member behavior and the calculated values from using **Eq. (2-10)**. It was learned that the discrepancy highly varied depending on the different loading stages.

### 8.2.1 Flexural behavior at the interior support location

**Eqs. (6-6), (6-7), and (6-8)** were derived based on the measured data from the two load cells in the actuators and a load cell under the interior support. Due

to the secondary effect, reaction force of the interior support was redistributed to the both end supports and this led to that the absolute total internal moment value of  $M_I$  (load-induced internal moment at the interior support) deducted by  $M_{2_I}$ , which is the positive secondary moment at the interior support location, and the absolute total internal moment values of  $M_E$  and  $M_W$  (those at mid-span) plus  $0.336M_2$ .  $M_E$  and  $M_W$  are the internal moments at the maximum positive moment section on the east and west spans, respectively, measured using load cell data. See **Figure 8-2** for the detail. This is also mentioned in Section 6.2.2. **Figure 8-3** shows the hypothetical loading stages of the specimens where the secondary reaction is assumed to be constant, where  $M_{2_E}$  and  $M_{2_W}$  are the secondary moments at the critical sections on the west and east span, respectively.

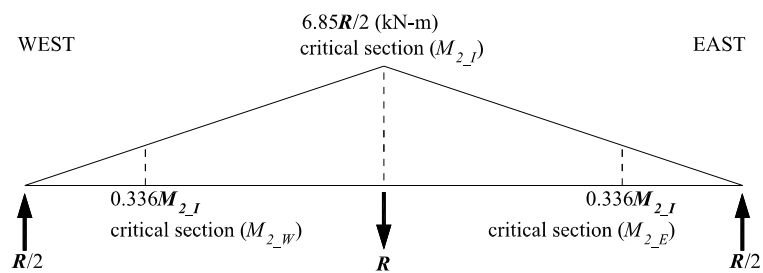


**Figure 8-2** Secondary moment diagram

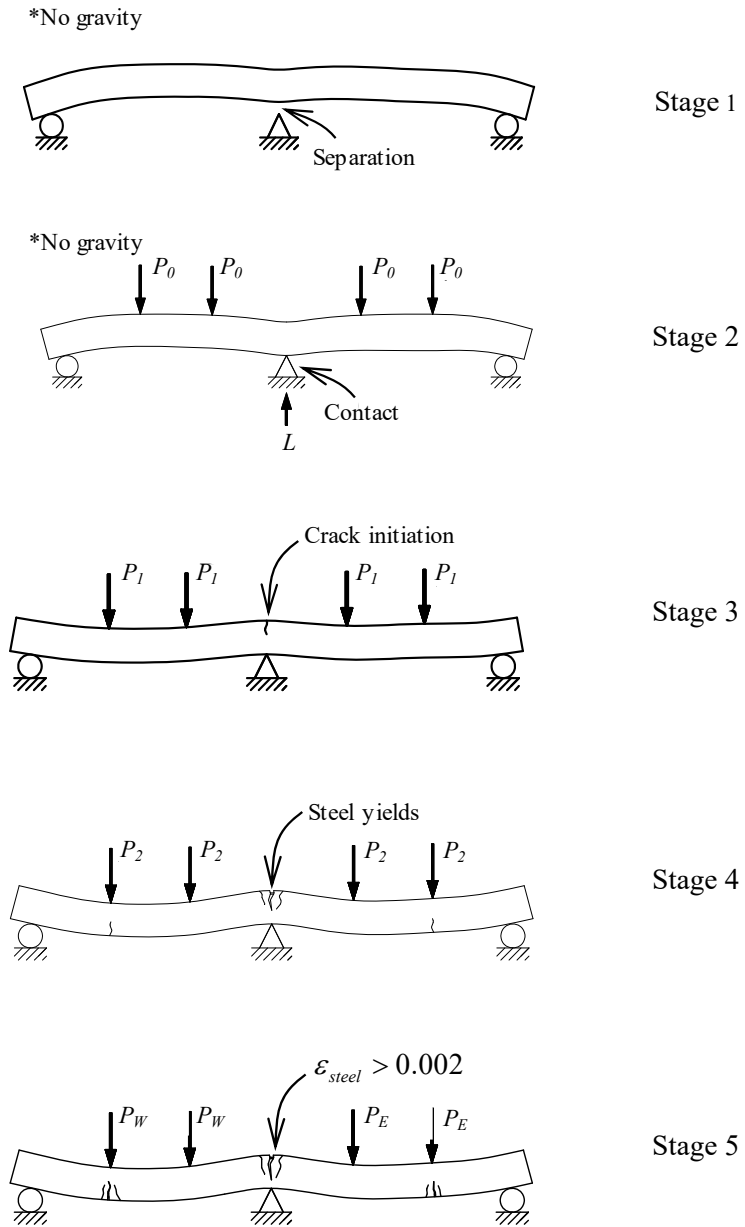


**Figure 8-3** Member behavior depending on different loading stages

In **Stage 1**, there is no gravity or any loading applied to the specimen. Only the internal prestressing force applied to the concrete and this makes the member bent up, resulting in the interior support separated from the member.

**Stage 2** represents the actuator loads applied up to  $P_0$  level until the member barely touches the interior support as shown in the figure, yet the interior reaction ( $L$ ) is still zero. So, this actuator forces all flow through the member to the end support resulting  $2P_0$  of reaction each at the end support. Since the secondary moment is assumed to be constant,  $P_0$  is assumed to be constant here. Up to this stage, gravity is not taken into account in an attempt to correlate the relationship between the applied actuator loads and secondary reaction only. From statics-computation point of view, this load of  $4P_0$  is applied, making the absolute value of  $M_I$  (internal moment at interior support location) to be smaller by  $M_{2-I}$  ( $= 6.80P_0$ ), compared to the internal moment only due to applied loads, and the value of  $M_E$  or  $M_W$  larger by  $0.336M_{2-I}$ , compared to the value of internal positive moment only due to applied loads.

In **Stage 3**, gravity loads and additional actuator load are applied until the first crack initiates at the interior support location. The specimen portions on the east and west spans bend down resisting the additional load. Occurrence of the first crack at the interior support location implies that the section at the interior support has lost some concrete contribution to tension, resulting in the reduced flexural stiffness. This implies that the stress in the extreme tension fiber of the concrete at the interior support location reached to  $f_r$ , where  $f_r$  is the modulus of rupture of concrete. The initiation of the first crack also indicates that the member is in between the uncracked elastic and plastic behavior ranges prior to the mild steel yielding state of the member.

In **Stage 4**, the longitudinal reinforcing bars at the section of the interior

support start to yield. From “Stage 3” to “Stage 4”, the distance from extreme compression fiber to neutral axis ( $c$ ) in the interior support section decreases while resisting additional load. Beyond “Stage 4”, the section at the interior support location is regarded as hinge state.

In **Stage 5**, the actuator load reaches its peak at this stage. The stress in prestressing reinforcement at nominal flexural strength ( $f_{ps}$ ) can be evaluated based on this point. Around this stage, concrete in compression at the critical sections on the both spans crushes. The hinge model introduced in the Section 6.3.1 is suggested assuming that the first hinge at the interior support and the second hinges on the both spans develops the same moment resistance as hinges at the peak load. In the experiment, the concrete portion in compression at the interior support location did not crush out because of the bearing effect produced by the interaction of the geometrical feature of the interior support and the adjacent concrete portion of the member (i.e., c-c-c-node). This might allow this section to have longer moment arm resulting in a bit larger moment resistance than the other two hinge sections.

### **8.2.2 Evaluation of secondary moment**

In this study, the combination of elastic and inelastic approaches based on three different behavioral zones (elastic, transition, and plastic) was used for the estimation of internal moment and secondary moment only at the interior support location. The estimated value of the internal moment at the interior support location only due to applied loads was then compared with monitored value of  $M_I$ , and the difference value was taken as the secondary moment of the section. The approach was based on the hypothetical step-by-step approach made in **Figure 8-3**, where the three different behavioral zones were identified based on the plotting trend of the monitored moment  $M_I$ , as: 1)

elastic zones in the moment-displacement curve showing linear relationship; 2) plastic zones where the moment increase rate with respect to displacement abruptly becomes flat; and 3) the range of the transition zones between the end of the elastic zone to the start of the plastic zone. A sample of the identified zones is presented in **Figure 8-4**, with the rest provided in Appendix D. The  $M_l$  plotted in the appendix was not filtered, so it is a bit different from **Figure 6-4**.

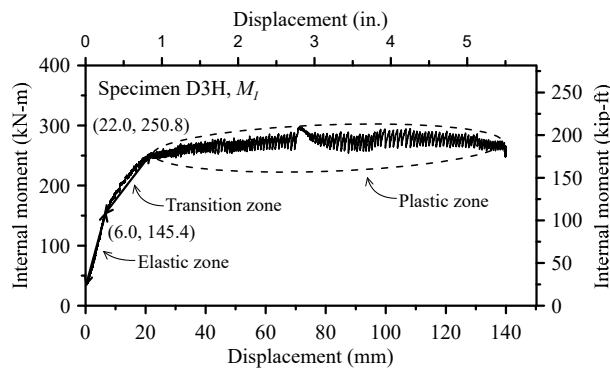


**Figure 8-4** Behavior zone identification of the Specimen D3H

This approach is highly reliant on sectional strain compatibility which is illustrated in **Figure 8-5**. The figure shows strain distribution of the section at the interior support. In the figure, the section presented on the left does not include unbonded prestressing reinforcement. This is because unbonded tendons were considered independent elements, not acting in a composite way, but controlling the concrete stresses independently in a manner that the flexural capacity of the section could be enhanced.

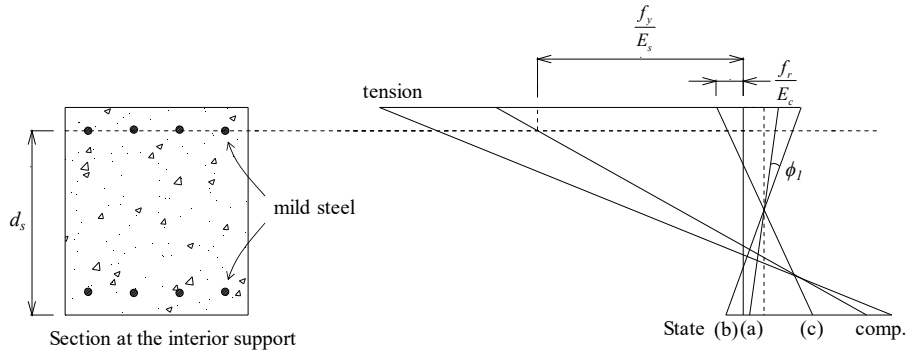


**Figure 8-5** Stress states of the concrete section at the interior support location

In **Figure 8-5**, State (a) represents the stress state where only prestressing force exists, but no secondary moment, gravity, nor actuator load. In State (b), secondary moment is included to State (a) and the curvature change of  $\phi_1$  is made which can be expressed as **Eq. (8-1)**. State (c) is the stress state where the first crack occurs at the extreme concrete tension fiber of interior support section and this state corresponds to the Stage 3 in **Figure 8-3**.

$$\phi_1 E_c I = M_{2\_I} \text{ (kN-m)} \quad (8-1)$$

where,  $\phi_1$  is the curvature change at the interior support location generated by secondary moment,  $E_c$  is the modulus of elasticity of concrete using the equation provided by ACI 318-14 (MPa);  $I$  is the moment of inertia of the transformed section of concrete ( $= 3270 \times 106 \text{ mm}^4$ ); and  $M_{2\_I}$  is the measured secondary moment at the interior support location.

1) Evaluation of secondary moment in elastic zone (Stage 1~3)

The elastic range of  $M_I$  can be identified as the range where the (negative) internal moment shows direct proportional relationship with deflection. Since

the section is in elastic behavior zone, **Eq. (8-2)** is applicable and **Eq. (8-3)** can be derived to estimate the secondary moment in the elastic range.

$$M_{cr} \frac{\Delta_x}{\Delta_{cr}} + M_{2-I} = M_I \text{ (kN-m)} \quad (8-2)$$

$$M_{cr} = - \left\{ Pe + \frac{I}{y} (f_r + P / A_{tr}) \right\} = -65.7 - kP \text{ (kN-m)} \quad (8-3)$$

where,  $M_{cr}$  is the (negative) moment required to make the first crack at the interior support section without consideration of secondary moment;  $\Delta_x$  is the displacement generated by the actuator load in the measured moment-deflection curve (see **Figure 6-4**);  $\Delta_{cr}$  is the total deflection at first cracking in the measured moment-deflection curve (see **Figure 6-4**);  $M_{2-I}$  is the (positive) secondary moment in the elastic range;  $M_I$  is the measured moment using **Eq. (6-6)**;  $I$  is the moment of inertia of the transformed section of concrete ( $= 3270 \times 106 \text{ mm}^4$ ),  $f_r$  is the modulus of rupture calculated using concrete strength measured in the material tests and the formula provided in ACI 318-14 ( $= 4.52 \text{ MPa}$ ),  $P$  is the monitored prestressing force at the interior support location (kN),  $A_{tr}$  is the sectional area of the transformed concrete section ( $= 187429.97 \text{ mm}^2$ ),  $e$  is the eccentricity of the tendon at the interior support location (mm);  $y$  is the distance between c.g.c. and the extreme tension fiber of the interior support section ( $= 225 \text{ mm}$ ); and  $k$  is the constant which is 0.255 for the specimens with high tendon profile and 0.166 for low tendon profile.

## 2) Evaluation of secondary moment in transition zone (Stage 3~4)

Transition zone ranges from the point of crack initiation of concrete to the

point where the nonprestressed reinforcement yields. The point where the nonprestressed reinforcement yields is considered as the starting point of plastic zone. In the transition zone, the secondary moment is evaluated by linearly interpolating between the end point of the elastic zone and the starting point of the plastic zone.

### 3) Evaluation of secondary moment in plastic zone (Stage 4~5)

Plastic zone is identified as the range where the increase rate of the absolute value of  $M_I$  substantially drops and shows a trend of moment hinging. In this zone, secondary moment can be calculated by taking the discrepancy between the (negative) plastic moment calculated based on the  $f_p$  assuming the nominal state and  $M_I$ . This is presented in **Eq. (8-4)**.  $f_p$  is the tendon stress based on the measured stress at the jacking end and the prestress distribution profile in **Figure 5-1**.

$$M_{@f_p} + M_{2-I} = M_I \text{ (kN-m)} \quad (8-4)$$

$$M_{@f_p} \cong - \left\{ f_y A_s \left( d_s - \frac{a}{2} \right) + f_p A_{ps} \left( d_p - \frac{a}{2} \right) \right\} \text{ (kN-m)} \quad (8-5)$$

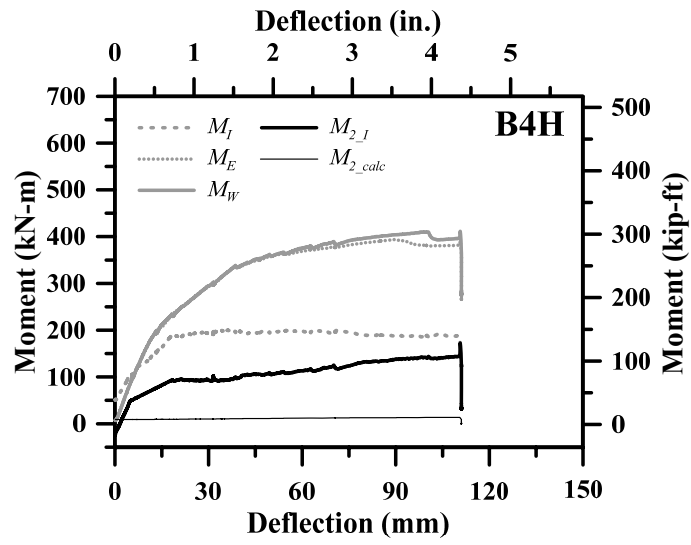
$$a = \frac{f_p A_{ps} + f_y A_s}{0.85 f'_c b} \text{ (m)} \quad (8-6)$$

where,  $M_{@f_p}$  is the (negative) plastic moment at the interior support location estimated based on the monitored  $f_p$ ;  $f_y$  is the yield strength of the nonprestressed reinforcement from the material tests (= 478 MPa);  $A_s$  is the area of nonprestressed longitudinal tensile reinforcement;  $d_s$  is the distance from extreme compression fiber to centroid of longitudinal tension reinforcement;  $f_p$  is the tendon prestress based on the measured stress at the

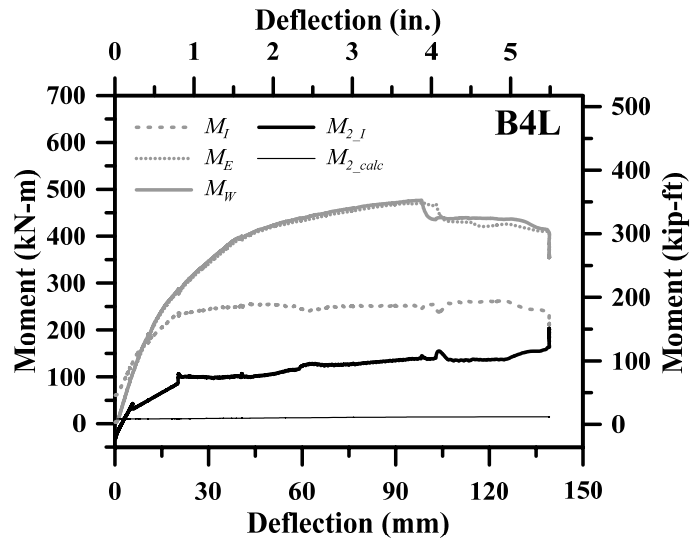
jacking end and the prestress distribution profile in **Figure 5-1**;  $A_{ps}$  is the area of prestressing reinforcement;  $d_p$  is the distance from the extreme compression fiber to the centroid of prestressed reinforcement;  $f'_c$  is the compressive strength of concrete measured from the material tests (= 52.7 MPa); and  $b$  is the width of the specimen.

### **8.2.3 Secondary moment results and discussion**

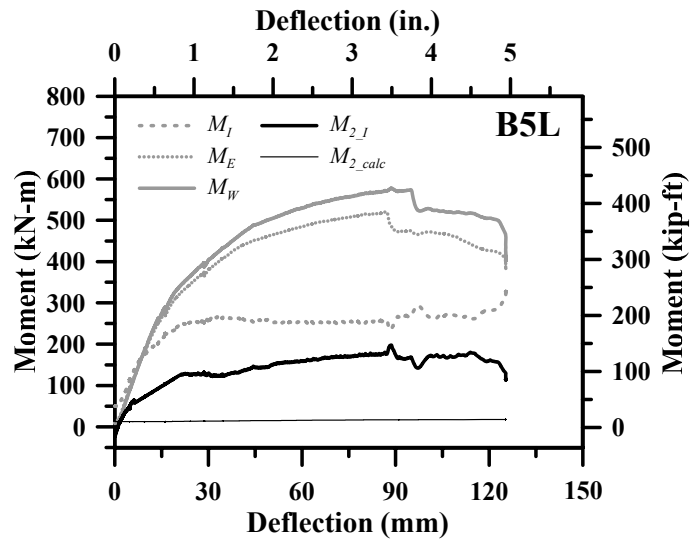
Secondary moment results based on the methodology illustrated from Section 8.2.2 are added to **Figure 6-4** and presented in **Figure 8-5** as  $M_{2\_J}$ . In the figure,  $M_{2\_calc}$  is also presented which is the secondary moment result calculated by using the load balancing method. In the load balancing method, the secondary support reaction and moment were calculated by using finite element computer software and the equivalent load based on the  $f_p$ . In the figure, the secondary moments of Specimen B4H were evaluated assuming that there were only two tendons acting in the system. The  $M_{2\_calc}$  in Specimen B4H showed sudden drop at the end of the curve because the tendon used for monitoring  $f_p$  in the specimen fractured at that point (loading test stopped as well at the point) and the  $f_p$  was used for the prestressing force in the load balancing method. The primary observations are discussed below.



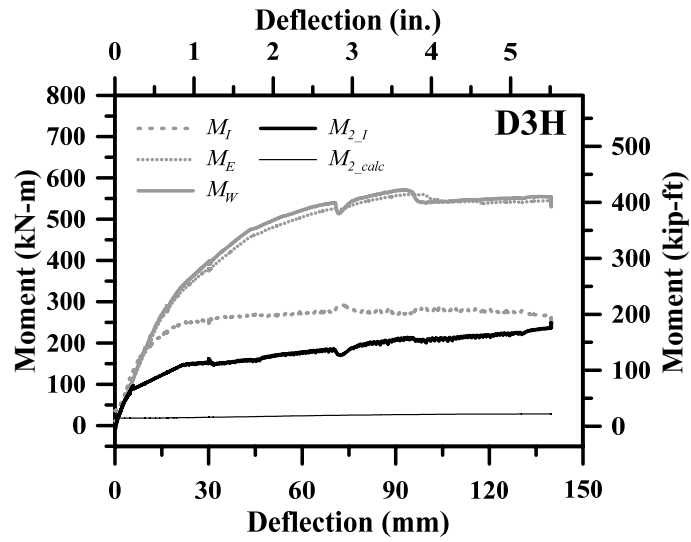
(a) Secondary moment-deflection curve of B4H



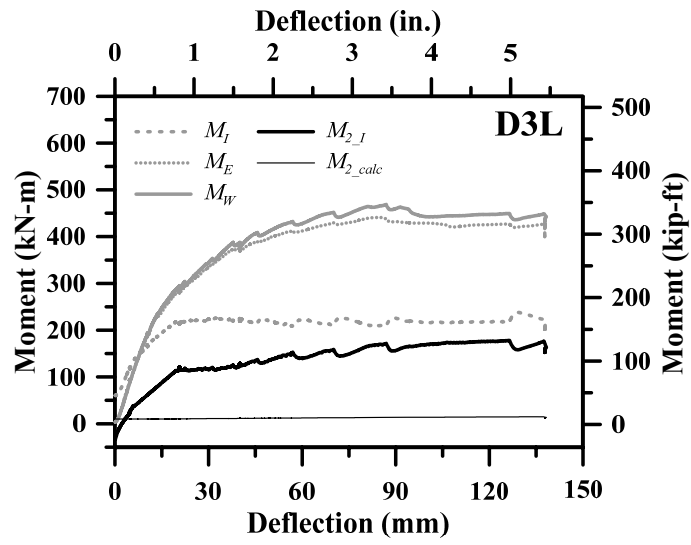
(b) Secondary moment-deflection curve of B4L



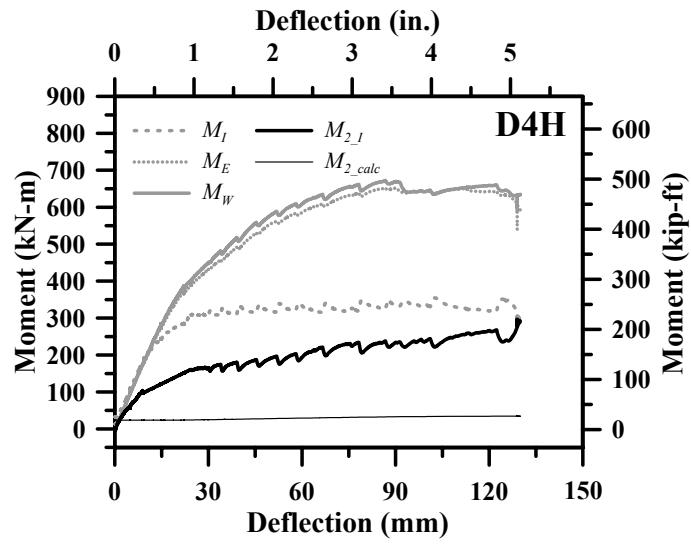
(c) Secondary moment-deflection curve of B5L



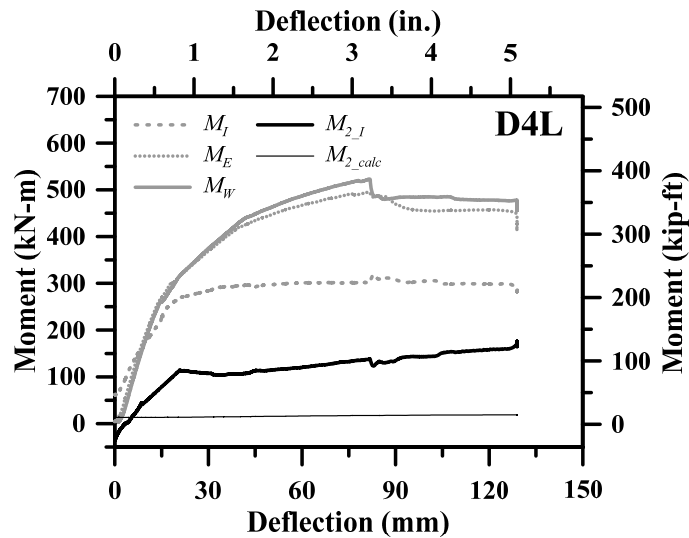
(d) Secondary moment-deflection curve of D3H



(e) Secondary moment-deflection curve of D3L



(f) Secondary moment-deflection curve of D4H



(g) Secondary moment-deflection curve of D4L

**Figure 8-6** Secondary moment curves with the calculated moments

- (1) The monitored  $M_{2_I}$  showed a great rate of increase in the elastic zone and the rate became almost zero as the section at the interior support location reached its plastic state of mild steel yielding. But  $M_{2_{calc}}$ , which was calculated by using load balancing method, showed a steady increase proportional to the monitored prestress  $f_p$ .
- (2)  $M_{2_I}$  and  $M_{2_{I_{calc}}}$  only had a single point of convergence in the elastic zone, and showed great discrepancy as the member underwent the plastic range. Consequently, this led to  $M_{2_I}$  to be significantly greater value than  $M_{2_{I_{calc}}}$ . This implies that the current load resistance factor of 1.0 applied for the secondary moment could significantly underestimate the actual secondary moment in the strength design.
- (3) The specimens with higher tendon profile and more prestressing force tended to show greater secondary effect.
- (4) It was noted that  $M_{2_I}$  showed negative values at the very beginning of the

loading stage. Tracking down for the reason, it was noticed that the magnitude of the measured reaction at the interior support was larger than expected. There are two possible reasons for this: (1) the resolution of the load cell which was used for monitoring the interior support reaction was reported to be up to 1% of its total capacity which is 200 tons. This error could have resulted in the over or underestimation of  $M_I$  by 67 kN-m; (2) three supports might not be totally leveled. In this case, the interior support might be a little bit higher than the other two end supports and this resulted in a bit more concentrated reaction at the interior support.

### **8.3 Discussion**

In this chapter, secondary moment acted in the specimens was investigated and discussed. The main results are summarized as follows.

- 1) Secondary effect in unbonded post-tensioned system is generated by the prestressing force in statically indeterminate structures and this effect was demonstrated in the loading test of the specimens. The current ACI code provisions (ACI 318-14) specifies that this effect shall be included in the load combination for strength design.
- 2) Since the specimens were 2-spanned beams, which are statically indeterminate structures, the secondary effect existed and each was evaluated in two different ways in this thesis: conventional methodology using load balancing method, and the methodology developed in this study.
- 3) The developed methodology in this study divides the behavioral zones of specimen into three zones: elastic, transition, and plastic zones. Three

different approaches were taken for each zone to estimate the secondary moment at the interior support location.

- 4) The obtained result from the developed methodology showed that the secondary moment varied depending on the loading stages. Also, it was noted that the secondary moment evaluated in this study tended to be larger when the specimen had higher tendon profile and larger prestressing force.
- 5) The secondary moment evaluated by using the developed methodology and the secondary moment by using load balancing method showed significant discrepancy as the members underwent into the plastic range. Consequently, this led to  $M_{2_I}$  significantly greater than  $M_{2_I_{calc}}$  in the range. This implies that the current load resistance factor of 1.0 applied for the secondary moment could quite underestimate the actual effect of secondary actions for the strength design.

## Chapter 9. Conclusion

Experiments on the flexural behavior of seven 2-span unbonded post-tensioned beams were conducted under 4-point static loading condition to verify the feasibility of using 2400 MPa strands in a manner consistent with the use of 1860 MPa strands in the post-tensioned beam members. The specimens were designed as half scale, symmetrical about the interior support location, and satisfied the design specification of ACI 318-14 and PTI M50.2-00: Anchorage Zone Design. The variables considered in the test included the strand type, the height of tendon profile, and the amount of prestress. The test results are summarized as follows:

- 1) Prestress variation at the jacking end and fixed end were measured since jacking. It was noted that the prestress at the jacking end experienced the immediate prestress loss due to anchor set behavior and elastic shortening of the concrete. Average long-term loss of 94.4 MPa was also observed in the specimens.
- 2) Based on the discrepancy measured between the jacking end and the fixed end at the moment when the mono-strand jack held the strand, friction between the jacking and fixed ends were evaluated and friction coefficients ( $\mu$  and  $\kappa$ ) were derived.
- 3) During the loading, the prestress did not vary much when the specimens showed elastic behavior, but started to increase as the specimens developed hinges. By considering the measured data at the jacking and fixed ends, it was learned that the prestress varied retaining the same prestress distribution profile during the different loading stages.

- 4) The  $f_{ps}$  for each specimen was evaluated and compared based on the test results and different equations: ACI 318-14, AASHTO (2017), Naaman et al. (2002), and Harajli (2006). All equations provided the prediction on the conservative side, and the equation suggested by Naaman et al. (2002) was found to be the most accurate. Also, it was noticed that  $\Delta f_{ps}$  tends to be larger when the specimen has a higher tendon profile and the specimen has less number of strands (less prestressing).
- 5) Load-deflection curves were derived based on the measured data. According to the obtained curves, it was learned that the specimens with 2400 MPa strands showed good ductile behavior which is equivalent to that of the specimens with 1860 MPa strands. The member strengths were evaluated by using the hinge model. The member strength based on the  $f_{ps}$  evaluated using ACI 318-14 equation underestimates the actual member strength. This is because the ACI equation predicting  $f_{ps}$  underestimates the value.
- 6) From prestress-deflection curves, it was noted that the stress increase occurred equivalently in the 2400 MPa strands when they were compared with the 1860 MPa strands. Even though 2400 MPa strands have to elongate greater to obtain the equivalent  $\Delta f_{ps}$ , it was revealed that the specimens with higher strength of strands developed the wider hinges, resulting in greater strain increment and almost equivalent stress increment in prestress.
- 7) This was verified by followings: the monitored prestress increments; equivalent hinge length calculation; monitored end rotation and strain data at the reinforcing bars; and the photographic analysis of hinge development. These evidence ensures the feasibility of using 2400 MPa

strands in a manner consistent with the use of 1860 MPa strands in the post-tensioned beam members.

- 8) Secondary moment was investigated by using the calculated internal moment at each critical section of the specimens. The internal moment was calculated by using the statics concept and the obtained internal moment at the interior support location was used to estimate the secondary moment in three different behavioral zones of the specimens.
- 9) The secondary moment showed a great rate of increase in the elastic zone and the rate became almost zero as the section at the interior support location reached its plastic state of mild steel yielding. Also, it was noted that the secondary moment evaluated in this study tended to be larger when the specimen had higher tendon profile and larger prestressing force.
- 10) The secondary moment evaluated by using the developed methodology and the secondary moment by using load balancing method showed significant discrepancy as the members underwent into the plastic range. This implies that the current load resistance factor of 1.0 applied for the secondary moment could quite underestimate the actual effect of secondary actions for the strength design.

## References

1. AASHTO (2017), "AASHTO LRFD Bridge Design Specifications, 8<sup>rd</sup> Ed.," American Association of State Highway Transportation Officials, Washington D.C., USA.
2. Aalami, B. O. (1990), "Load Balancing: A Comprehensive Solution to Post-Tensioning," *ACI Structural Journal*, V. 87, No. 6, 662-670.
3. ACI Committee 318 (2014), "Building Code Requirements for Structural Concrete and Commentary (ACI 318-14)," American Concrete Institute, Farmington Hills, MI.
4. ACI Committee 423 (2016), "Guide to Estimating Prestress Loss (ACI 423.10R-16)," American Concrete Institute, Farmington Hills, MI.
5. Allouche, E. N., Campbell, T. I., Green, M. F., and Soudki, K. A. (1998), "Tendon Stress in Continuous Unbonded Prestressed Concrete Members-Part 1: Review of Literature," *PCI Journal*, V. 43, No. 6, 86-93.
6. ASTM A416-06 (2006) "Standard Specification for Steel Strand, Uncoated Seven-Wire for Prestressed Concrete," ASTM International, West Conshohocken, PA.
7. Au, F. T. K., and Du, J. S. (2004), "Prediction of Ultimate Stress in Unbonded Prestressed Tendons," *Magazine of Concrete Research*, V. 56, No. 1, 1-11.
8. Burns, N. H., Charney, F. A., and Vines, W. R. (1978), "Tests of One-Way Posttensioned Slabs With Unbonded Tendons," *PCI Journal*, V. 24, No.2, 110-111.
9. Carroll, J. C. (2009), "Grade 300 Prestressing Strand and the Effect of Vertical Casting Position," Virginia Polytechnic Institute and State University (PhD thesis).
10. Chen, R. (1971), "The Strength and Behavior of Post-Tensioned Prestressed Concrete Slabs with Unbonded. Tendons," University of Texas (Master Thesis).
11. European Committee for Standardization (CEN) (2004), "Eurocode 2: Design of concrete structures – Part 1-1: General rules and rules for buildings," *European standard EN 1992-1-1: 2004: E*, Brussels, Belgium.
12. Harajli, M. H. (1990), "Effect of Span-Depth Ratio on Ultimate Steel Stress in Unbonded Prestressed Concrete Members," *ACI Structural Journal*, V. 87,

No. 3, 305-312.

13. Harajli, M. H. (2006), "On the Stress in Unbonded Tendons at Ultimate: Critical Assessment and Proposed Changes," *ACI Structural Journal*, V. 103, No. 6, 803-812.
14. Harajli, M. H. (2012), "Tendon Stress at Ultimate in Continuous Unbonded Post-Tensioned Members: Proposed Modification of ACI 318, Eq. (18-4) and (18-5)," *ACI Structural Journal*, V. 109, No. 2, 183-912.
15. Harajli, M. H., and Hijazi, S. (1991), "Evaluation of the Ultimate Steel Stress in Unbonded Prestressed Members," *PCI Journal*, V. 36, No. 1, 62-82.
16. Hemakom, R. (1970), "Behavior of Post-Tensioned Concrete Slabs with Unbonded Tendons," University of Texas (Master Thesis).
17. Hill, A. T. (2006), "Material properties of the Grade 300 and Grade 270 prestressing strands and their impact on the design of bridges," Virginia Polytechnic Institute and State University (Master's thesis).
18. Jeon, S., Seo, H., Yang, J., and Youn, S. (2016), "Prestressing Effect of LNG Storage Tank with 2,400 MPa High-Strength Strands," *Journal of the Korean Society of Civil Engineering*, V. 36, No. 6, 999-1010 (in Korean).
19. Kang, T. H.-K., and Wallace, J. W. (2008), "Stresses in Unbonded Tendons of Post-Tensioned flat plate systems under dynamic excitation," *PTI Journal*, V. 6, No. 1, 31-44.
20. Kim, J., Seong, T., and Lee, J. (2012), "Development of 2,160 MPa/2,400 MPa PS Strand and its Application Technology," *Megazine of the Korea Concrete Institute*, V. 24, No. 3, 45-50 (in Korean).
21. Kordina, K., and Hegger, J. (1987), "Determination of the Ultimate Strength in Bending in the Case of Prestressing without Bond," *Beton-und-Stahlbeton*, V. 84, No. 4, 85-90.
22. KS D 7002. (2011) "Uncoated Stress-Relieved Steel Wires and Strands for Prestressed Concrete," Korea Agency for Technology and Standards, Seoul, Korea.
23. Lee, L., Moon, J., and Lim, J. (1999), "Proposed Methodology for Computing of Unbonded Tendon Stress at Flexural Failure," *ACI Structural Journal*, V. 96, No. 6, 1040-1048.
24. Lin, T. Y. (1963), "Load-balancing Method for Design and Analysis of Prestressed Concrete Structures," *In Journal Proceedings*, V. 60, No. 6, 719-742.
25. Mattock, A. H., Yamazaki, J., and Kattula, B. T. (1971), "Comparative Study of Prestressed Concrete Beams with and without Bond," *ACI Journal*, V. 68, No. 2, 116-125.

26. Maguire, M., Collins, W. N., Halbe, K. R., and Roberts-Wollmann C. L. (2016), "Multi-Span Members with Unbonded Tendons: Ultimate Strength Behavior," *ACI Structural Journal*, V. 113, No. 2, 195-204.
27. Naaman, A. E., and Alkhairi, F. M. (1991), "Stress at Ultimate in Unbonded Post-Tensioning Tendons: Part 1-Evaluation of the State-of-the-Art," *ACI Structural Journal*, V. 88, No. 5, 641-651.
28. Naaman, A. E., and Alkhairi, F. M. (1991). "Stress at Ultimate in Unbonded Post-Tensioning Tendons: Part 2-Proposed Methodology," *ACI Structural Journal*, V. 88, No. 6, 683-692.
29. Naaman, A. E., Burns, N., French, C., Gamble, W. L., and Mattock, A. H. (2002), "Stresses in Unbonded Prestressing Tendons at Ultimate: Recommendation," *ACI Structural Journal*, V. 99, No. 4, 518-529.
30. Nilson, A. H. (1987), "Design of Prestressed Concrete," *John Wiley & Sons. Inc.*, New York, N. Y.
31. NZS 3101 (2006), "Concrete Structures Standard: Part 1– The Design of Concrete Structures (NZS 3101– 1)," *Concrete Design Committee P 3101 for the Standards Council*, Wellington, New Zealand.
32. Pannel, F. N. (1969), "The Ultimate Moment of Resistance of Unbonded Prestressed Concrete Beams," *Magazines of Concrete Research*, V. 21, No. 66, 43-54.
33. Park, H., Jeong, S., Lee, S., and Cho J. (2016), "Flexural Behavior of Post-Tensioned Prestressed Concrete Girders with High-Strength Strands," *Engineering Structures*, V. 112, No. 1, 90-99.
34. Park, H., Cho, J. Y., and Kim, J. S. (2012), "Investigation on Applicability of 2400 MPa Strand for Post-Tensioned Prestressed Concrete Girders," *Journal of the Korea Concrete Institute*, V. 24, No. 6, 727-735 (in Korean).
35. PCI Committee on Prestress Loss (1975), "Recommendations for Estimating Prestress Losses," *PCI Journal*, V. 20, No. 4, 43-75
36. PTI (2006), "Post-Tensioning Manual, 6<sup>th</sup> Ed.," Post-Tensioning Institute, Farmington Hills, MI.
37. PTI (2000), "PTI M 10.3-00: Field Procedures Manual for Unbonded Single Strand Tendons," Post-Tensioning Institute, Farmington Hills, MI.
38. PTI (2000), "PTI M50.2-00: Anchorage Zone Design," Post Tensioning Institute, Farmington Hills, MI.
39. Tam, A. and Pannel, F. N. (1976), "Ultimate moment of resistance of unbonded partially prestressed reinforced concrete beams," *Magazine of Concrete Research*, V. 28, No. 97, 203-208.

40. Yang, K.-H., and Kang, T. H.-K. (2011), "Equivalent Strain Distribution Factor for Unbonded Tendon Stress at Ultimate," *ACI Structural Journal*, V. 108, No. 2, 217-226.
41. Yang, J. M., Yim, H. J., and Kim, J. K. (2015), "Transfer Length of 2,400 MPa PS Strand in 15 m-long Full-Scale Pretensioned Prestressed Concrete Beam," *Journal of The Korean Society of Hazard Mitigation*, V. 15, No. 5, 139-146 (in Korean).
42. Yim, H. J., Kim, J. K., and Yang, J. M. (2015), "Experimental Study on the Transfer Length in Pretensioned Prestressed Concrete Beam Using 2,400 MPa PS Strand," *Journal of The Korean Society of Hazard Mitigation*, V. 15, No. 2, 41-49 (in Korean).
43. Zhou, W. and Zheng, W. (2014), "Unbonded Tendon Stresses in Continuous Post-Tensioned Beams," *ACI Structural Journal*, V. 111, No. 3, 525-536.

## **Appendix A : Final drawings**

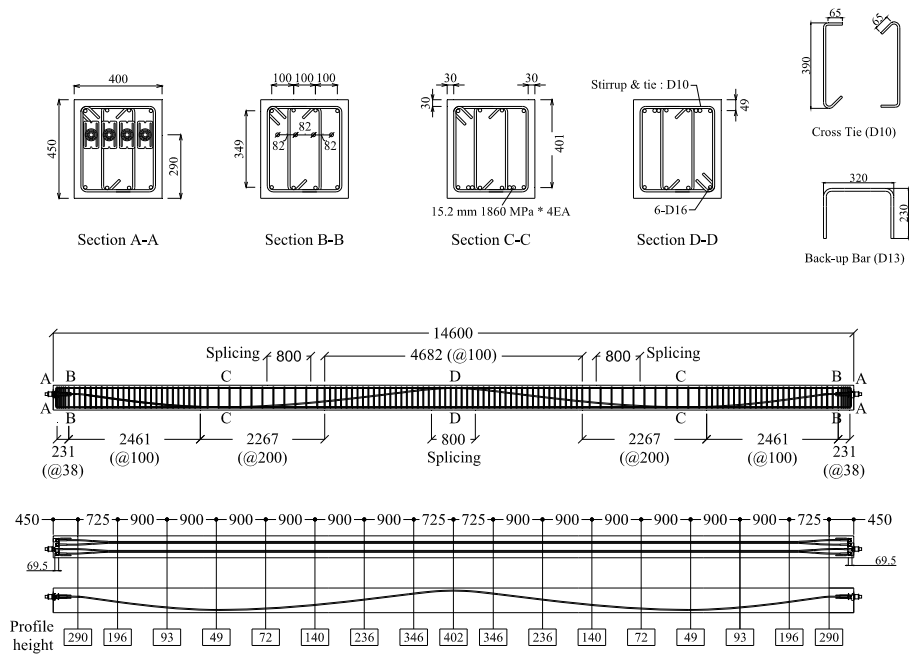


**Figure A-1** Details of Specimen B4H (Unit: mm)

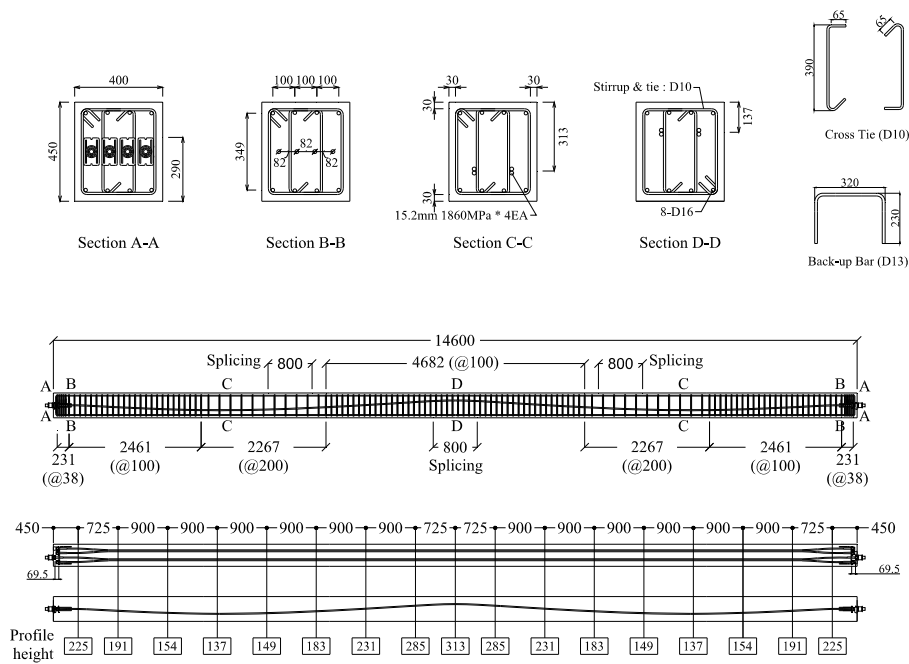


**Figure A-2** Details of Specimen B4L (Unit: mm)

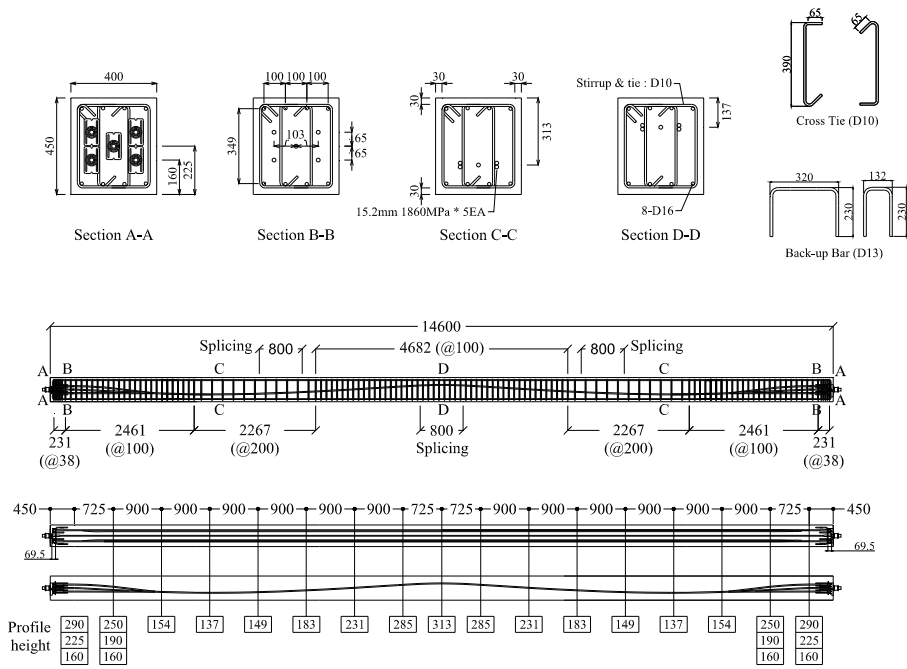


Figure A-3 Details of Specimen B5L (Unit: mm)

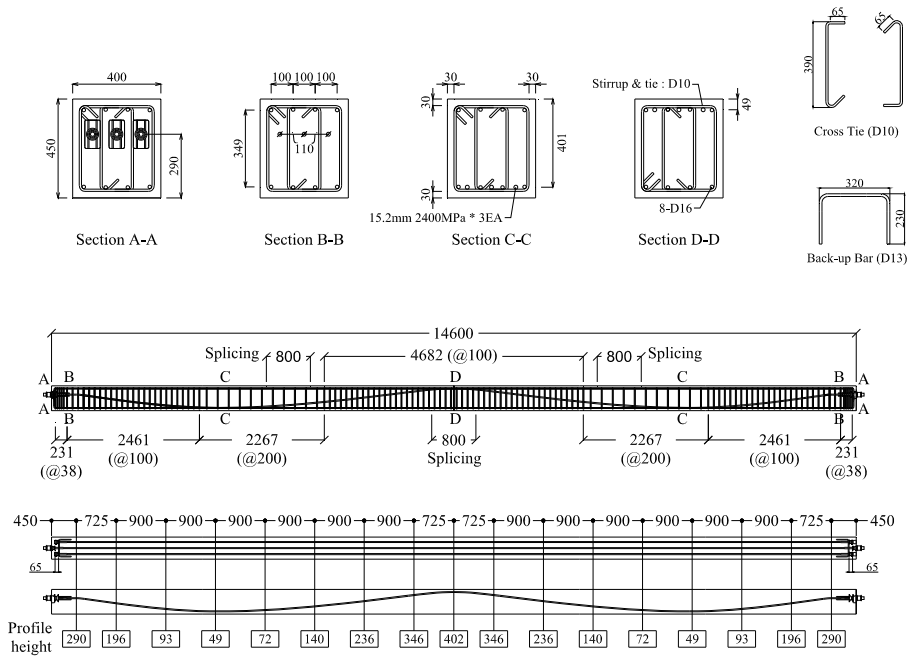
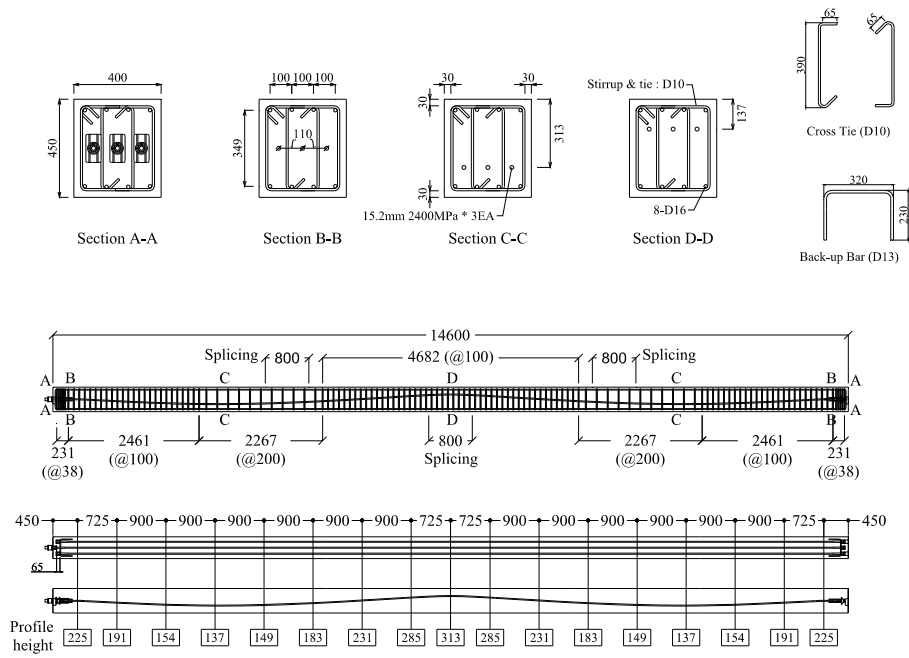
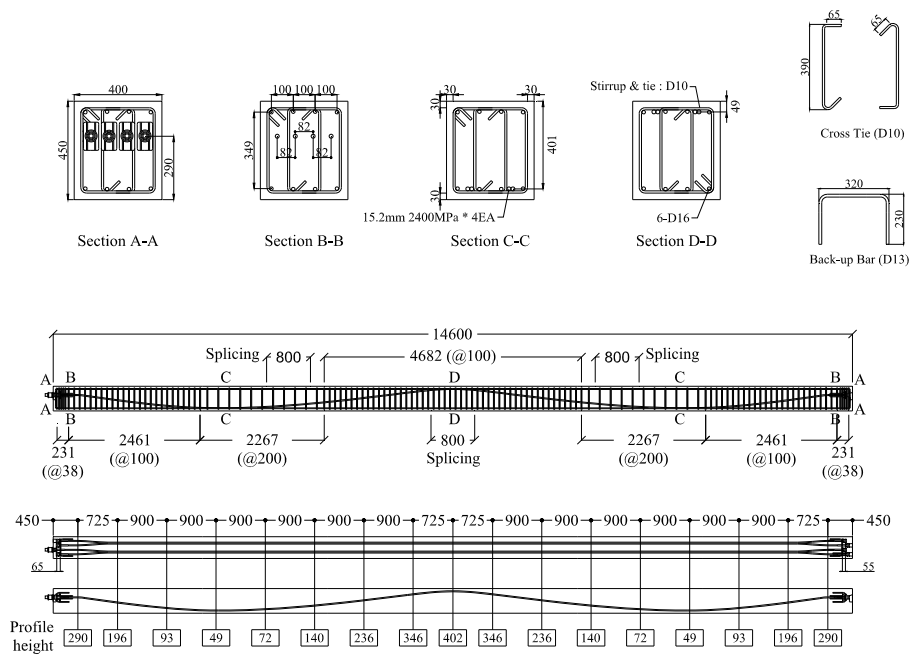


Figure A-4 Details of Specimen D3H (Unit: mm)



**Figure A-5 Details of Specimen D3L (Unit: mm)**



**Figure A-6 Details of Specimen D4H (Unit: mm)**

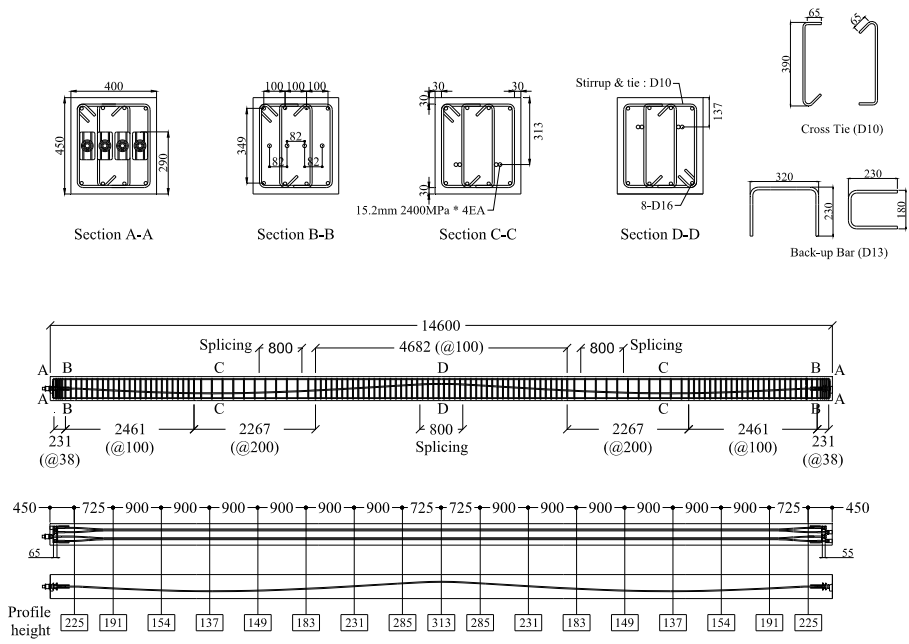
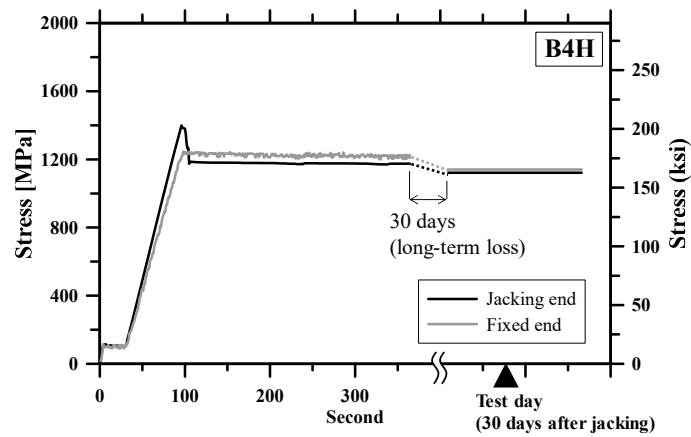
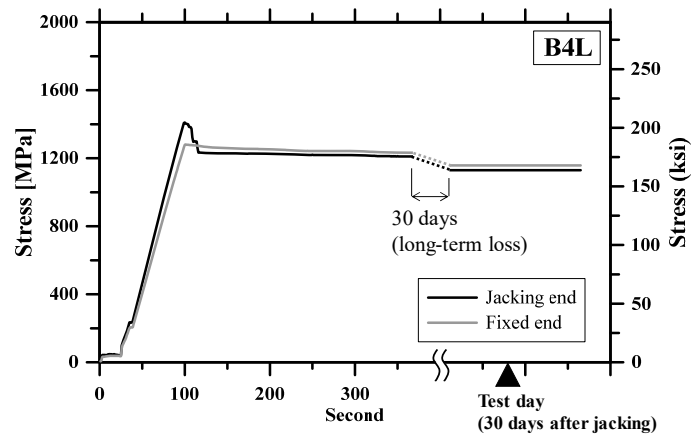


**Figure A-7** Details of Specimen D4L (Unit: mm)

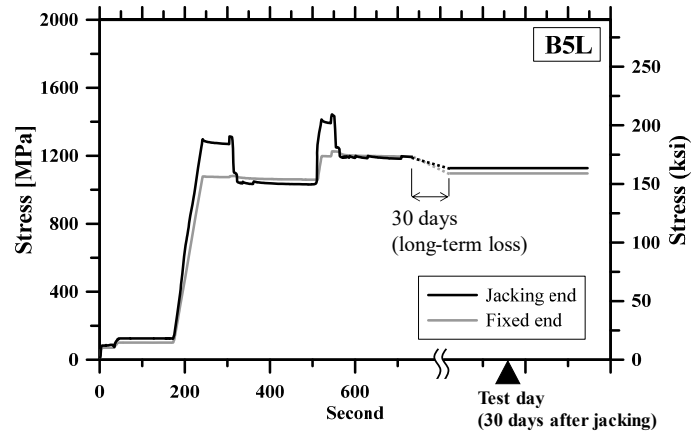
## **Appendix B : Prestress variation during jacking and seating**



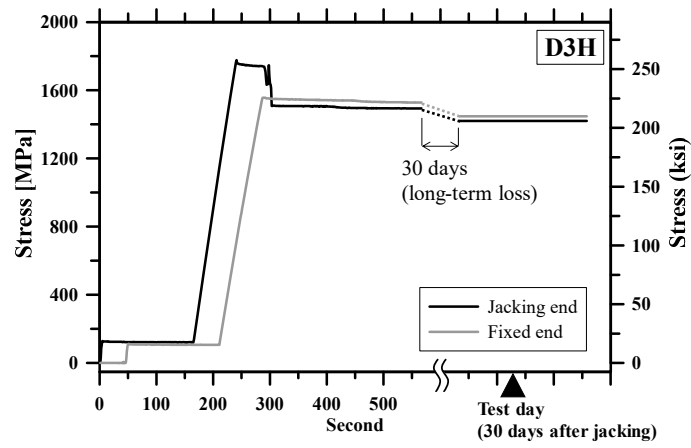
(a) Prestress variation during jacking and seating at the jacking and fixed ends of B4H



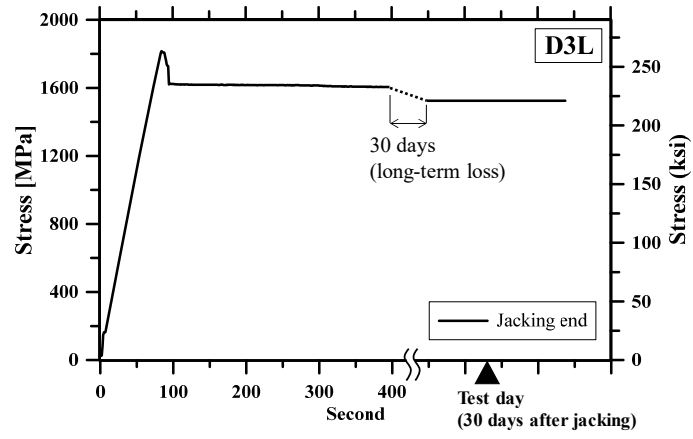
(b) Prestress variation during jacking and seating at the jacking and fixed ends of B4L



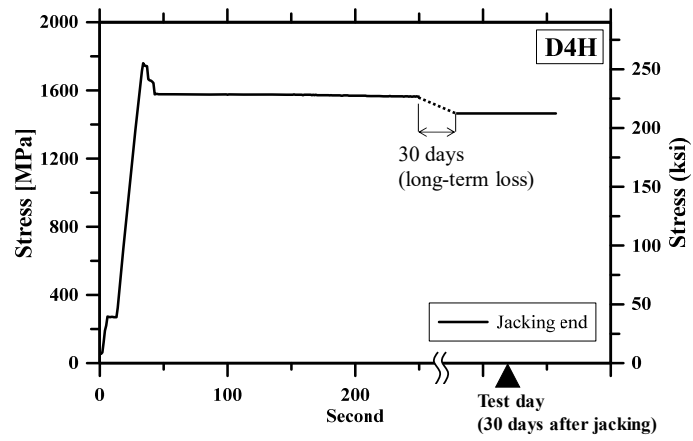
(c) Prestress variation during jacking and seating at the jacking and fixed ends of B5L



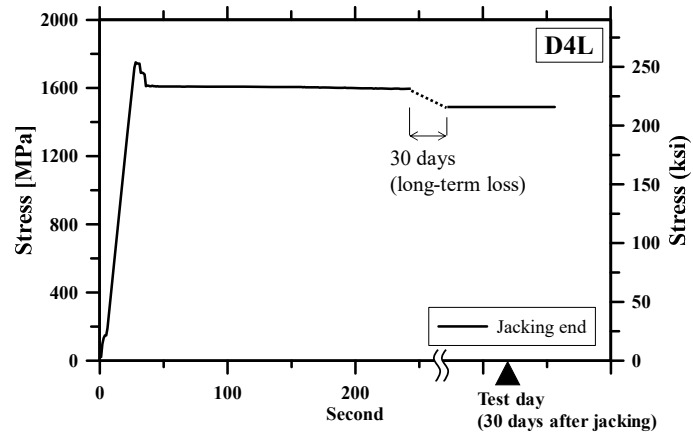
(d) Prestress variation during jacking and seating at the jacking and fixed ends of D3H



(e) Prestress variation during jacking and seating at the jacking end of D3L



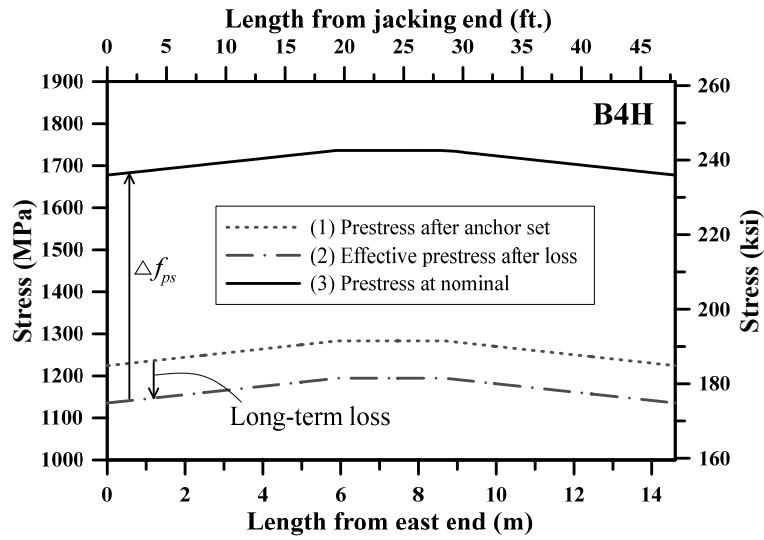
(f) Prestress variation during jacking and seating at the jacking end of D4H



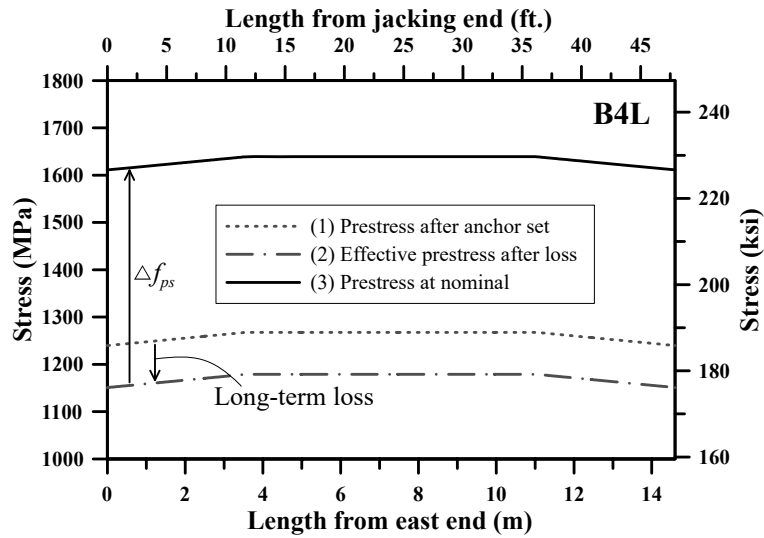
(g) Prestress variation during jacking and seating at the jacking end of D4L

**Figure B-1** Prestress variation measured during jacking and seating

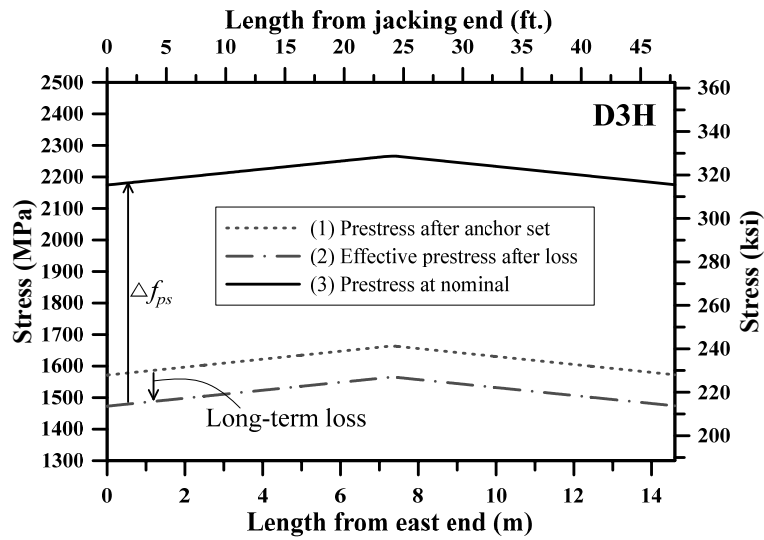
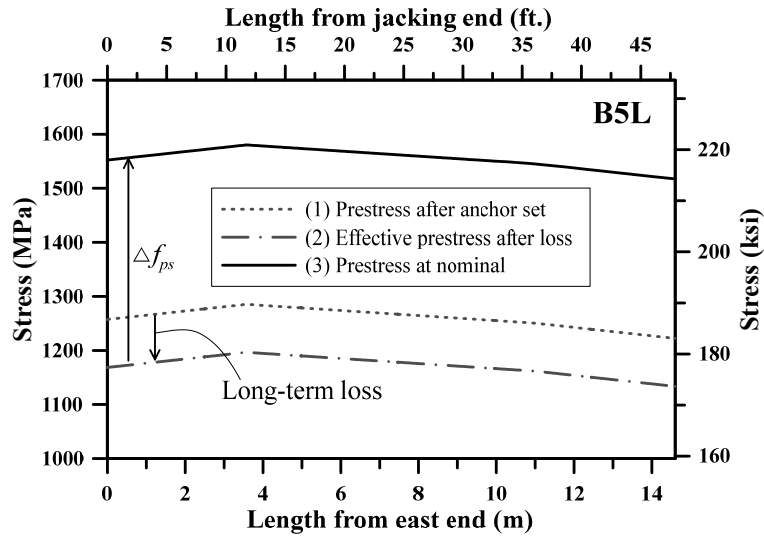
## **Appendix C : Prestress distribution at different stages**

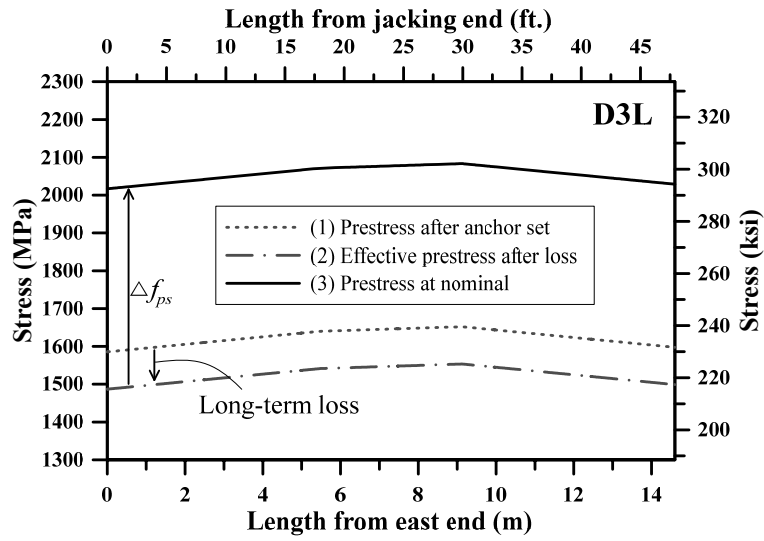


(a) Member prestress distribution profile at different stages (B4H)

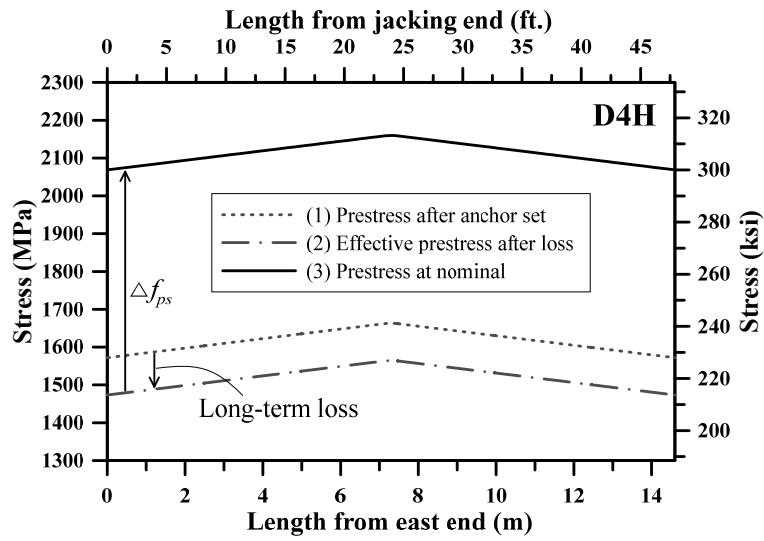


(b) Member prestress distribution profile at different stages (B4L)

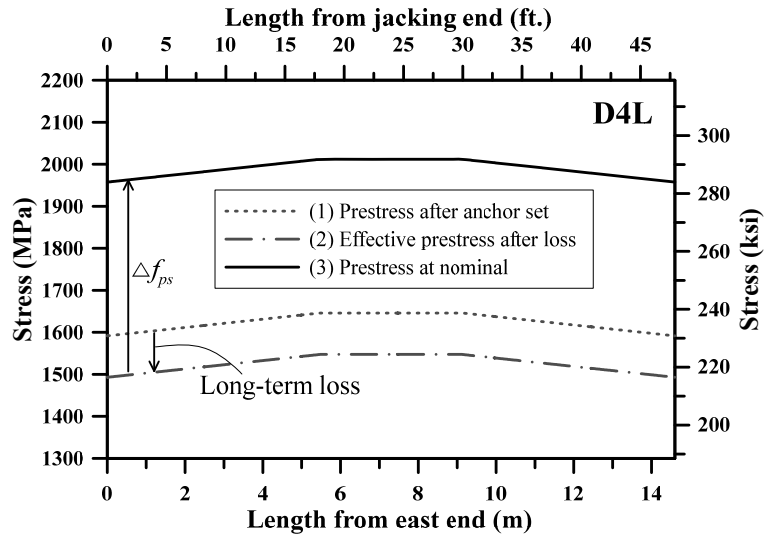




(e) Member prestress distribution profile at different stages (D3L)



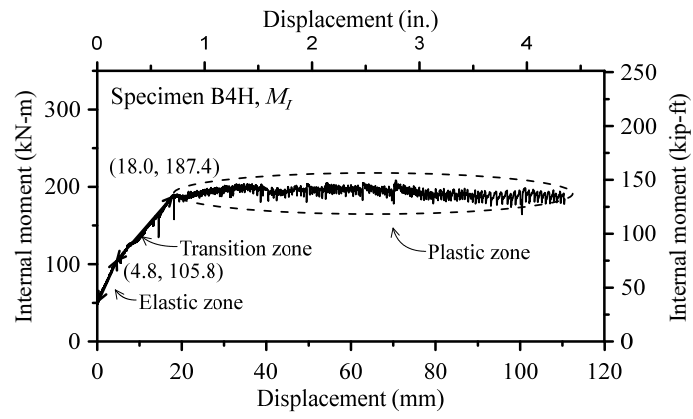
(f) Member prestress distribution profile at different stages (D4H)



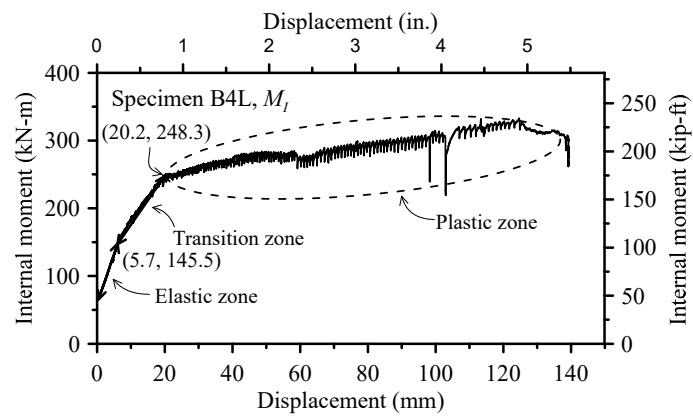
(g) Member prestress distribution profile at different stages (D4L)

**Figure C-1** Prestress distribution profile at different stages

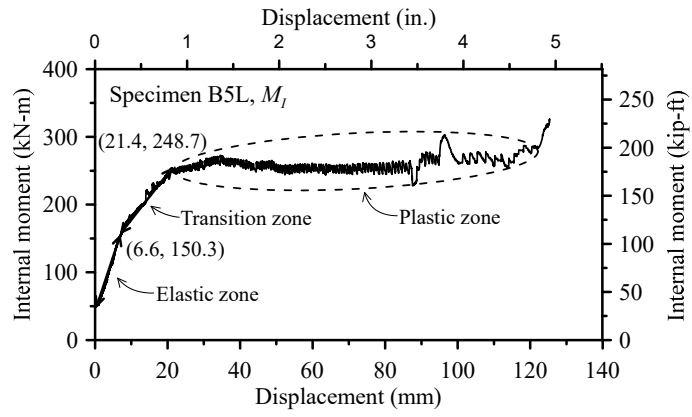
## **Appendix D : Zone identification**



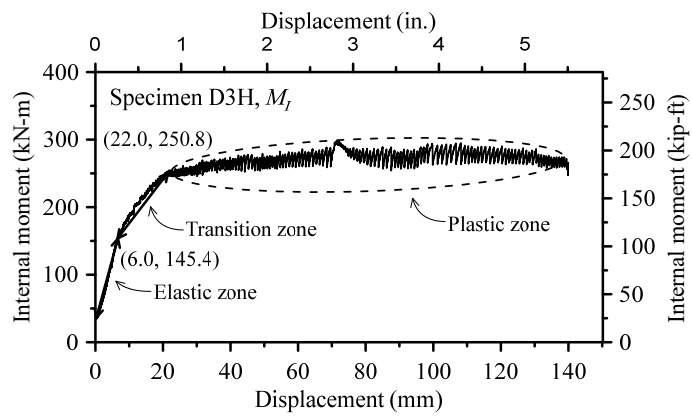
(a) Zone identification (B4H)



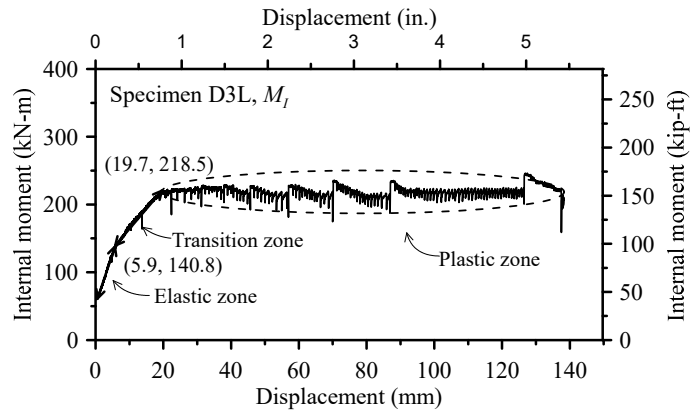
(b) Zone identification (B4L)



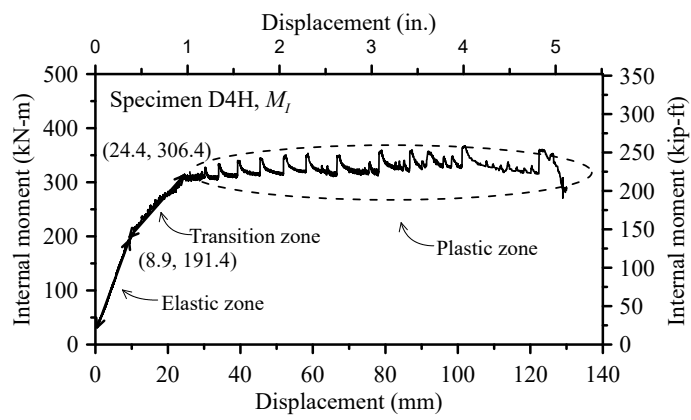
(c) Zone identification (B5L)



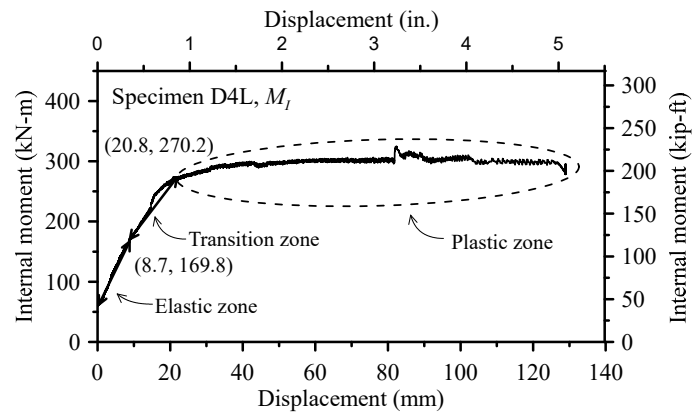
(d) Zone identification (D3H)



(e) Zone identification (D3L)



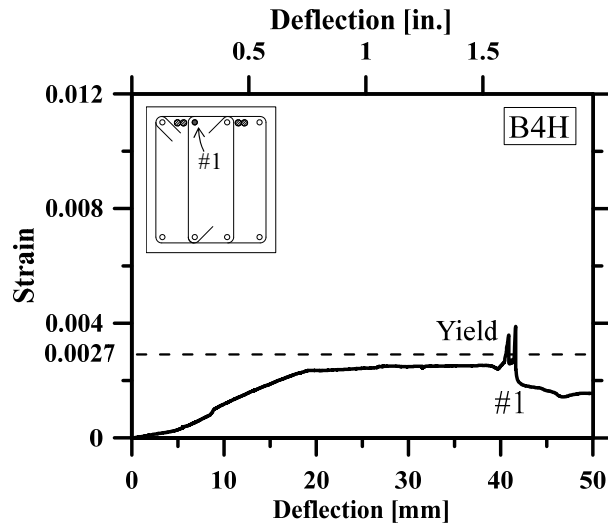
(f) Zone identification (D4H)



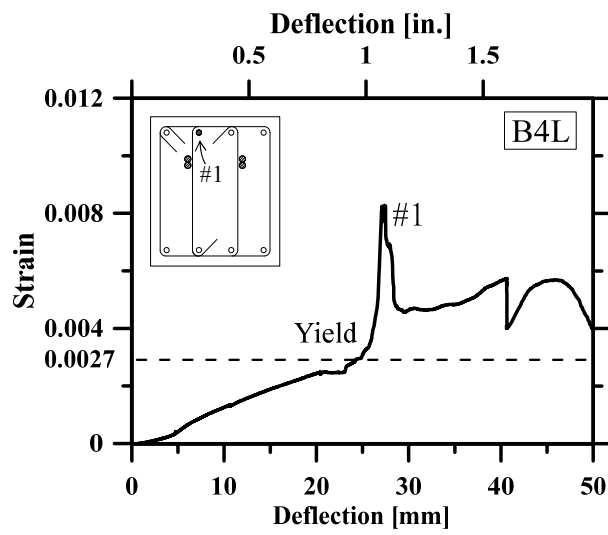
(g) Zone identification (D4L)

**Figure D-1** Behavior zone identification of the specimens

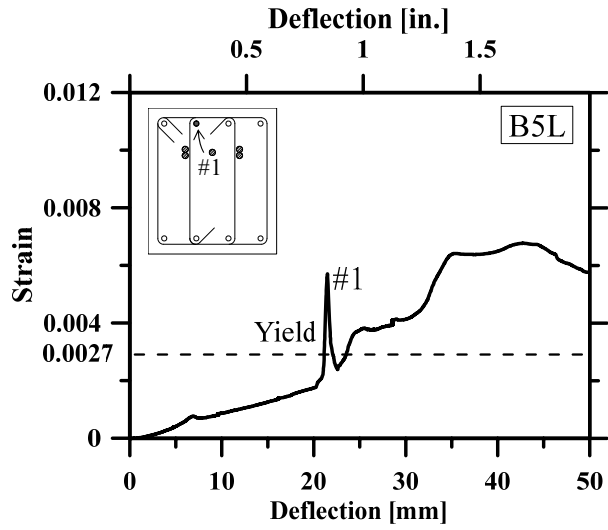
## **Appendix E : Steel strain gauge data**



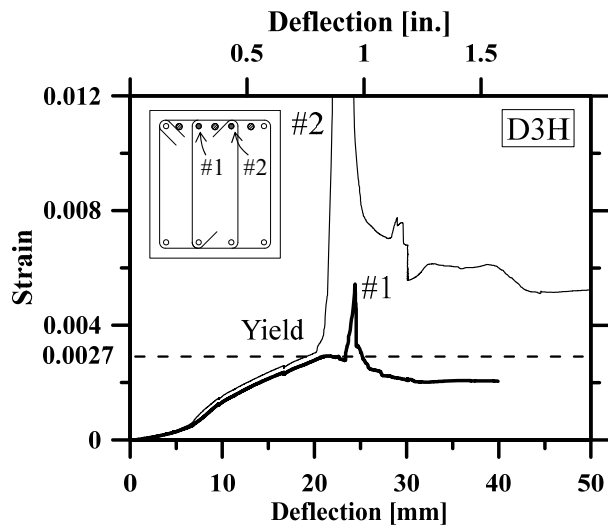
(a) Strain in reinforcing bar in tension at B4H



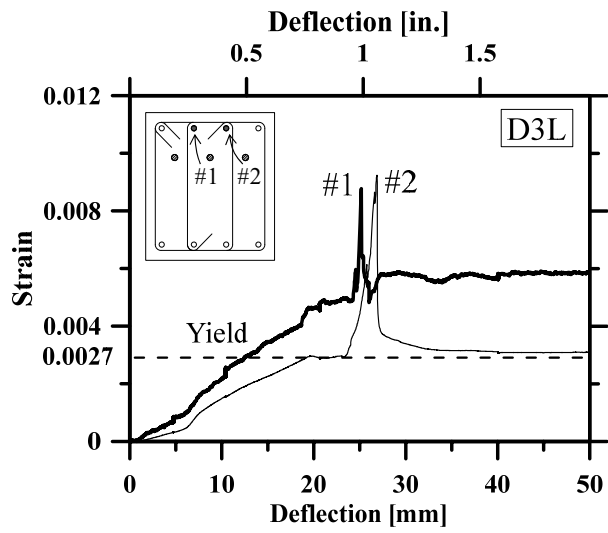
(b) Strain in reinforcing bar in tension at B4L



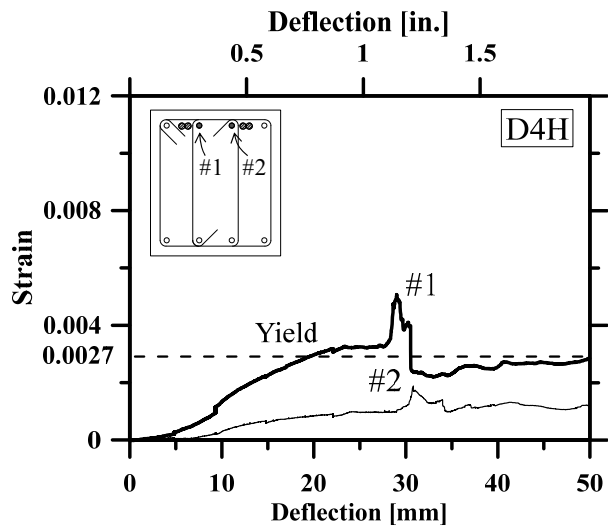
(c) Strain in reinforcing bar in tension at B5L



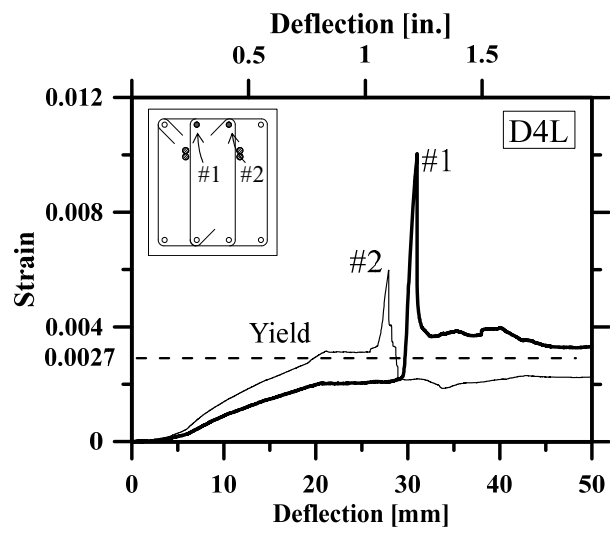
(d) Strain in reinforcing bar in tension at D3H



(e) Strain in reinforcing bar in tension at D3L



(f) Strain in reinforcing bar in tension at D4H



(g) Strain in reinforcing bar in tension at D4L

**Figure E-1** Strain measured at the reinforcing bar in tension at the interior support

## 국 문 초 록

### 2400MPa 비부착 강연선이 적용된 2경간 연속 보의 실험적 연구

최근 국내 기술로 기존 1860MPa급(Grade 270) 강연선 보다 강도가 증가한 2160MPa, 2400MP급 고강도 강연선이 개발되었다. 고강도 강연선을 적용하게 되면 예상되는 여러 가지 이점들에도 불구하고 관련 기준과 적용 사례 및 연구의 미비로 실무에서는 1860MPa급 강연선이 주로 사용되고 있는 실정이다. 이에 따라 해당 연구에서는 총 일곱 개의 2경간 비부착 포스트텐션 보에 대한 실험적 연구를 수행하였고, 변수로는 강연선의 강도, 텐던 프로파일의 높이, 그리고 프리스트레싱력의 양이 적용되었다. 실험 결과, 고강도 강연선이 적용된 네 개의 실험체 모두 일반강도 강연선이 적용된 실험체와 동급의 강도와 연성거동능력을 보이는 것으로 확인되었다. 이는 기존의 설계지침에 따라 일반강도 강연선 대신 고강도 강연선을 비부착 포스트텐션 휨 부재에 적용 가능하다는 것을 의미한다. 보다 자세한 설명은 일반강도 강연선과 고강도 강연선의 물리적 특성, 소성 힌지의 길이와 소성 힌지 파괴 거동에 대한 각 실험체의 비교를 통해 본 논문에 자세하게 기술되어 있다. 2차 모멘트에 대한 측정과 평가 또한 이루어졌는데, 2차 모멘트는 탄성거동구간에서 거의 일정한 크기를 유지하다가 소성 거동이 발생하기 시작하면서부터 급격

하게 증가하는 것으로 나타났다. 공칭강도를 발휘하는 지점에서 평가된 2차 모멘트는 기존의 load balancing method를 통하여 계산한 값보다 매우 크게 나타나는 것으로 관찰되었으며, 이 연구 결과를 고려해 보았을 때 부정정 PT 구조 설계 시 2차 효과의 평가에 대하여 새로운 접근법이 필요하다고 사료된다.

**핵심용어:** 고강도 강연선, 비부착 포스트텐션 보, 2차 모멘트, 프리스트레스.

**학번:** 2016-26786